PRODUCTION AND CHARACTERIZATION OF HIGH PERFORMANCE Al – Fe – V – Si ALLOYS FOR ELEVATED TEMPERATURE APPLICATIONS

A THESIS SUBMITTED TO
THE GRADUATE SCHOOL OF NATURAL AND APPLIED SCIENCES
OF
MIDDLE EAST TECHNICAL UNIVERSITY

BY

SEDA SAYILGAN

IN PARTIAL FULFILLMENT OF THE REQUIREMENTS
FOR
THE DEGREE OF MASTER OF SCIENCE
IN
METALLURGICAL AND MATERIALS ENGINEERING

JUNE 2009

Approval of the thesis:

PRODUCTION AND CHARACTERIZATION OF HIGH PERFORMANCE Al – Fe – V – Si ALLOYS FOR ELEVATED TEMPERATURE APPLICATIONS

submitted by **SEDA SAYILGAN** in partial fulfillment of the requirements for the degree of **Master of Science in Metallurgical and Materials Engineering Department, Middle East Technical University** by,

Prof. Dr. Canan Özgen _____
Dean, Graduate School of **Natural and Applied Sciences**

Prof. Dr. Tayfur Öztürk _____
Head of Department, **Metallurgical and Materials Engineering**

Prof. Dr. Ali Kalkanlı _____
Supervisor, **Metallurgical and Materials Engineering Dept., METU**

Examining Committee Members:

Prof. Dr. Alpay Ankara _____
Metallurgical and Materials Engineering Dept., METU

Prof. Dr. Ali Kalkanlı _____
Metallurgical and Materials Engineering Dept., METU

Prof. Dr. Ekrem Selçuk _____
Metallurgical and Materials Engineering Dept., METU

Prof. Dr. Rıza Gürbüz _____
Metallurgical and Materials Engineering Dept., METU

Assoc. Prof. Dr. Nuri Durlu _____
Mechanical Engineering Dept., TOBB ETU

Date: 25.06.2009

I hereby declare that all information in this document has been obtained and presented accordance with the academic rules and ethical conduct. I also declare that, as required by these rules and conduct, I have fully cited and referenced all material and results that are not original to this work.

Name, Last name : Seda SAYILGAN

Signature :

ABSTRACT

PRODUCTION AND CHARACTERIZATION OF HIGH PERFORMANCE
Al – Fe – V – Si ALLOYS FOR ELEVATED TEMPERATURE APPLICATIONS

Sayılgan, Seda

M.S., Department of Metallurgical and Materials Engineering

Supervisor: Prof. Dr. Ali Kalkanlı

June 2009, 138 pages

In the present study, the powder metallurgy was evaluated as a technique to produce high performance Al – 8Fe – 1.7V – 7.9Si (wt%) alloys for elevated temperature applications and the role of powder particle size range and extrusion ratio in the microstructural and mechanical properties of the extruded alloys was investigated. For this purpose, an air atomization method was employed to produce powders of the high temperature alloy and after that the produced powders were sieved and cold compacted. The compacted billets were subsequently hot extruded at 450 – 480 °C. Five selected ranges of powders which were different in particle size (−2000+212 μm, −212+150 μm, −150+106 μm, −106+90 μm, and −90 μm) and three different extrusion ratios (144:1, 81:1, and 26:1) were used in this study.

In the first part of the thesis, microstructure and thermal stability of as – air atomized powders were described. α – Al matrix and α – $Al_{13}(Fe, V)_3Si$ phases were characterized in all rapidly solidified powders by XRD. The fraction of the intermetallic phases was reduced as the powder particle size increased. DTA

analysis revealed an exothermic reaction at 581 °C in all alloy powders of different size fractions.

In the second part of the study, the effect of powder particle size and extrusion ratio on microstructural and mechanical properties (at different temperatures) of the extruded alloys was investigated. The results showed that decrease in powder particle size and increase in extrusion ratio refined the microstructure and improved the mechanical properties. It was revealed that the effect of powder size was more evident than that of extrusion ratio. Remarkable increases in mechanical properties (e.g. 60.7% increase in ultimate tensile strength at 250 °C) were observed as a result of rapid solidification process (atomization) and hot extrusion.

Keywords: Al – Fe – V – Si alloy, rapid solidification, powder metallurgy, air atomization, mechanical properties.

ÖZ

YÜKSEK SICAKLIK UYGULAMALARI İÇİN YÜKSEK BAŞARIMLI
Al – Fe – V – Si ALAŞIMLARININ ÜRETİMİ VE KARAKTERİZASYONU

Sayılgan, Seda
Yüksek Lisans, Metalurji ve Malzeme Mühendisliği Bölümü
Tez Yöneticisi: Prof. Dr. Ali Kalkanlı

Haziran 2009, 138 sayfa

Bu çalışmada, toz metalurjisi yüksek sıcaklık uygulamaları için yüksek başarımlı Al – 8Fe – 1.7V – 7.9Si (% ağırlıkça) alaşımlarının üretim tekniği olarak değerlendirilmiş ve ekstrüzyon sonucu üretilmiş alaşımların içyapısal ve mekanik özelliklerine toz tane boyutu aralığının ve ekstrüzyon (dar çıkım) oranının işlevi incelenmiştir. Bu amaçla, yüksek sıcaklık alaşım tozlarını üretmek için hava atomizasyonu yöntemi kullanılmıştır ve bundan sonra tozlar elenmiş ve soğuk sıkıştırılmıştır. Sıkıştırılan tozlara sonra 450 – 480 °C' de sıcak ekstrüzyon yöntemi uygulanmıştır. Farklı tane boyut aralığındaki beş çeşit toz (−2000+212 μm, −212+150 μm, −150+106 μm, −106+90 μm ve −90 μm) ve üç farklı ekstrüzyon oranı (144:1, 81:1 ve 26:1) bu çalışmada kullanılmıştır.

Tezin birinci bölümünde, hava atomizasyonu ile üretilen tozların içyapıları ve ısıl kararlılıkları anlatılmıştır. Tüm hızlıca katılaşmış tozlarda α – Al matris ve α – $Al_{13}(Fe, V)_3Si$ fazları XRD ile karakterize edilmiştir. Toz tane boyutu arttıkça, intermetalik fazların oranı azalmıştır. DTA analizi, farklı boyut aralıklarındaki tüm alaşım tozlarında 581 °C' de bir ekzotermik tepkime olduğunu ortaya çıkarmıştır.

Tezin ikinci bölümünde, ekstrüzyon sonucu üretilmiş alaşımların içyapısal ve mekanik özelliklerine (farklı sıcaklıklarda) toz tane boyutunun ve ekstrüzyon oranının etkileri incelenmiştir. Sonuçlar, toz tane boyutundaki azalma ve ekstrüzyon oranındaki artmanın içyapıyı incelttiğini ve mekanik özellikleri geliştirdiğini göstermiştir. Toz tane boyutunun etkisinin, ekstrüzyon oranınınkinden daha belirgin olduğu ortaya çıkarılmıştır. Hızlı katılaşma yöntemi olan atomizasyon ve sıcak ekstrüzyonun sonucu olarak mekanik özelliklerde dikkat çekici artışlar gözlemlenmiştir (ör. 250 °C' deki çekme dayanımında % 60.7 artış).

Anahtar Kelimeler: Al – Fe – V – Si alaşımı, hızlı katılaşma, toz metalurjisi, hava atomizasyonu, mekanik özellikler.

To my family;
Nazım, Kiraz and Selda Sayılgan

ACKNOWLEDGEMENTS

I would like to express my deepest gratitude to my supervisor Prof. Dr. Ali Kalkanlı for his guidance, continuous support and encouragement throughout this study.

I am also thankful to Gökhan Türkyılmaz and Özgür Keleş for their valuable supports, motivation and invaluable friendship in all part of the study.

My special thanks go to the technical staff of the Department of Metallurgical and Materials Engineering, METU, especially Salih Türe for their contributions to this study.

I would also like to thank to Arda Çetin, Turgut Kırma, Yankı Başaran, Betül Pelin Maradit, Çağla Özgit, Gülhan Çakmak, and Güher Kotan for their helps and supports.

Thanks are also extended to Mehmet Konyalı from OSKO Aluminum for kindly providing the facility of extrusion.

I would like to express my sincere thanks to Mehtap Soytürk, Ayşe Deniz Çulha, Derya Saygı, and Senem Aksöz for always being supportive in my life.

Finally, I want to express my great thanks to my family for supporting, encouraging, and loving me all through my life. It would not have been possible to complete this study without their love.

This study was supported by The Scientific and Technological Research Council of Turkey (TUBITAK) Grant No: 105M058.

TABLE OF CONTENTS

LIST OF TABLES

LIST OF FIGURES

CHAPTER 1

INTRODUCTION

There are numerous technical advantages of aluminum alloys. These advantages have enabled them to be one of the dominant structural material families of the 21st century. Aluminum is comparable with competitive metallic alloy systems with respect to the low density (2.71 g/cm^3), good inherent corrosion resistance (due to very quick formation of the continuous, protective oxide film in air) and good workability that enables aluminum and its alloys to be economically rolled, extruded, or forged into useful shapes. However, aluminum alloys have limitations compared with competitive materials. For instance, Young's modulus of ferrous alloys (about 210 GPa, or 30 × 10^6 psi) or titanium alloys (about 112 GPa, or 16 × 10^6 psi) are higher than that of aluminum (about 70 GPa, or 10 × 10^6 psi) [1]. In addition, the most important limitation is insufficient high temperature mechanical properties that originate from lower melting point of aluminum (660 °C) than major competitive alloy systems such as iron – based, nickel – based, and titanium – based alloys [2]. Therefore, in spite of aluminum alloys' low density, the mechanical properties of aluminum alloys at elevated temperatures are not competitive with these alloy systems and the use of aluminum alloys for certain structural components in aircrafts and aerospace structures is limited.

The search for aluminum alloys which have high temperature mechanical properties has been carried out in recent decades. The addition of alloying elements can enhance the mechanical properties of aluminum alloys and enable the high temperature usage of them. On the other hand, there are not many precipitation – hardenable aluminum alloy systems that are produced by conventional ingot metallurgy because the number of alloying elements that have extensive solid

solubility in aluminum is relatively low [1]. This hinders the design of better alloys. The demand for high temperature strength, high performance and cost effective materials revealed that the necessity of novel processing techniques for the development of new aluminum alloys. With this respect, rapid solidification (RS) is an effective technology in combining microstructure and mechanical properties. The introduction of high thermal gradient during RS accounts for solid solubility extension, grain size reduction and decrease in both the number and size of segregated phases, and new metastable alloy phases [3].

There should be constituents that do not undergo phase transformation and resist rapid coarsening in aluminum alloys for applications at elevated temperatures [4]. A new class of aluminum alloys strengthened by dispersoids of aluminum – rich intermetallic compounds is produced by RS. The importance of these alloys arises from various metastable intermetallic compounds that provide unique structure, thermal stability and desirable properties in an aluminum matrix [5]. Higher temperature capability of these aluminum alloys is due to the presence of thermally stable dispersoids in the microstructure. There are three basic requirements for forming thermally stable dispersoids in the microstructure. The first one is that the alloying element should have low solid solubility and low diffusivity to have a minimal coarsening during high temperature exposure. Another requirement is that the alloying elements should have high liquid solubility to have a large volume fraction of dispersoids in the microstructure. The last one is the fact that alloys should be solidified very rapidly to form the required fine dispersoids [6].

Dispersion strengthened aluminum alloys which are based on Al – transition metal (TM) type systems are used for elevated temperature structural applications in aircrafts and aerospace [3, 7, 8]. These Al – TM alloys contain transition metals such as Fe, Ni, V, Cr, Zr, Mo and Ti with possible additions of Si and Ce [9]. The thermal stability of Al – TM binary systems is enhanced by addition of ternary and quaternary elements. Al – Fe – Ce, Al – Fe – V – Si, Al – Mn, Al – Cr, Al – Zr, and Al – V are some examples of these alloy systems [5]. Among these alloys, Al – Fe –

V – Si alloy has good combination of excellent properties such as strength, ductility, fracture toughness, fatigue crack growth resistance, corrosion resistance and creep rupture at room and high temperatures (up to 350 °C) [6, 10].

To produce a bulk material having the same microstructure with initial rapid solidified structures like ribbons, powders etc., they could be consolidated [11]. Traditional consolidation methods (hot isostatic compaction, uniaxial hot pressing, sintering etc.) provide medium level strength but higher strength levels can be obtained with the use of extrusion [12].

The main objective of this study was to produce Al – Fe – V – Si alloys via powder metallurgy techniques, which are air atomization of Al – 8Fe – 1.7V – 7.9Si, cold – compaction and hot – extrusion, and characterize them with several methods. Moreover, an optimization study on powder particle size and characteristics of air atomized alloy which affects microstructure and mechanical properties of as – extruded Al – Fe – V – Si alloy was conducted.

In the first part of the thesis, Al – 8Fe – 1.7V – 7.9Si alloy was produced by air atomization. As – atomized powders were characterized by means of particle size, particle shape, interparticle friction, thermal and microstructural analysis using screening, scanning electron microscopy (SEM), Hall flowmeter, differential thermal analysis (DTA), and X – Ray diffraction (XRD), respectively. In the second part of the study, resulting powders were cold – compacted and extruded at 450 °C. As – extruded alloys were examined in order to determine microstructural and mechanical properties at elevated temperatures. Also, the effect of powder particle size and characteristics on microstructure and mechanical properties of the alloys produced from different particle size range was investigated.

CHAPTER 2

LITERATURE SURVEY

2.1 Rapid Solidification

Rapid solidification (RS) has attracted a great deal of attention because it provides wide range of opportunities for material science and engineering [13]. Important constitutional variations in materials including solid solubility extensions, solute trapping, and the formation of nonequilibrium crystalline, quasicrystalline, and fully amorphous phases is affected by RS. Furthermore, it can affect significant microstructural properties, which are the refinement of the material microstructure, the formation of microcrystalline phases, and the formation of nonequilibrium concentrations of lattice defects. With the help of RS, these constitutional and microstructural changes in materials are introduced in a controlled manner [14].

The rapid extraction of thermal energy (superheat and latent heat) during transition from the liquid state at high temperatures to solid material at ambient temperature is called rapid solidification [3]. RS is a far – from – equilibrium process that results in a significant undercooling of the molten metals or alloys leading to significant microstructural and constitutional effects in materials [2]. Undercooling of 100 °C or more before solidification is obtained by the rapid extraction of heat. These are the advantages of RS which are the consequences of large deviations from equilibrium:

- Solid solubility limit extension
- Grain size reduction

- Reduction in both amount and size of segregated phases
- Synthesis of novel phases [14].

The solubility for several elements to aluminum based on the equilibrium phase diagram is shown in Table 2.1. For comparison, Table 2.1 also gives the extending solubility limit for aluminum through use of RS.

Table 2.1 Extended solubility in aluminum via RS [15].

Element	Equilibrium, at%	RS Maximum, at%
Cr	0.4	6
Cu	2.5	18
Fe	0.03	6
Mg	18.9	40
Mn	0.7	9
Ni	0.02	8
Si	1.6	16

One of the following approaches stated below is necessary to achieve rapid solidification:

- High undercooling before solidification
- High velocity of advance during continuous solidification
- High cooling rate during solidification [3].

Supercooling of liquid metal to a temperature at which the latent heat released during solidification (before transferred to the surroundings) can be dissipated through total volume of the solidifying volume is required in the first approach. An illustration of the concept of undercooling is represented in Figure 2.1. In this figure, T_1, T_2, and T_3 are undercooling temperatures of alloy C_0 and T_R and T_S are

the recalescence and solidus temperatures, respectively. Alloy with composition C_0 is undercooled into the singe phase region, α. Because of increase in temperature due to recalescence, which is the release of latent heat of solidification, it returns to the two phase region, α + L. This condition is illustrated in Figure 2.1 (a). Critical undercooling (T_R=T_S) is given in Figure 2.1 (b). Recalescence makes return to the temperature definitely T_S. Figure 2.1 (c) demonstrates that recalescence brings the temperature into single phase region ($T_R < T_S$). This is called hypercooling. Materials having high specific heat (C) and low latent heat of solidification (L) have higher temperature of solidifying volume during recalescence when there is no heat transfer to the surroundings. With this respect, hypercooling occurs when the initial undercooling (ΔT) below the equilibrium liquidus exceeds the temperature rise which is directly proportional to C/L [14].

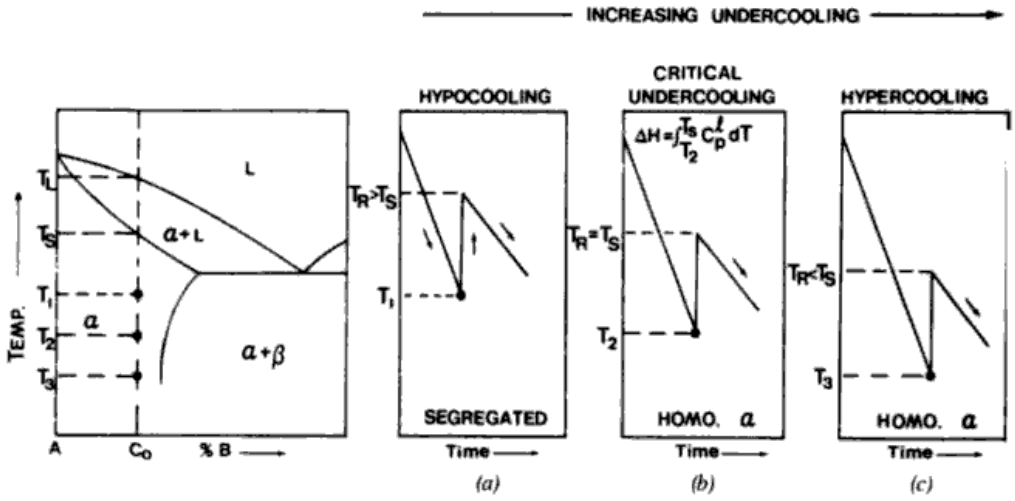

Figure 2.1 An illustration of concept of critical undercooling and hypercooling [3].

The second approach to achieve rapid solidification is high velocity of advance during continuous solidification. This is accomplished by pulling a sufficiently thin specimen with high velocity enough to force the solidification front to advance at drawing velocity [14].

Introducing a high cooling rate during solidification is the third and most commonly used approach for rapid solidification. This is attributed to wide range of available experimental techniques. This approach is applicable to numerous alloy compositions. In practice, the striking effect of imposing a high cooling rate during solidification is based on making one dimension of solidifying volume very small and extracting heat very rapidly. The nucleation and growth of solid phases from melt under rapid heat extraction forms unusual nonequilibrium structures [3].

2.1.1 Microstructures of Rapidly Solidified Aluminum Alloys

A range of rapid solidification processes have been developed to produce the metastable microstructure in materials. The formation of unique microstructures during RS is the result of extreme rates of heat removal and thermodynamically unstable melts. Large deviation from equilibrium, as evidenced by the extension in solid solubility limits, the reduction or elimination of the detrimental effects of segregation, the development of new nonequilibrium crystalline, quasicrystalline, or noncrystalline (amorphous) phases, and the sharp reduction of grain size to the micrometer or nanometer scale, is permitted by the rapid extraction of thermal energy associated with RSP [16]. There are three main effects of RS on microstructures of aluminum alloys:

- Constitutional changes (as a result of high levels of undercooling during RS)
- Size refinement (due to high velocity of the interface during solidification)
- Formation of metastable phases (including amorphous and quasicrystalline phases) [14].

RS forms nonequilibrium phases that are glasses, quasicrystalline phases, new crystalline phases and equilibrium phases with extended composition ranges. Two general types of noncrystalline phases exist in aluminum base alloys. These are amorphous and quasicrystalline phases. Both of them can preserve their properties at moderate temperatures. The production of amorphous phases is very difficult in aluminum base alloys. These alloys have very low crystallization temperatures

relative to their liquidus temperatures so they must be solidified very rapidly for formation of amorphous phases. In addition, because of the brittleness of these alloys in amorphous state, these cannot be used for any structural applications [14]. The fact that the entire or residual melt is undercooled below the glass – forming temperature before the advance of crystal formation can complete the solidification process is required for glass formation. It is highly dependent on alloy composition, purity and cooling rate during solidification in order to inhibit the rapid advance of crystal formation. If nonequilibrium crystalline phases' nucleation and growth kinetics results in a higher rate of formation than the competing equilibrium phases, formation of nonequilibrium crystalline phases by rapid solidification can occur [17].

While formation of amorphous structures is difficult in aluminum base alloys, quasicrystals are found in these alloys easily. Quasicrystals are highly ordered structures, even though they lack translational periodicity. Quasicrystals may be regarded as a type of intermetallic compound in which quasi – periodic translational order is required. Although development of either (chemical) order or twinning is dependent on long range periodicity, the lack of long range periodicity does not inhibit these properties [18]. Quasicrystals exhibit true five – fold (icosahedral) or ten – fold (decagonal) symmetry and their structures can extend over sizeable distances because of the lack of perfect periodicity. According to studies, there are at least two types of quasicrystalline phases (icosahedral and decagonal). They are very sensitive to alloy composition and solidification conditions [3].

There are three types of formation of metastable crystalline phases in aluminum alloys, which are

- Phases formed during quenching that are present under some equilibrium conditions but not thermodynamically stable at temperatures and alloy compositions in which they are observed (Type 1),

- Phases that are not formed during quenching from melt but appear during thermal treatment (Type 2),
- Phases which are present in rapid solidified samples but do not exist under equilibrium conditions at any compositions within the alloy system (Type 3) [3].

A summary of metastable phases detected in binary aluminum alloys are given in Table 2.2.

Table 2.2 Nonequilibrium phases detected in aluminum binary alloys under RS [3].

Alloying Element	Concentration Range (at. %)	Nonequilibrium Phase Detected	Type	Corresponding Equilibrium Phases
Cr	1.6 – 3	Al_4Cr	1	α – Al + Al_7Cr
Cu	45	Al_3Cu_2 (trigonal)	3	O + η_2
	17.3	Noncrystalline	3	α – Al + O
Fe	2 – 4	γ, γ', γ'', o^{α}	2	Al_3Fe + α – Al
	4	Al_6Fe (orthorombic)	2	–
	–	Al_6Fe	3	–
Mg	25	Le_2 superlattice	2	α – Al + β – Al_3Mg_2
	40	(α – Mn) like structure	3	α – Al + β – Ml_3Mg_2
Mn	≤ 6	Al_4Mn	1	α – Al + Al_6Mn
Ni	7.3 – 10.1	η (orthorombic)	3	α – Al + β – Al_3Ni

2.1.2 Rapid Solidification Techniques

A moving or stationary substrate or jets of gas or liquid is required for rapid solidification processing [3]. There are several ways to produce rapidly solidified materials. Figure 2.2 shows the production methods of rapid solidification.

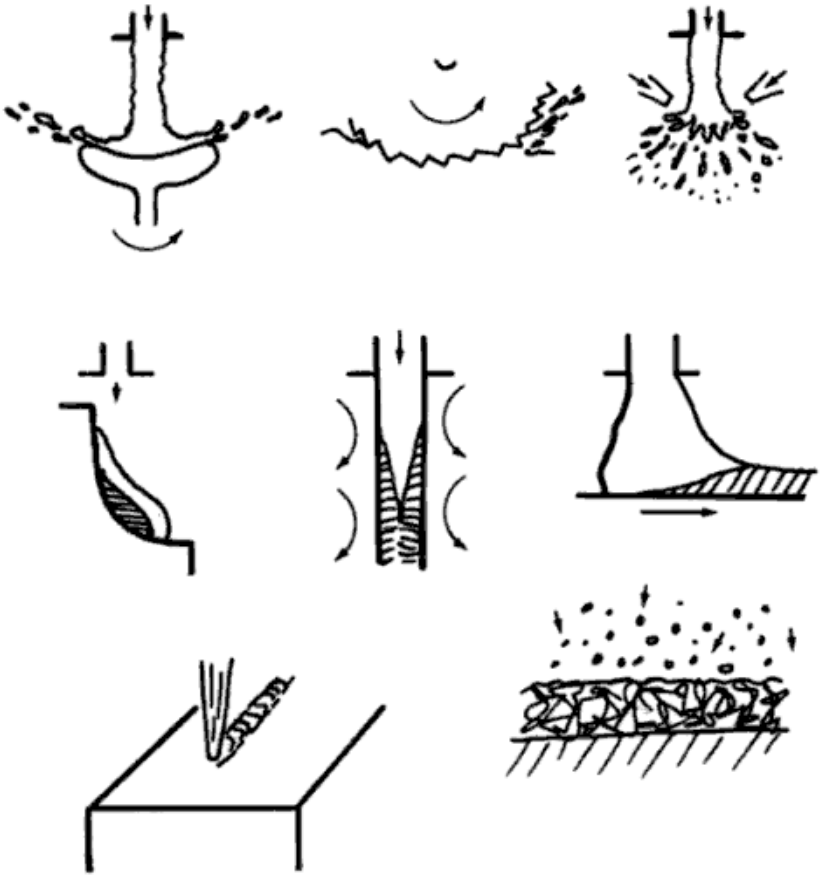

Figure 2.2 A classification of rapid solidification process [14].

Rapid solidification processes are classified into four different types according to the presence of common physical features. RS processes which produce only individual samples of RS materials are named as single splat techniques. In addition, processes that involve fine particulate material as members of the same groups are called atomization processes. If the product is in the form of a long continuous ribbon or wire, these processes can be grouped as continuous processes. Finally, processes which use the thermal conductivity of the bulk medium itself to produce RS are classified as self – quenching. Schematic representations of these processes are given in Figures 2.3 through 2.6.

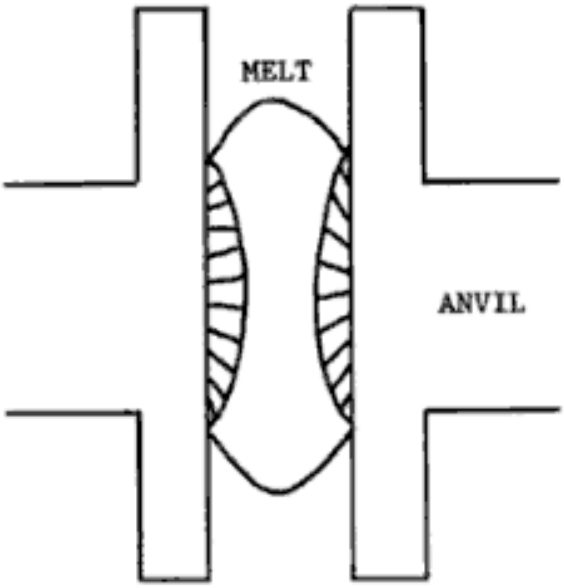

Figure 2.3 Schematic representation of the singe splat process [14].

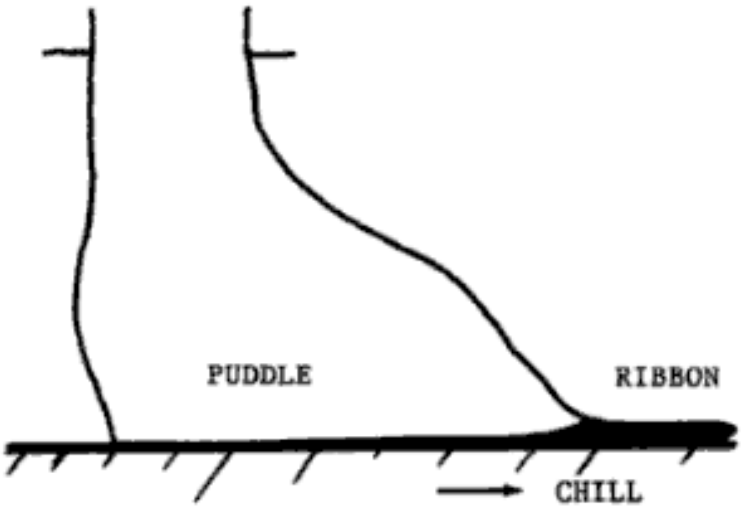

Figure 2.4 Schematic representation of the continuous process [14].

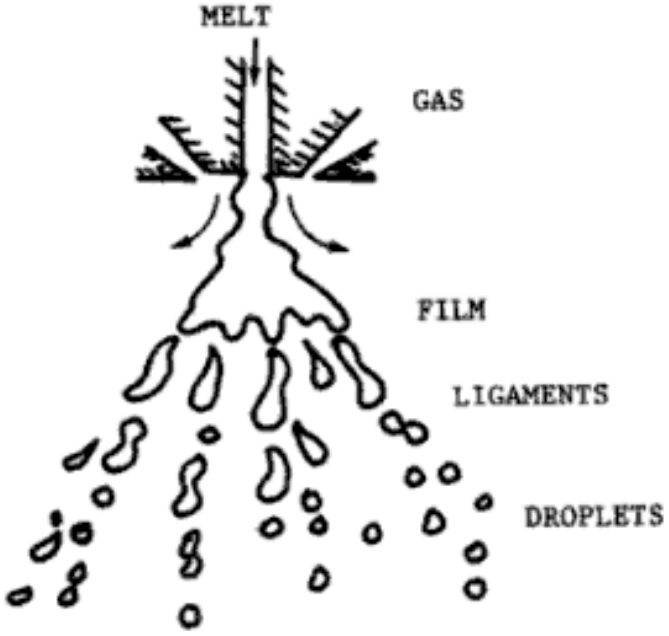

Figure 2.5 Schematic representation of the atomization process [14].

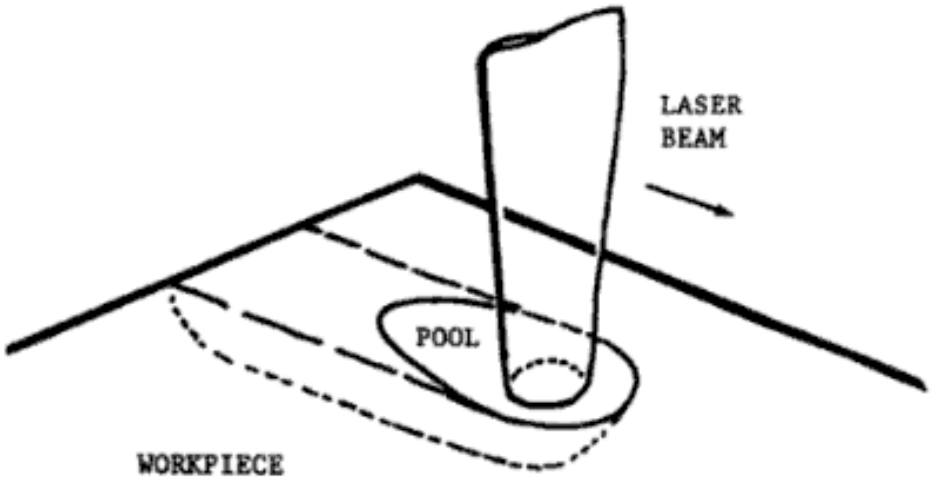

Figure 2.6 Schematic representation of the self – quenched process [14].

Among these processes, atomization, spray deposition, and ribbon or foil casting are generally used for production of rapid solidified aluminum alloys [3].

2.1.2.1 Spray Deposition

In spray deposition, finely divided molten metal droplets, which are produced by disintegration of a stream of molten metal using high−energy inert gases, impinge on a substrate before they completely solidify. This ensures some properties of RS with a near – net shape capability [19]. The production of alloy compositions which are difficult to produce conventionally is promoted by spray deposition. One particular spray deposition set – up is shown in Figure 2.7. There are two main processes that involve the impact of melt droplets on a solid surface before complete solidification. The first one is the spray forming in which near – net shape billets, tubes, and more complex shapes are manufactured without the ingot stage. The second is the spray coating. A metallic substrate is coated with a thin coating of either metallic or ceramic material [20].

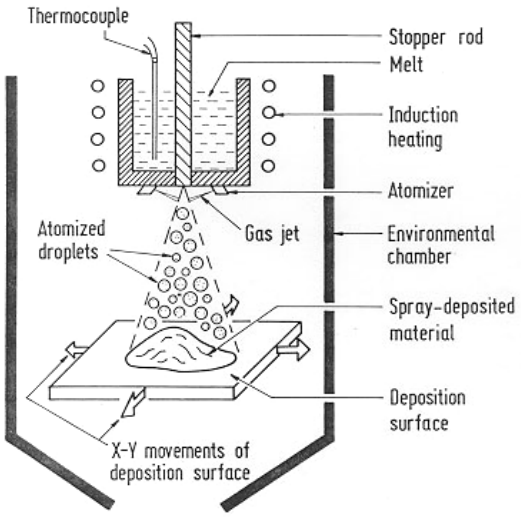

Figure 2.7 Schematic drawing of experimental arrangement for spray deposition [14].

2.1.2.2 Ribbon or Foil Casting

More rapid cooling and more refined structures than other RS techniques are obtained ribbon or foil casting processes [14]. Melt spinning, planar flow casting and melt overflow are ribbon or foil casting processes.

In melt spinning, a molten metal stream is squirted onto a rapidly spinning copper disk (20,000 RPM). The melt solidifies on the disk and forms rapidly solidified product that is often in ribbon form. These ribbons are dragged out by centrifugal forces [15]. Cooling rate in melt spinning is as high as 10^6 K/sec [14]. Melt spinning is illustrated schematically in Figure 2.8.

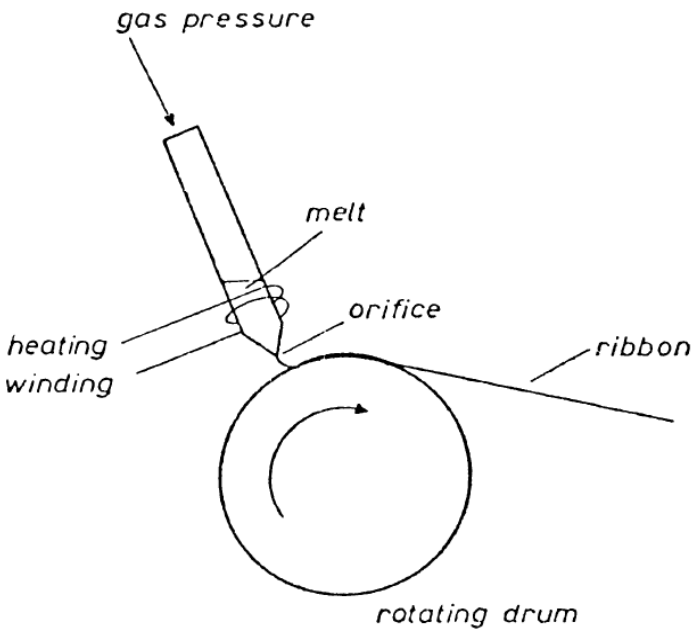

Figure 2.8 A sketch of melt spinning [17].

The melt is forced through a slotted orifice and onto a rapidly moving chill surface in planar flow casting (PFC). In PFC, a nozzle is positioned near a moving substrate in order to control the thickness of the ribbon, as shown in Figure 2.9 [3].

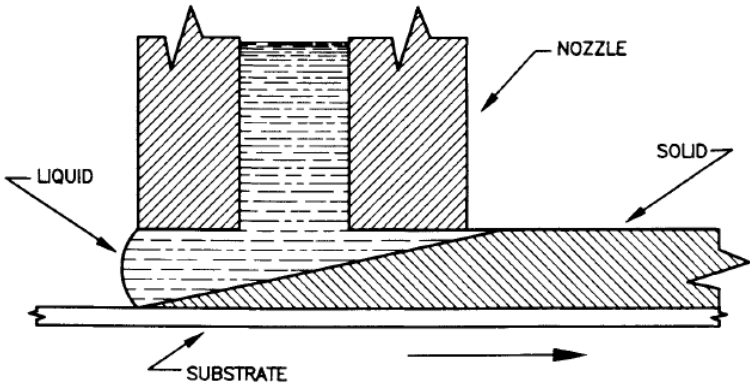

Figure 2.9 Schematic representation of PFC as practiced by Allied – Signal Inc. [21].

In melt overflow process, a film of molten metal is dragged from the lip of a melt supply onto a rapidly rotating chilled wheel [14]. Figure 2.10 shows the melt overflow process.

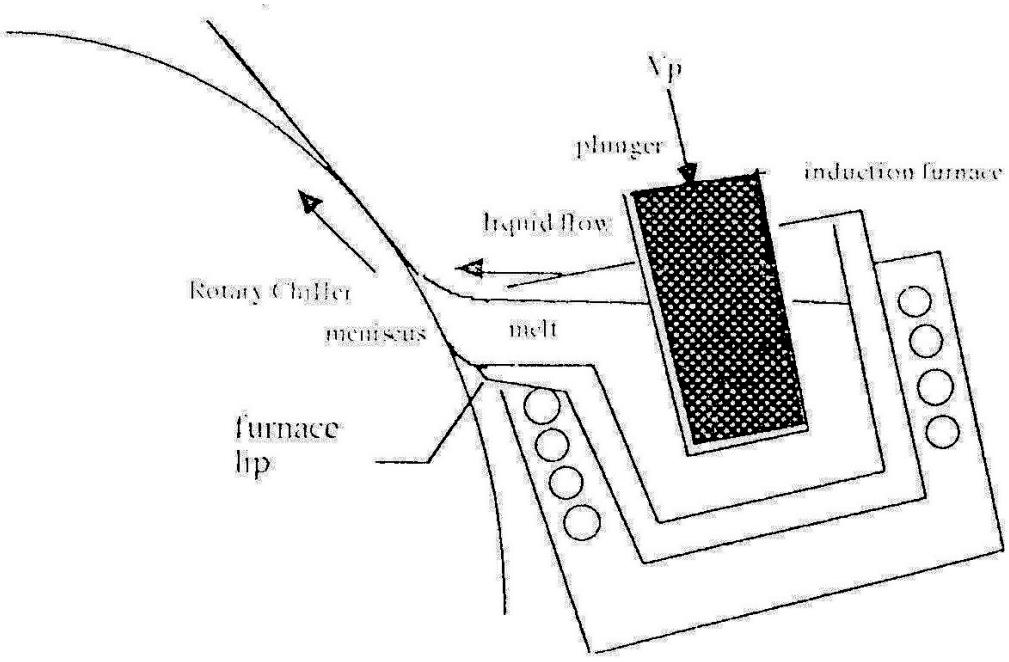

Figure 2.10 An illustration of melt overflow process [22].

2.1.2.3 Atomization

The breakup of a liquid into fine droplets is called atomization. Therefore, any material in molten state can be atomized. Breakup of the liquid into discrete particles is obtained with the use of impingement of liquid or gas, centrifugal force, and vacuum [23]. The transfer of kinetic energy from the atomizing fluid (gas or liquid) to molten metal causes atomization. Rayleigh instabilities that grow on the surface of torn molten ligaments are the origin of droplets [3]. Figure 2.11 exhibits the model for the disintegration of a liquid sheet by a high – velocity gas jet.

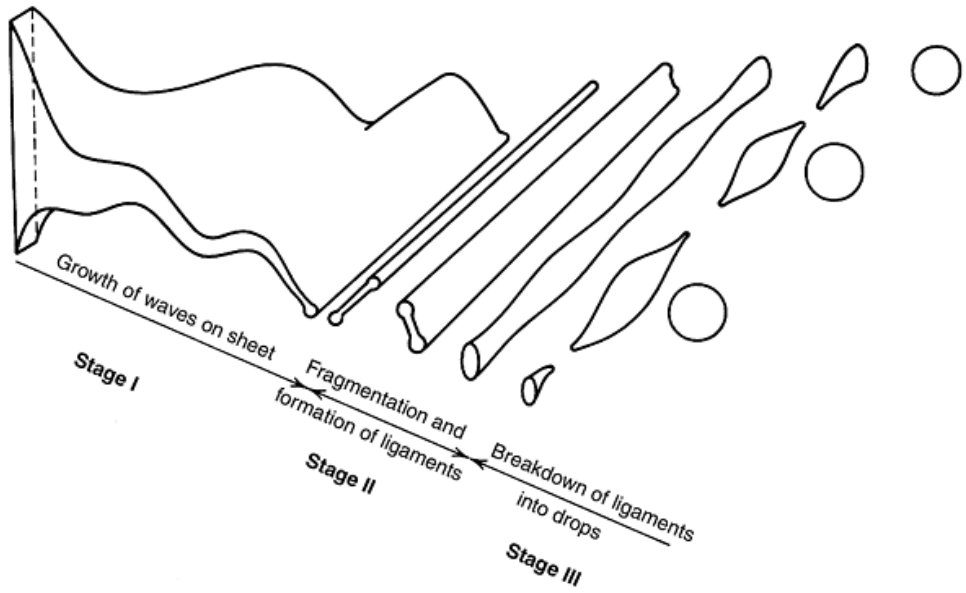

Figure 2.11 Schematic representation of the sheet disintegration and drop formation processes [3].

Dombrowski and Johns proposed that the basic conceptual mechanism of droplet formation in atomization is a three – step process. The initiation of sinuous waves, or other disturbances that rapidly increase in amplitude in stage I, is followed by fragmentation, which forms ligaments in stage II. Breakdown of ligaments into droplets occurs in stage III. Thus, there are three stages involved in the atomization

process: formation of wave with a particular wavelength and wave number, removal of the ligament, and spheroidization of the ligament [19].

Particle formation stages during atomization are seen in Figure 2.12. Lavernia et al. [3] summarize the phenomena associated with the method considering that the size distribution of atomized droplets depend on three major properties. These are

- The properties of the material such as liquidus temperature, density, thermal conductivity, surface tension, heat capacity and heat of fusion,
- The properties of the gas like density, heat capacity, viscosity and thermal conductivity,
- The processing parameters such as atomization gas pressure, superheat temperature, and metal/gas flow ratio.

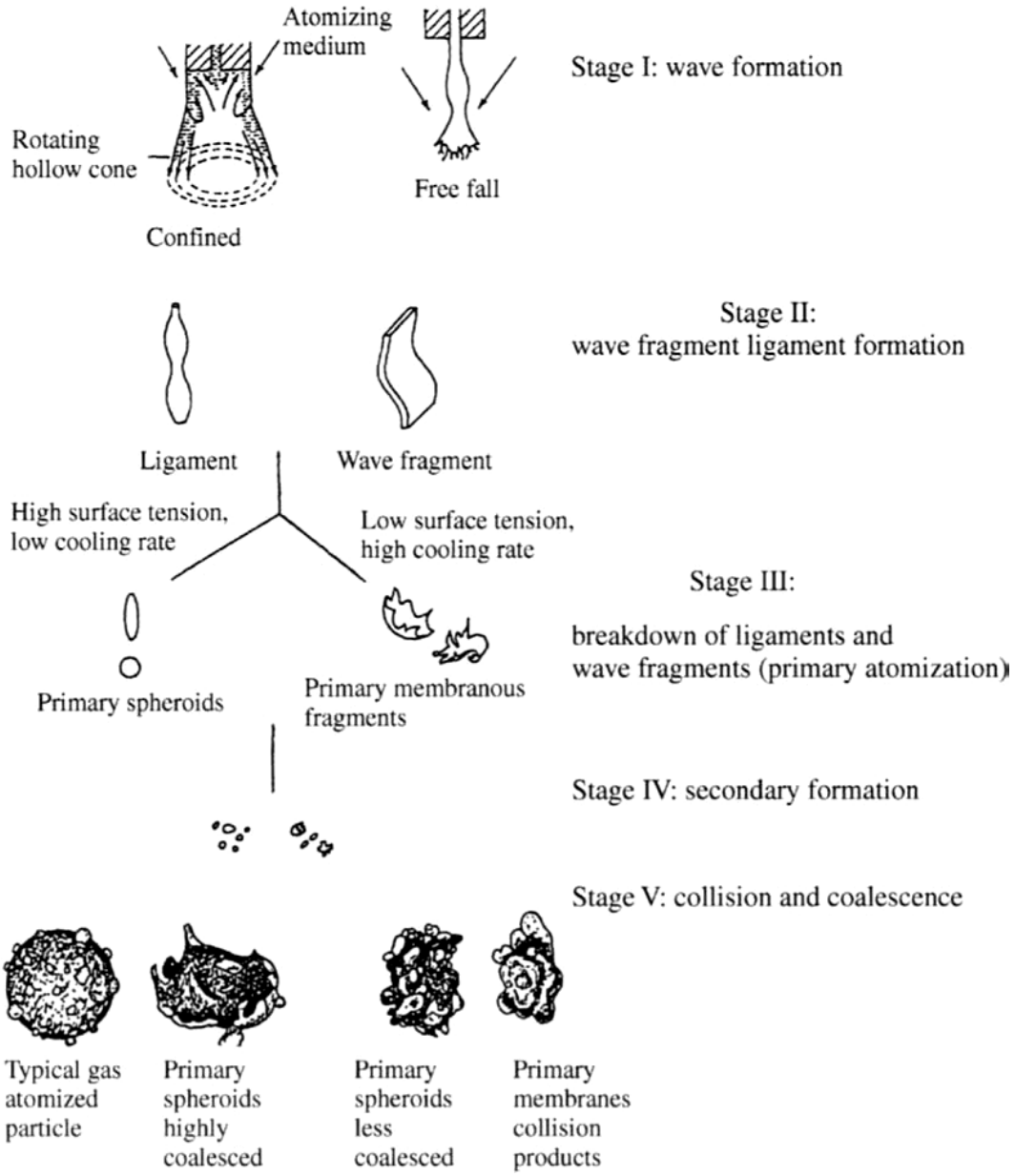

Figure 2.12 Particle formation stages during atomization [3].

One of the most important applications of the atomization method is powder fabrication. Powder is convenient for subsequent consolidation into near final shapes.

2.2 Powder Metallurgy

The powder metallurgy (P/M) process is a near – net or net – shape manufacturing process. P/M combines the features of shape – making technology for powder compaction with the development of final material and design properties (physical and mechanical) during subsequent densification or consolidation processes (e.g., sintering) [19]. P/M enables to produce high quality, complex parts to close tolerances in an economical manner. A metal powder with specific characteristics of size, shape, and packing can be converted into a strong, precise, high performance shape with the use of P/M. Moreover, P/M process is capable of producing a wide range of new materials, microstructures, and properties. That results in various unique applications [15].

Aluminum P/M parts are used in an increasing number of applications. Automotive components, aerospace components, power tools, appliances, and structural parts use the variety of aluminum P/M parts. The flexibility in material selection and design are provided by aluminum P/M alloys due to their mechanical and physical properties. The combination of properties that are light weight, corrosion resistance, high strength, good ductility, nonmagnetic properties, conductivity, machinability, and variety of finishes makes aluminum attractive for P/M parts [19].

2.2.1 Powder Production Techniques

Powder production begins with consideration of size, shape, composition, and structure. These powder properties affect the subsequent compaction, sintering, and densification stages [24]. Powders of almost all materials can be produced. However, suitable methods for powder production depend on required production rates, powder properties, the physical and chemical properties of the material and targeted applications [15, 19]. Precise control of the chemical composition and the physical characteristics of powders can be allowed by various powder production processes.

Significant methods of powder production can be classified into four main groups: mechanical processes, chemical processes, electrolytic processes, and atomization [15, 25, 26]. Atomization and chemical processes are the most widely used but mechanical and electrolytic processes are also used for production of specialty materials in small quantities. Moreover, chemical and electrolytic methods are useful for producing high purity powders whereas mechanical processes are the most widely used methods of powder production for hard metals and oxides.

2.2.1.1 Mechanical Processes

The size reduction of metal powders by mechanical processes is performed in the solid state. The use of mechanical method in P/M is limited because the disintegration of metallic materials, which mostly exhibit high levels of plasticity, is difficult. Nonetheless, materials like intermetallic compounds and ferroalloys powders can be produced into powders by this method. The size reduction in solid state depends on fracture mechanics: the nucleation of cracks, crack propagation and fracture [25].

2.2.1.2 Chemical Processes

Almost all metals are produced into powders by this technique. Powder properties can be controlled easily. The most of processing variables and production parameters permit close control of particle size and shape [19]. The reduction of metal compounds such as oxides, carbonates, nitrates, or halogenides with gases or solids is required by chemical processes [25]. This method includes reduction of oxides, precipitation from solution or from a gas, thermal decomposition, chemical embrittlement, hydride decomposition, and thermit reactions [19, 26].

2.2.1.3 Electrolytic Processes

A reduction process in which the metal ions are neutralized by cathodic current is defined as powder production by electrolysis [25]. High product purity is the main

advantage of electrolytic method. In this method, only elemental powders are produced because contaminants prevent the formation and deposition of powders at the cathode [15].

2.2.1.4 Atomization

The dominant method for producing metal and prealloyed powders from aluminum, brass, iron, low alloy steels, stainless steels, tool steels, super alloys, titanium alloys, and other alloys is atomization because high production rates favor economy of scale and prealloyed powders can only be produced by atomization [23].

Atomization is simply the breakup of a liquid into fine droplets as discussed in Section 2.1.2.3. General types of atomization processes are listed below:

- Two – fluid atomization, where a liquid metal is broken up into droplets by impingement of high − pressure jets of gas, water, or oil (Figure 2.13 (a) and (b))
- Centrifugal atomization, where a liquid stream is dispersed into droplets by the centrifugal force of a rotating disk, cup, or electrode (Figure 2.13 (c))
- Vacuum or soluble − gas atomization, where a molten metal is supersaturated with a gas that causes atomization of the metal in a vacuum (Figure 2.13 (d))
- Ultrasonic atomization, where a liquid metal film is agitated by ultrasonic vibration (Figure 2.13 (e)) [23, 24].

Water, gas, centrifugal, ultrasonic, and soluble – gas atomization are all used in commercial production, but two – fluid atomization methods with gas (including air) or water account for more than 95% of atomization capacity worldwide [23].

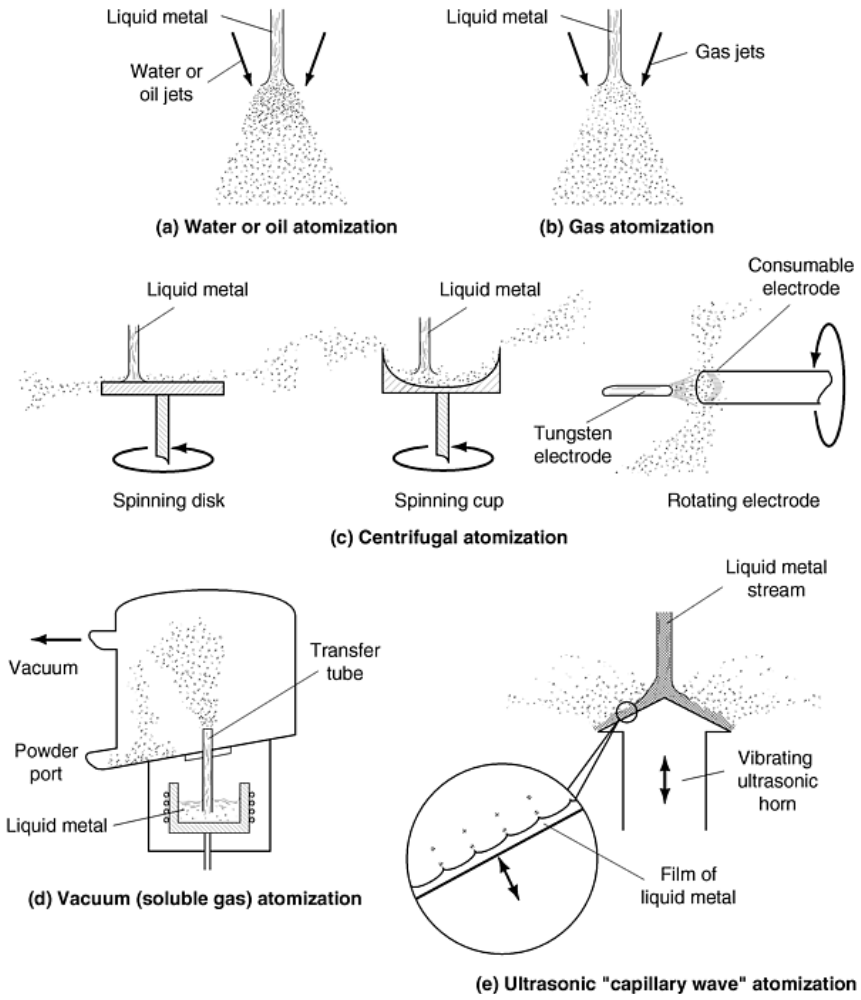

Figure 2.13 Atomization process [19].

In following sections, industrially applied methods of atomization are described.

2.2.1.4.1 Water Atomization

Metals and alloys that do not react with water can be water atomized only if it can be melted and poured satisfactorily. The low melting metals (below about 500 °C) are generally produced in this way because they give extremely irregular powders due to ultra rapid freezing, which is often undesirable. The reasons why water atomization is cheaper than the other methods of atomization are the low cost of the medium (water), low energy use for pressurization compared with gas or air, and

the very high productivity that can be achieved (up to 30 tons/h or about 500 kg/min). Nevertheless, powder purity and particle shape (especially for more reactive metals and alloys which generally give irregular powders of (relatively) high oxygen content) are the main limitations [19, 27].

A schematic flow sheet of water atomization is illustrated in Figure 2.14. A melting facility, an atomizing chamber, water pumping/recycling system, and water dewatering and drying equipment are the major components of a typical water atomization [19]. The molten metal is poured into a tundish. It supplies a uniform and controlled head of molten metal to the tundish nozzle which is a nozzle at the base of the tundish and controls the shape and size of the metal stream and directs it through an atomizing nozzle system in which the metal stream is disintegrated into fine droplets by the high – velocity water jets [20]. There are several variables involved in water atomization for the distinct stages of melting, atomization, and particle solidification (Figure 2.14). Many of these variables are interrelated, and each atomization unit is unique to some degree with specific operating conditions [19, 23].

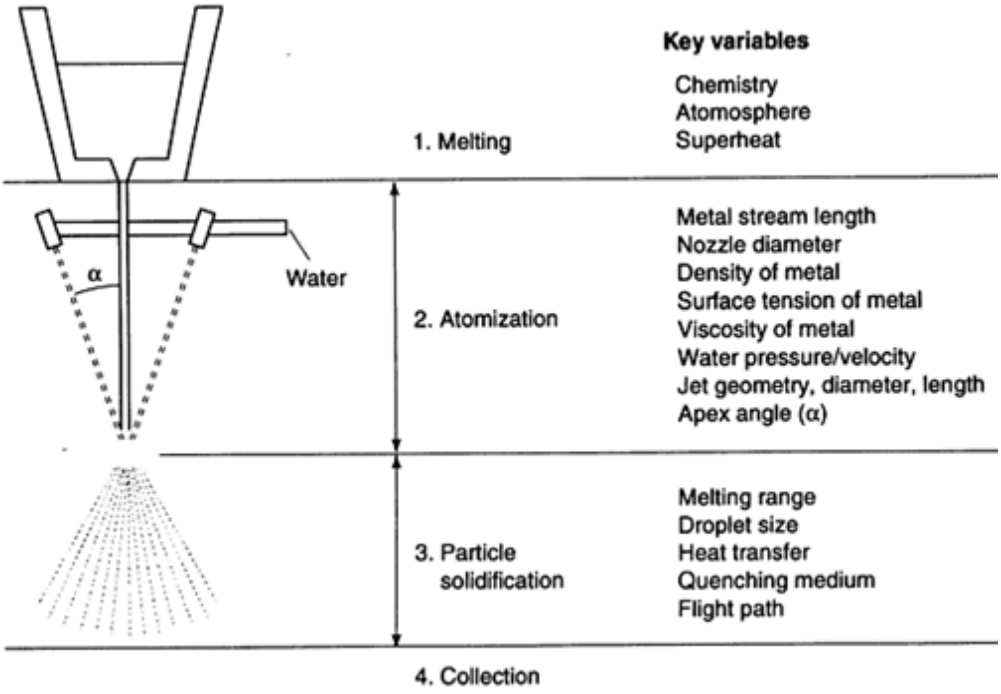

Figure 2.14 Stages in water atomization and associated process variables [23].

2.2.1.4.2 Oil Atomization

Liquids used in atomization of metal powders other than water is hydrocarbons. The problem of powder oxidation is solved by this method. Oil atomized powders are very similar to water atomized powders and both of them have very similar rates of cooling [20, 23].

2.2.1.4.3 Vacuum Atomization

Another important industrial atomization method is vacuum atomization. This method is based on the rapid expansion of gas – saturated molten metal. When a molten metal supersaturated with gas under pressure is exposed to vacuum, the gas expands and comes out of solution. This results in a fine spray of molten droplets. The energy for atomization is stored in the molten metal [20]. A schematic

representation of vacuum atomization is given in Figure 2.15. In vacuum atomization, there are two chambers. The alloy is melted and subsequently pressurized in the lower chamber while the upper chamber under vacuum serves as a collection tank for powders. The alloy is induction melted under vacuum with the use of conventional furnace and the molten metal is then pressurized with the mixture of inert and soluble gas (hydrogen) in the lower chamber. Then, the molten metal is atomized by ejecting the liquid stream into the upper vacuum chamber by means of siphon tube [19, 20, 23].

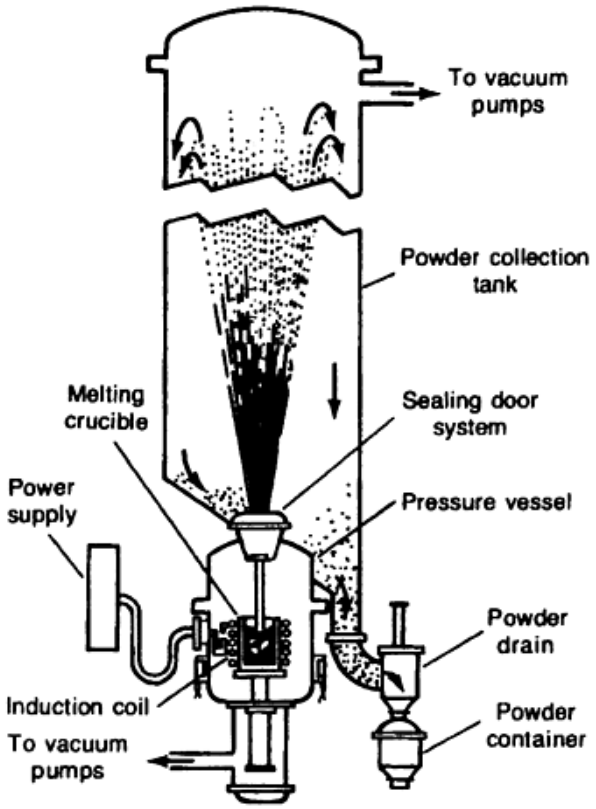

Figure 2.15 Vacuum atomization system [19].

2.2.1.4.4 Gas Atomization

The process where the liquid metal is disrupted by a high velocity gas such as air, nitrogen, argon, or helium is called gas atomization. The selection of gas is done due to the requirements determined by the metal to be atomized [25]. The liquid metal stream is disintegrated by kinetic energy transfer from the atomizing medium to the metal [15]. The process principles are similar to water atomization. With minor changes, Figure 2.14 can also be used to describe gas atomization.

Gas atomization is undertaken either in vertical or horizontal units. Vertical designs are very similar to water atomization units. Moreover, there are lots of horizontal designs where a vertical, inclined, or sometimes horizontal melt stream is atomized by essentially horizontal gas jets [25]. Gas atomizing units are classified as *confined* or *free – fall* nozzle configurations. These configurations are shown in Figure 2.16. In addition, *internal mixing* nozzle configuration, where the gas and metal are mixed before expanding into the chamber, is used [23].

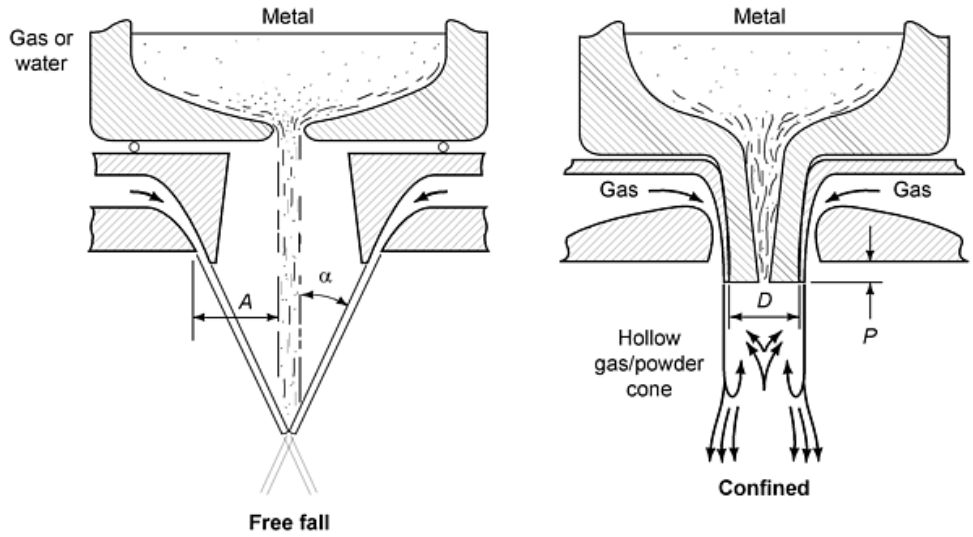

Figure 2.16 Two – fluid atomization with **(a)** free − fall design (gas or water) and **(b)** confined nozzle design (gas only) [19].

Free – fall gas units resemble the water atomizing units but in free – fall gas units, fine powder production is very difficult because of the rapid velocity decrease. On the other hand, in gas atomization, closed configuration is often used. This type is nominated in gas atomization for efficiency because the rapid decrease in velocity (and kinetic energy) of gas stream with distance from the nozzle are prevented [23, 25].

Air and nitrogen are commonly used for breakup of the liquid stream. Argon is chosen in order to minimize contamination. Also helium is preferred because it provides an inert atmosphere and rises the cooling rate of the droplets [23].

2.2.2 Powder Properties and Characterization

The properties of the final metallurgy parts are determined by the properties of the starting powders. Reliable techniques for powder characterization and testing are required to evaluate the chemical and physical properties of metal powders, both as individual particles and in bulk form. The representativity of samples taken to test metal powders is key to the characterization process.

The properties of a metal powder particle can be divided into two main categories, material properties and properties due to the process of fabrication. Material properties are structure, theoretical density, melting point, plasticity, elasticity, and purity (impurities). On the other hand, particle size, particle shape, density (porosity), surface conditions, microstructure, type and amount of lattice defects, gas content within a particle, adsorbed gas layer, amount of surface oxide, and reactivity are the properties due to the powder production methods [28].

Characteristics of a bulk powder are

- Particle size distribution
- Specific surface
- Apparent and tap density

- Powder flowability
- Compressibility [15, 25, 28, 29].

2.2.2.1 Particle Size Distribution

The properties of the final products made from powder are controlled by particle size and particle size distribution because they have an important effect on the behavior of metal powders during processing. Therefore, characterization of them is essential. Common particle size measuring techniques include sieve analysis, microscopy, Fraunhofer diffraction, neutron/X – ray scattering, sedimentation, electrical zone sensing [19, 25].

2.2.2.2 Surface Area

An average measure of the external condition of a large number of particles is called surface area. It is a useful property because it correlates with various characteristics and it also provides insight into the powder behavior during chemical activity, catalysis, friction, adsorption, contamination, pressing and sintering. Gas adsorption and gas permeability are two main analysis systems [15].

2.2.2.3 Apparent Density and Tap Density

Apparent density, which is defined as the weight of a unit volume of loose powder expressed in grams per cubic centimeter, is one of the fundamental properties of a powder. It affects processing parameters such as the design of compaction tooling and the magnitude of the press motions required to compact and densify loose powder. The most common methods for determining apparent density of metal powders use the Hall flowmeter and the Scott volumeter [19, 25].

Tap density is defined as the apparent density of a powder packed vertically by vibration. Tapping or vibrating a loose powder provides movement and separation and lowers the friction between the powder particles. Tap density is always higher

than the free – flow apparent density. Tap density is a function of particle shape, particle porosity, and particle size distribution. The amount of increase from apparent to tap density depends on mainly particle shape. Usually, the lower the apparent density, the higher the percentage increases in density on tapping [19, 25].

2.2.2.4 Powder Flowability

Flowability is determined with the use of the Hall flowmeter. The measured parameter is the flow time required for 50 g of powder. Short flow times indicate free flowing powders whereas long times indicate high interparticle friction [15, 25].

2.2.2.5 Compressibility

The ability of densification of bulk powders in terms of compact density and compaction pressure is named as compressibility. Compressibility of a powder is a major factor in the design of pressing tools, the part density attainable, and the size of press needed. A more compressible powder can be compacted to a higher density and, consequently, permits the manufacture of parts possessing higher mechanical properties or the use of a smaller and less expensive compaction press [25].

2.2.3 Powder Shaping and Consolidation

Several methods that range from high pressure die compaction to pressureless shaping methods like slip casting are used for powder metallurgy parts. In all these methods, consolidation of powders into useful forms is the main purpose. The selection of a shaping or consolidation method involves the type of powder to be used (i.e., spherical, sponge, flake), the chemistry of the powder (i.e., prealloyed, elemental blend, partially alloyed), the use of rigid or flexible tools, the use of a binder or lubricant, the use of a directed powder spray to directly consolidate the powder as it is being made [19].

This section briefly explains powder shaping and consolidation methods used in this study, cold compaction and hot extrusion.

The most commonly used compaction process is cold compaction in rigid dies. In the cold compaction process, which is shown schematically in Figure 2.17, a die cavity of desired geometric shape is filled with powder. Then, a movable punch seals the die cavity, and a load is then applied via the advancing punches. The pressure causes the metal powder particles to mechanically interlock and cold weld together into a porous mass of the approximate shape and dimensions desired for the final component. The powder is densified from both top and bottom planes, and the middle plane has the lowest density. This as – pressed shape is commonly named as the green part [15].

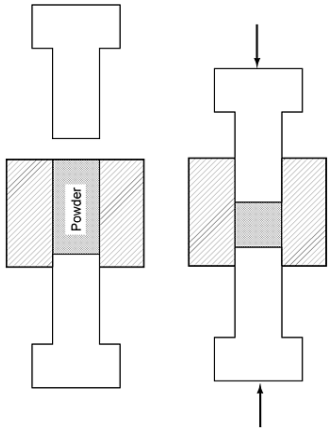

Figure 2.17 Schematic representation of the die compaction process [19].

For generating long and thin structures such as tubes and rods, extrusion is the most appropriate process. There are two main types of extrusion mechanisms, direct and indirect or inverted [28]. These can be shown in Figure 2.18.

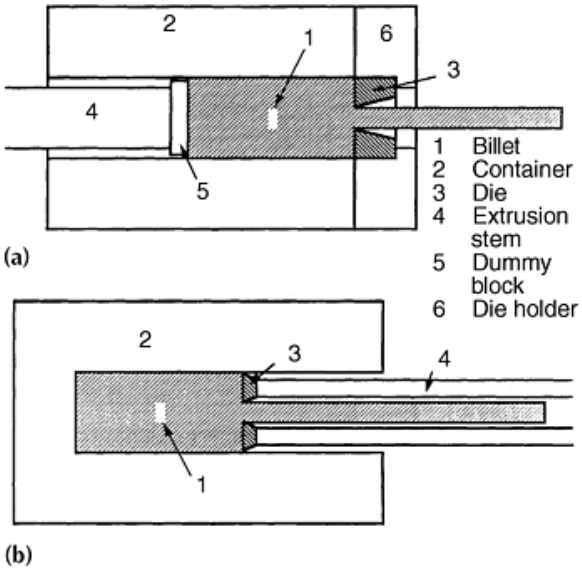

Figure 2.18 Basic methods of extrusion **(a)** Direct extrusion, **(b)** Indirect extrusion [19].

In order to produce a densified and elongated form having structural integrity, direct extrusion processing where metal powders undergo plastic deformation (usually at an elevated temperature) is generally used. Three main approaches to extrusion of powders are given in Figure 2.19. In this study, the third approach is used. Canning is employed because of isolation of the principal material from the atmosphere and extrusion lubricants (clean extrusion technique), encapsulation of spherical and other difficult to compact powders to produce a billet form, improved lubricity and metal flow at the die interface by proper selection of the can material, isolation of the principal material from the extrusion die and region of highest shear, which is an important consideration for materials with limited ductility, and the ability to position powder and solid components within the can to produce unique and complex shapes [15, 19, 28, 30].

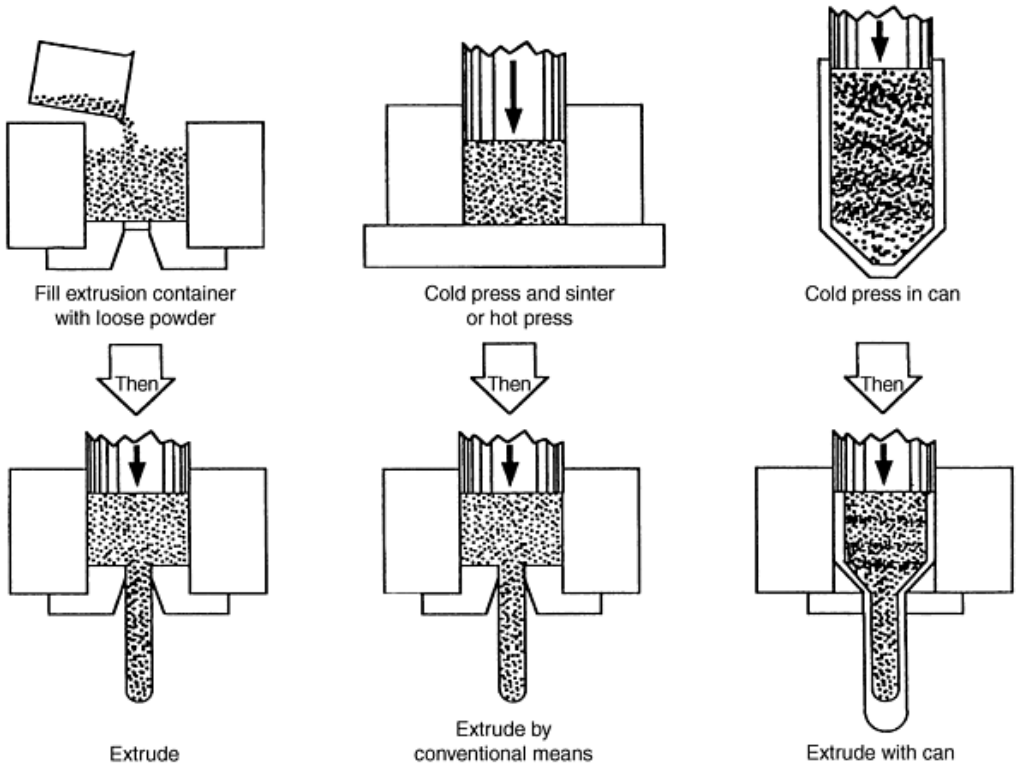

Figure 2.19 Hot extrusion methods for metal powders [19].

2.3 Advanced Aluminum Powder Metallurgy Alloys

Much finer and homogeneous microstructure, better mechanical properties, and near – net shape parts producibility for aluminum alloys in comparison with ingot metallurgy (I/M) are provided by P/M processing. Emerging technologies of advanced aluminum P/M alloys such as mechanical alloying and RS provide significant improvements in room and elevated temperature strength, fracture toughness, fatigue life, and corrosion resistance. Some examples of advanced aluminum P/M alloys and their compositions are given in Table 2.3.

Table 2.3 Chemical composition of aluminum P/M alloys [19].

Alloy Designation	Composition
Al – Cu – C	Al – 1.0Ci – 1.5C
Al – Mg – C	Al – 2.0Mg – 1.5C
Al – C r – X	Al – 5.0Cr – 2.0Zr – 1.0Mn
Al – Ti – X	Al – 3.0Ti – 3.0Ce
Al – Be – X	Al – 22.6Be – 10.8Li
201AB	Al – 4.4Cu – 0.8Ci – 0.5Mg – 1.5 other
201AC	Al – 4.4Cu – 0.8Si – 0.5Mg
202AB	Al – 4.0Cu – 1.5 other
601AB	Al – 0.25Cu – 0.6Si – 1.0Mg – 1.5 other
601AC	Al – 0.25Cu – 0.6Si – 1.0Mg
602AB	Al – 0.6Mg – 0.4Si – 1.5 other
MD – 76	Al – 5.6Zn – 2.5Mg – 1.6Cu
7090	Al – 8.0Zn – 2.5Mg – 1.0Cu – 1.5Co – 0.35O
7091	Al – 6.5Zn – 2.5Mg – 1.5Cu – 0.4Co
X7093	Al – 9.0Zn – 2.2Mg – 1.5Cu – 0.14Zr – 0.10Ni
8009	Al – 8.5Fe – 2.4Si – 1.3V
X8019	Al – 8.3Fe – 4.0Ce
Al – Fe – Ce	Al – 8.0Fe – 3.5Ce – 0.35O
Al – Fe – Co	Al – (3-8)Fe – (2-7)Co – 0.35O
Al – Fe – Ni	Al – 8Fe – 1.7Ni
Al – Fe – Mo	Al – 8.0Fe – 2.0Mo
Al – Li – Cu	Al – (2-3.5)Cu – 0.5Mg – 0.6Mn – (2.5-3.2)Li
Al – Mn – Co	Al – (3-8)Mn – (1.5-7)Ni
Al – Mn – Ni	Al – (3-8)Mn – (1.6-6.5)Co
Al – Ni – Co	Al – (2-5)Ni – (2-5)Co

The P/M route for producing advanced aluminum alloys involves blending elemental or prealloyed powder with the binder, followed by canning, vacuum degassing, and some form of consolidation, such as hot pressing or hot isostatic pressing (HIP), into a billet that is subsequently rolled, forged, or extruded into shapes. In addition, deformation processing (extrusion, forging, or rolling) of the consolidated powders develops the best properties attainable by breaking up any preexisting oxide on the alloyed powder [19].

There are two main types of strengthening mechanism of advanced aluminum P/M alloys: precipitation and dispersion strengthening [3, 31]. *Precipitation strengthening* is the general mechanism for most of the aluminum alloys for their strength. Precipitation strengthened aluminum alloys contain some intermetallic dispersoids but they are strengthened during the formation of precipitates that are formed through heat treatments which are given after powder consolidation and forming. The other mechanism, *dispersion strengthening*, directly depends on dispersoids which are responsible for high temperature strength and creep. These alloys have no I/M analogue [14].

2.4 Rapidly Solidified Al – Fe – V – Si Alloy

Dispersion – strengthened Al – Fe – V – Si alloys produced by RS for elevated temperature applications such as aerospace structures, heat engineering, and automobile industry have been greatly developed in recent years because these alloys represent a new class of structural material with excellent room and high temperature strength, fracture toughness and low coarsening rate of dispersoids [4, 32]. The high temperature strength of these alloys is due to low diffusivity and limited solubility of the alloying elements (Fe and V) in Al [3, 11, 33]. RS leads to the formation of several stable and metastable phases in Al – Fe – V – Si alloys [34]. Wang et al. [4] showed that the driving force for particle coarsening is minimized by the low solid state diffusion of Fe and V in Al and the role of V in reducing the interfacial energy between the dispersoids and matrix minimize. Thus, particle stability increases at temperature up to 510 °C.

2.4.1 Microstructure of RS Al – Fe – V – Si Alloy

There are three types of microstructure in as – atomized powders. These are *zone A*, *zone B*, and *zone C* [6, 10, 35]. The microstructure of *zone A* consists of very fine and homogeneously distributed precipitates in α – Al matrix. The regions consisting of microcellular structures is described as the *zone B* while the *zone C* is composed of the regions consisting of coarse cellular structures and globular quasicrystalline phase particles [10]. Cooling rate and composition of alloy have an important influence on types of microstructure [6]. In the investigation of Tongsri et al. [10], both *zone A* and *zone B* microstructures was present in fine powder particles and the size of *zone A* decreased with increasing powder particle size. They also reported that microstructure of coarse powder particles exhibited both *zone B* and *zone C*. The intercellular phases of Al – Fe – V – Si in *zone B* were very fine, randomly oriented microquasicrystalline icosahedral particles whereas the intercellular phases of Al – Fe – V – Si powders in zone C were silicide phase [6, 10, 32]. Figure 2.20 illustrates the microstructures and their thermal stability.

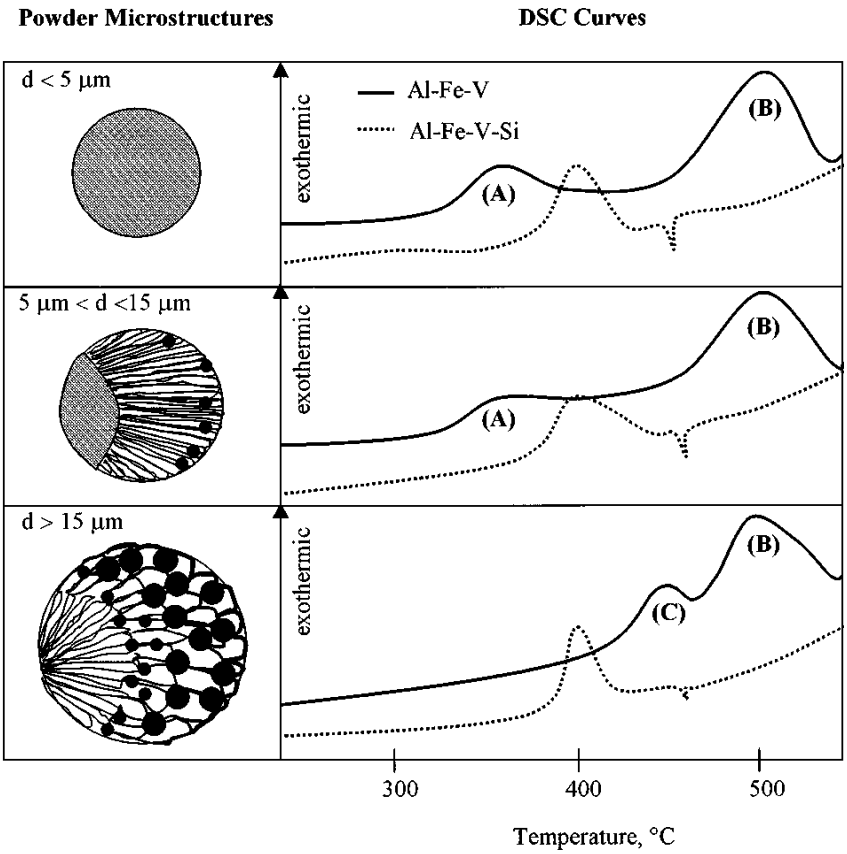

Figure 2.20 Schematic diagram showing microstructures and DSC curves of Al – Fe – V – Si powder particles [10].

Formation of these zones is explained by the interactions between the growing α – Al fronts with the freely dispersed, primary phase particles. The formation of *zone A* is due to advancing planar α – Al into the melt and engulfing the ultra fine dispersed microquasicrystalline particles (Figure 2.21 (a)). In *zone B* (in medium sized powders (5 – 15μm)), the planar front is not stable at velocities below the absolute velocity and turns into cellular front and freely dispersed microquasicrystalline phase particles pushed laterally by the cellular front and entrapped in the intercellular liquid that solidifies later at the end of the solidification of a melt droplet (Figure 2.21 (b)). In *zone C*, the cellular α – Al front changed to a dendritic mode. The globular particles are as large as the cellular or primary dendrite arm spacing. Thus, they are not trapped in the intercellular/interdendritic regions [10].

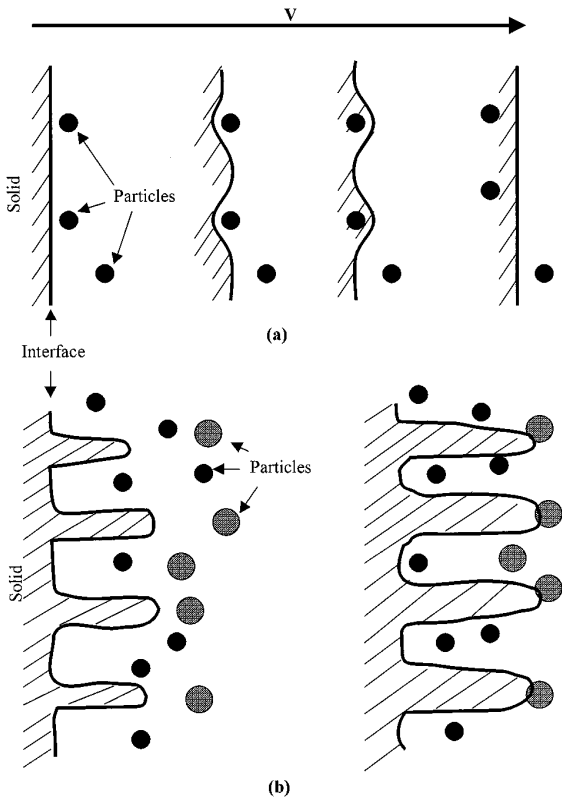

Figure 2.21 Schematic diagram showing interaction between second phase particles and planar **(a)** and cellular **(b)** solidification fronts [10].

Second phases were investigated in the strip – cast and spray – cast Al – Fe – V – Si alloy by Koh et al. [32]. They showed that there are three types of second phases, namely icosahedral, bcc α – AlFeSi, newly found hexagonal phase. Furthermore, Yaneva et al. [11] found that as – cast and annealed Al – Fe – V – Si alloy ribbon produced by PFC have a two – phase microstructure, which are supersaturated aluminum matrix and quaternary silicides. The overall stability of RS Al – Fe – V – Si alloy is due to the presence of a high amount of small rounded dispersoids ($Al_{12}(Fe, V)_3Si$) that prevent recrystallization, grain growth and dislocation accumulation [36]. Wang et al. [4] demonstrated that Al – Fe – V – Si alloy produced by PFC has bcc α – $Al_{13}(Fe, V)_3Si$ phase precipitates which are mainly distributed along grain boundaries. Moreover, the homogeneous distribution of fine dispersoids improves recrystallization temperature and prevents the growth of grains.

2.4.2 Mechanical Properties of RS Al – Fe – V – Si Alloy

The mechanical properties of rapidly solidified Al – Fe – V – Si alloys and their products at elevated temperatures are mainly dependent on the thermal stability of microstructures and/or phases [10]. A cubic intermetallic phase that is $Al_{13}(Fe, V)_3Si$ is responsible for high temperature strength in these alloys [8, 37]. These rounded intermetallics that homogeneously distributed throughout the matrix is shown in Figure 2.22. In addition, Prakash et al. [9] revealed that the extrusion microstructure of Al – 8Fe – 1V – 2Si (in wt%) consisted of alternate bands of regions containing fine and coarse dispersoids. This banded structure is given in Figure 2.23.

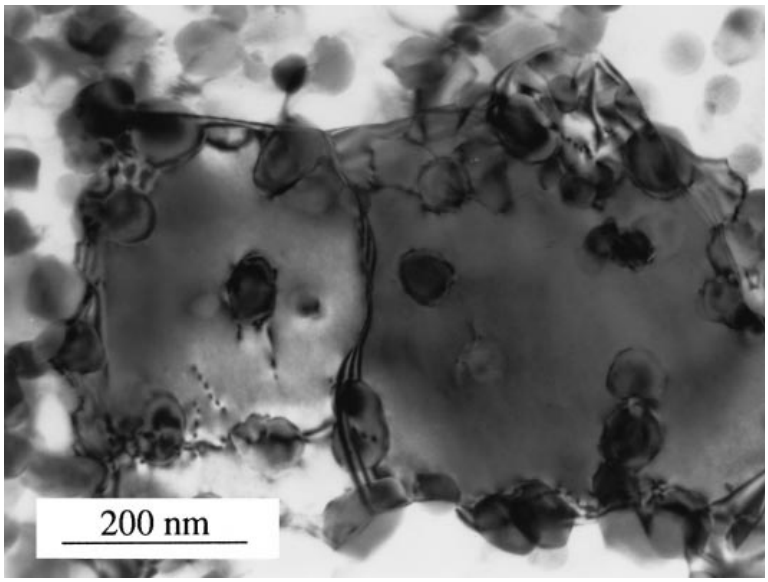

Figure 2.22 TEM micrograph showing the microstructure of the as-received rolled Al – 8.5Fe – 1.3V – 1.7Si (in mass %) [36].

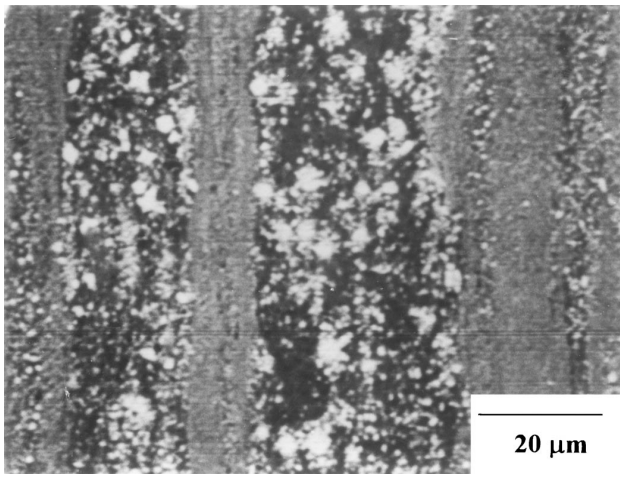

Figure 2.23 Backscattered electron micrograph showing the microstructure in Al – Fe – V – Si extrusions [9].

Wang et al. [38] studied the effect of particle size and characteristics of the powder and flakes on mechanical properties. They reported that the improvement of mechanical properties is the result of high cooling rate and low level of surface oxidation. Mechanical properties of extruded alloys are given in Table 2.4. Also, they emphasized that small particle size causes high strength and low ductility. Low ductility is attributed to the large surface area of small particles and it results in a high level of surface oxidation.

Table 2.4 Mechanical properties of the extrudes made from the powder and powder deposited flakes (PDF) [38].

Nominal Composition	**Mean Diameter (μm)**	**Room Temperature**			**623 K, 30 min**		
		σ_{UTS} (MPa)	$\sigma_{0.2}$ (MPa)	Δl (%)	σ_{UTS} (MPa)	$\sigma_{0.2}$ (MPa)	Δl (%)
Al – 6Fe – 1Si – 2V	Powder, 20	328	264	14	/	/	/
Al – 8Fe – 1Si – 2V	Powder, 20	465	406	8	270	242	7
Al – 8Fe – 1Si – 2V	Powder, 20	402	342	10	245	204	8
Al – 8Fe – 1Si – 2V	PDF	447	388	12	259	217	9

Yan et al. [39] in their study stated that the total elongation to fracture increases not only with increasing temperature but also with increasing strain rate. The dependence of elongation on the strain rate may be due to the presence of a transition from plastic instability at lower strain rates to stable deformation at higher strain rates for the fine grained materials produced by spray deposition. Figure 2.24 represents the variation of total elongation with test temperature at different strain rate for FVS0812 aluminum alloy sheet.

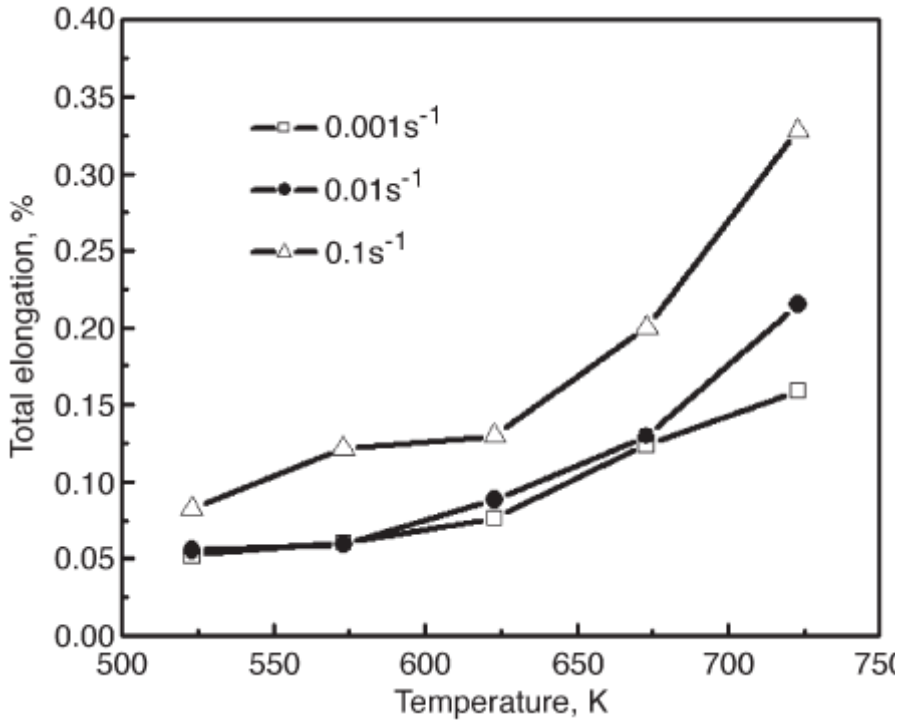

Figure 2.24 The variation of total elongation with test temperature at different strain rate for FVS0812 aluminum alloy sheet [39].

In the investigation of Carreno et al. [40], the high temperature behavior of two Al – Fe – V – Si alloys, which were processed by the same method, was studied. These alloys were Al – 8.5Fe – 1.3V – 1.7Si and Al – 11.7Fe – 1.2V – 2.4Si and they contained high volume fractions of precipitates: 27% and 36%, respectively. They concluded that improved high temperature creep properties can be obtained in

aluminum alloys containing a high volume fraction of fine dispersoids that hinder the movement of dislocations.

The fracture mode of rapidly solidified Al – Fe – V – Si alloys is ductile rupture regardless of the test temperature and strain rate. The dimples are distributed throughout the fracture surface, which indicate that void nucleation, growth and coalescence is the failure micromechanism. The presence of dimples indicates that the samples have good ductility and they fracture in a ductile style [9, 30, 39, 41]. Typical fracture surfaces of rapidly solidified Al – Fe – V – Si alloys is given in Figure 2.25.

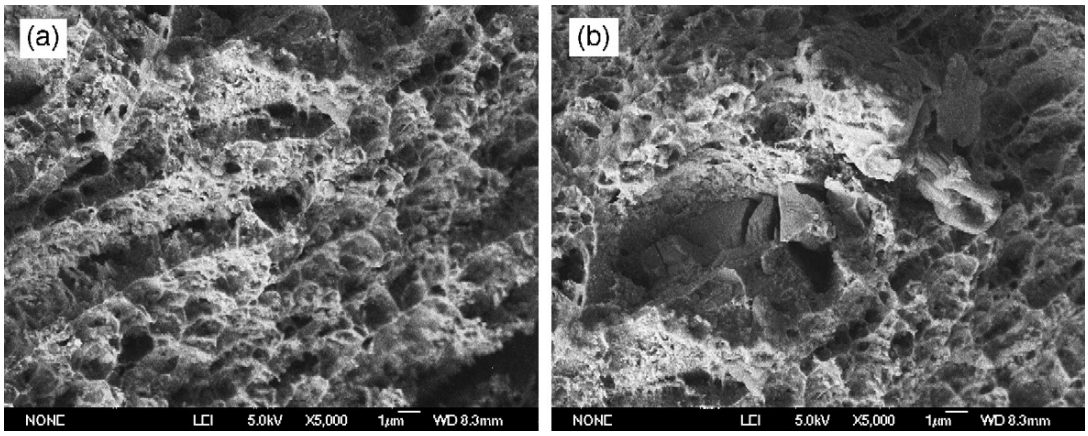

Figure 2.25 Fracture morphologies of the samples in different tensile deformation conditions **(a)** 300 °C, 0.001 s^{-1} and **(b)** 300 °C, 0.001 s^{-1} [39].

CHAPTER 3

EXPERIMENTAL PROCEDURE

The Al – Fe – V – Si alloys studied in the present study were produced through powder metallurgy route of atomization, cold compaction and extrusion. The properties of powders were investigated by screen analysis, SEM, DTA, XRD, and Hall flowmeter. The microstructural and mechanical characterization of the alloys produced from different powder particle size ranges and extrusion ratios was performed by optical microscopy, SEM, XRD, tensile and hardness test machine. Also, the effects of powder particle size and extrusion ratio on microstructure and mechanical properties were examined.

3.1 Production of Hot Extruded Al – Fe – Si – V Alloys

3.1.1 Alloy Preparation

The alloy used in the present study was Al – 8 Fe – 1.7V – 7.9Si (all compositions are in wt%) alloy. The alloys were prepared in an induction furnace under air atmosphere by melting of 99.7% purity Al with Fe, Fe – 75%V master alloy, and Si, which were weighed in a Denver Instrument SI – 6002 (6000g × 0.01g), in a clay bonded graphite crucible at 850 – 870 °C. Sufficient time was given after melting for complete homogenization. Then, the molten alloy was poured in graphite moulds to obtain ingots.

3.1.2 Powder Production

The alloy ingots were remelted in the induction furnace at 900 °C and the molten alloy was poured into electrical resistance holding furnace that was heated up to 900

°C because the melt must be superheated over the melting temperature. A horizontal atomization chamber was positioned in front of electrical resistance furnace to collect rapidly solidified powders. The chamber has dimensions of 8×2×3 m to allow enough time for the powder particles to solidify before striking the walls. Figure 3.1 shows the air atomization chamber used for powder production in Foundry and Solidification Laboratory of Department of Metallurgical and Materials Engineering, METU.

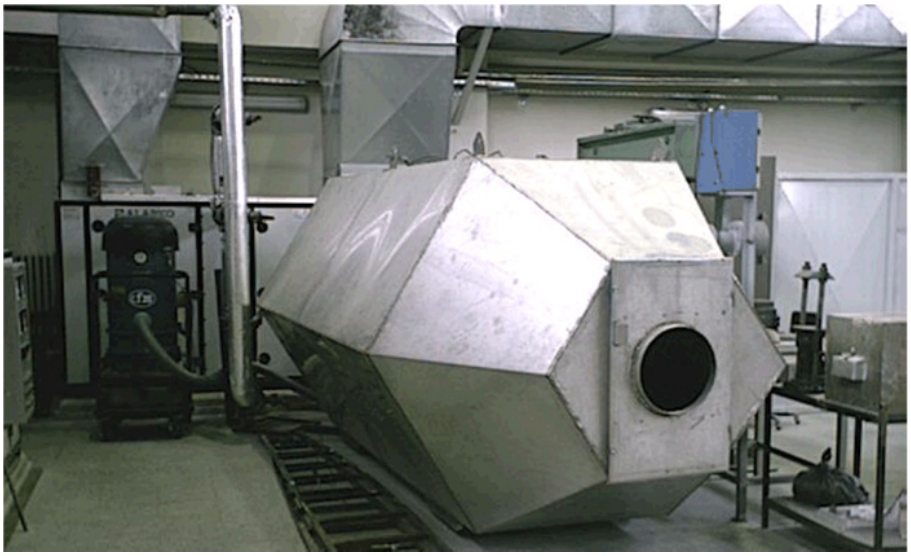

Figure 3.1 Air atomization chamber used for powder production.

Horizontal air atomization technique was carried out to produce air atomized Al – Fe – V – Si powders. A schematic diagram of experimental setup is given in Figure 3.2. The melt was atomized into micrometer sized powders using compressed air having a pressure of 26.65 atm into the atomization chamber. Powders were collected from the chamber and ultra fine powders were collected by vacuum.

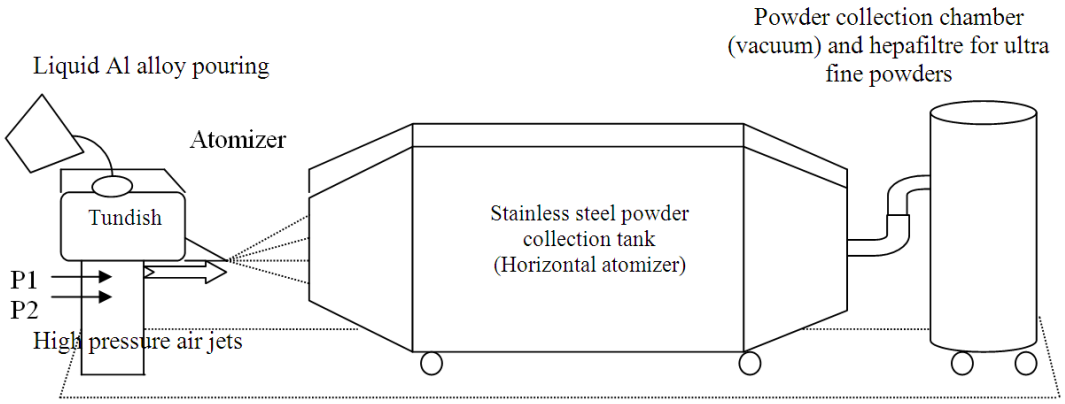

Figure 3.2 A schematic diagram of the horizontal gas atomizer at METU utilized during experiments.

3.1.3 Screening

The atomized alloy powders were sieved to obtain powders of various size fractions. Screen analysis of these powders was made by using screens that have meshes ranging from 38 μm to 212 μm. The opening sizes for the used series of screens appear in Table 3.1. The powder (a sample size of 100 g) was loaded onto the top of screen and the screen stack is agitated for a period of 15 minutes. After vibration, the powder in each size interval was separated. Retsch AS 200 sieve shaker, which is shown in Figure 3.3, was used for separation.

Table 3.1 Sieve sizes that were used in screening.

Mesh Size	Opening (µm)
70	212
100	150
140	106
170	90
200	75
270	53
400	38

Figure 3.3 Sieve shaker.

The SEM micrographs of sized powders are given in Figures 3.4 through 3.10.

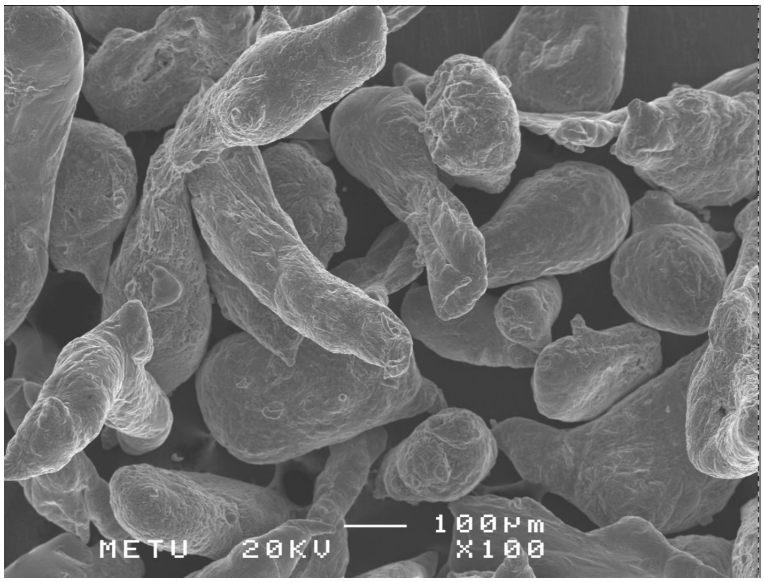

Figure 3.4 SEM micrograph of air atomized Al – Fe – V – Si powders that were between 212 and 150 μm in size (−212+150 μm).

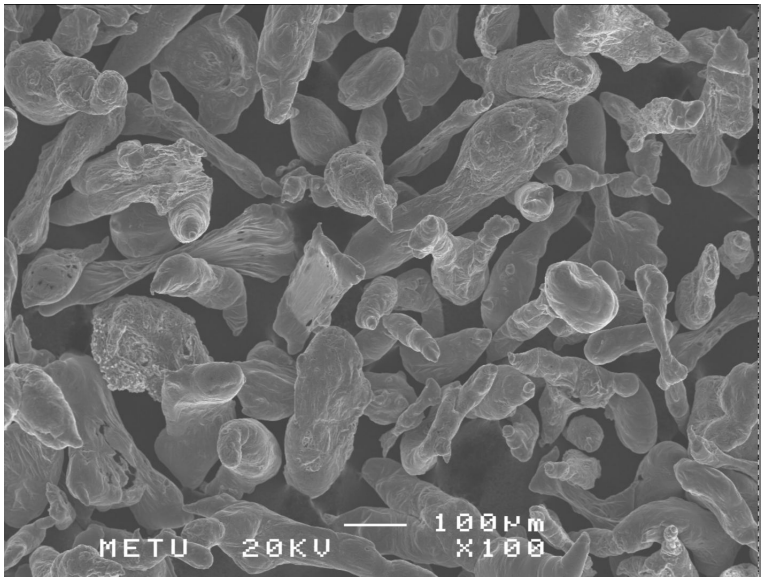

Figure 3.5 SEM micrograph of air atomized Al – Fe – V – Si powders that were between 150 and 106 μm in size (−150+106 μm).

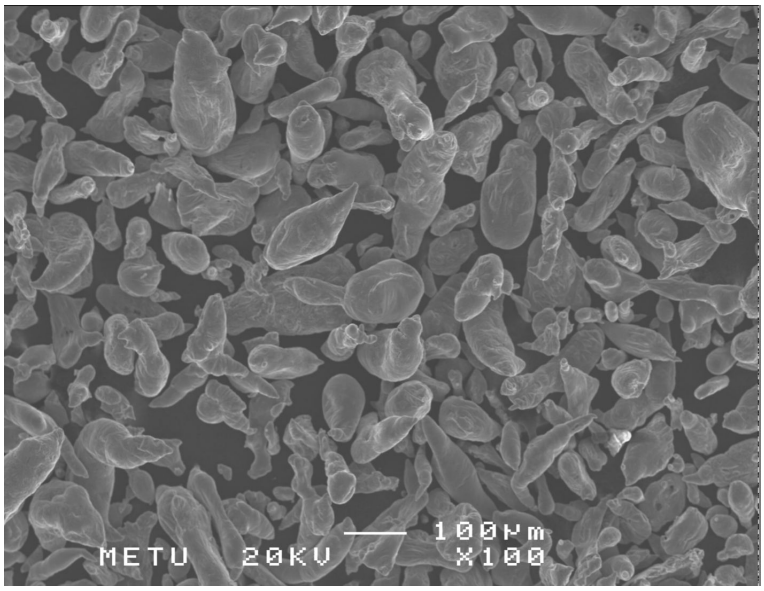

Figure 3.6 SEM micrograph of air atomized Al – Fe – V – Si powders that were between 106 and 90 μm in size (−106+90 μm).

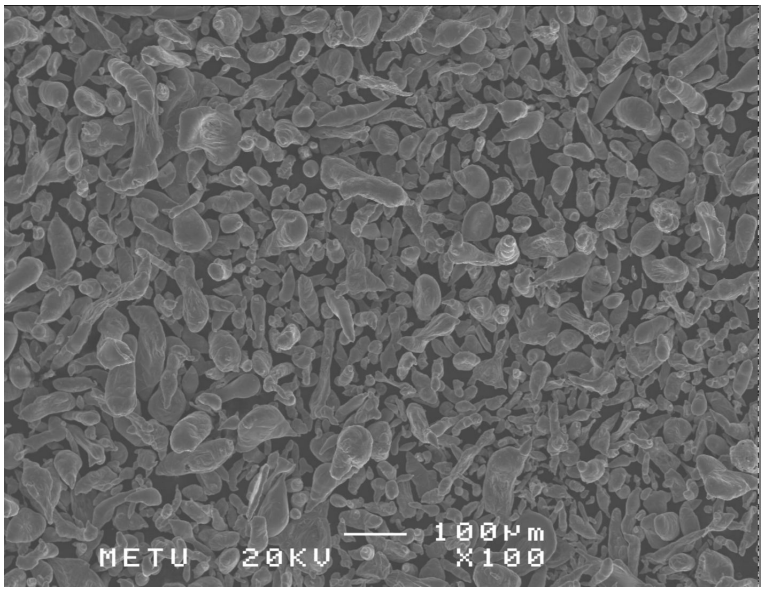

Figure 3.7 SEM micrograph of air atomized Al – Fe – V – Si powders that were between 90 and 75 μm in size (−90+75 μm).

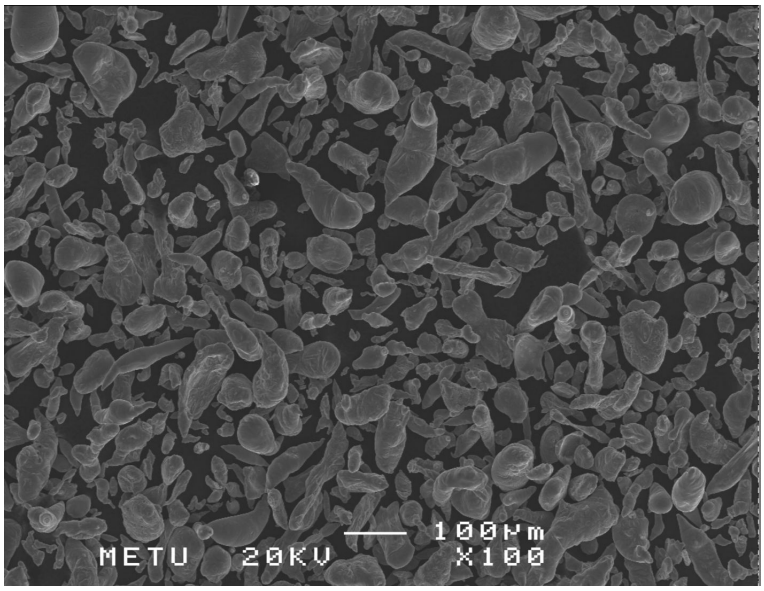

Figure 3.8 SEM micrograph of air atomized Al – Fe – V – Si powders that were between 75 and 53 μm in size (−75+53 μm).

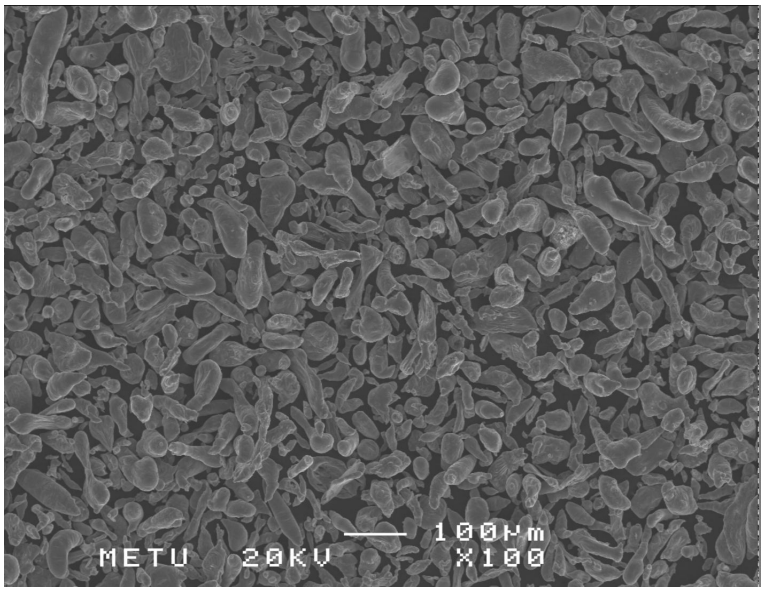

Figure 3.9 SEM micrograph of air atomized Al – Fe – V – Si powders that were between 53 and 38 μm in size (−53+38 μm).

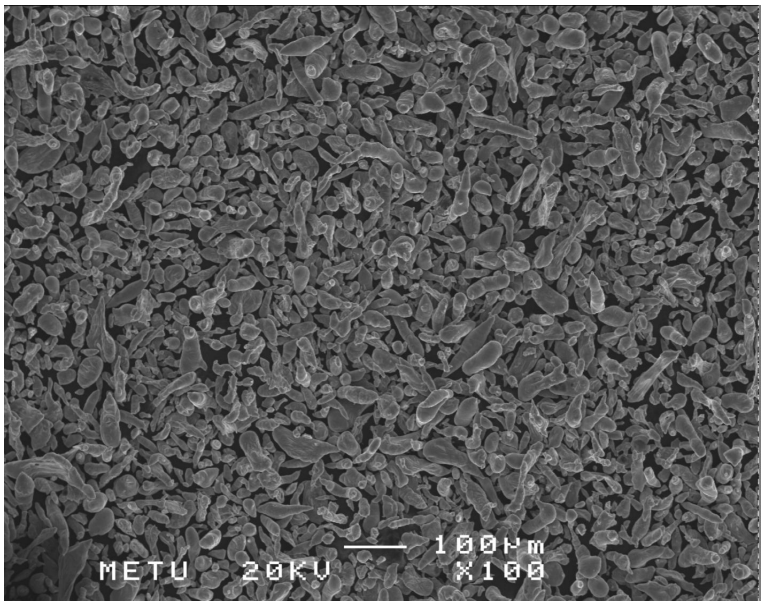

Figure 3.10 SEM micrograph of air atomized Al – Fe – V – Si powders that were below 38 μm in size (−38 μm).

3.1.4 Blending and Mixing of Powders with Binders

In the present study, seven different types of extrusion billet were produced according to various ranges of particle sizes and extrusion ratios. These particle size ranges were –2000+212 μm, −212+150 μm, −150+106 μm, −106+90 μm, and −90 μm. The first four ranges were attained after sieving so blending was not required. However, in order to obtain the last one, powders with several particle sizes were blended after screening. The weight percentages of these five ranges are given in Table 3.2.

Table 3.2 Weight percentages of five different particle size ranges.

–2000+212 µm	100% −2000+212 µm
–212+150 µm	100% −212+150 µm
–150+106 µm	100% −150+106 µm
–106+90 µm	100% −106+90 µm
–90 µm	50% −90+75 µm + 29% −75+53 µm + 15% −53+38 µm + 6% −38 µm

Powder size distribution of air atomized powders < 90 µm is demonstrated in Figure 3.11.

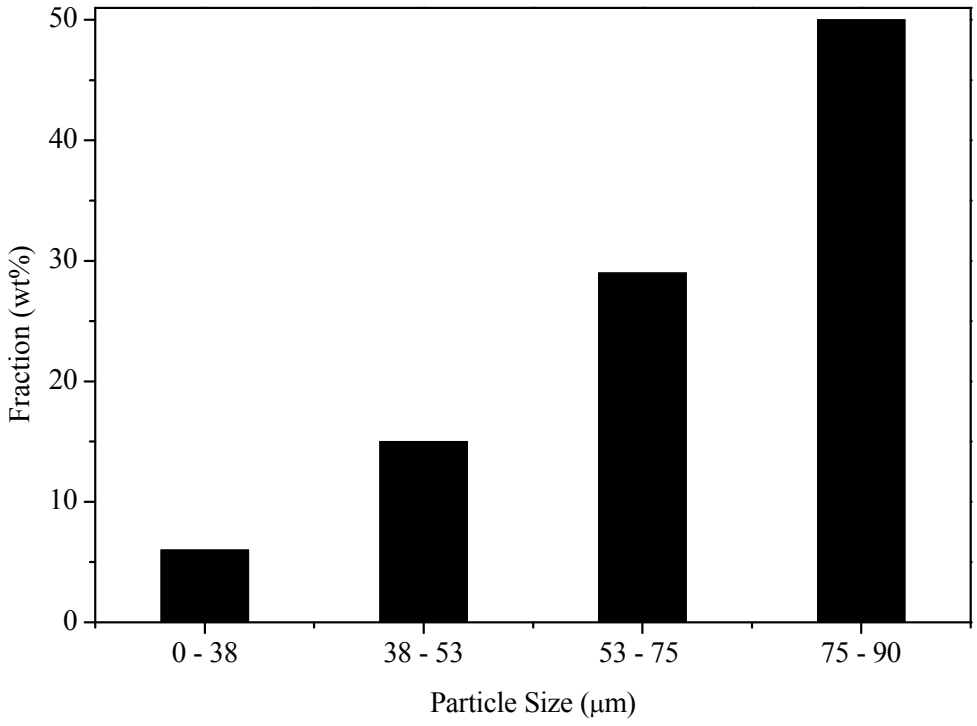

Figure 3.11 Powder size distribution of Al – 8Fe – 1.7V – 7.9Si alloy produced by air atomization of powder size < 90 µm.

Powders also were mixed with binders because as particle sizes decrease, compaction becomes more difficult. The use of binders was not essential for the first three particle size ranges but the last two ranges involved the use of binders. Polyethylene glycol (PEG) 8000 was used as a solid binder for the preparation of powders that were between 106 and 90 μm and below 90 μm. The physical and chemical properties of PEG 8000 are shown in Table 3.3. Powders and polyethylene glycol were mixed in plastic container with steel balls at high energy mixing condition for 30 minutes at a medium vibration. Also, ethyl alcohol was added to powder – binder mixture before compaction.

Table 3.3 Physical and chemical properties of PEG 8000.

Form	Crystalline powder or flakes
Color	White
Odor	Not available
Melting Point	63 °C
Boiling Point	Not available
Ignition Temperature	395 °C
Flash Point	270 °C
Density	1.21 g/cm^3
Thermal Decomposition	> 220 °C

3.1.5 Cold Compaction and Canning

Al – Fe – V – Si alloy powders were cold compacted in a steel die with top and bottom punches used to apply the desired pressure. The upper punch applied ~ 108 MPa whereas the lower one applied ~70 MPa. In cold compaction, irregularly shaped powders are used to ensure adequate green strength and structural integrity of the as – pressed product because during cold compaction the powder particles mechanically interlock with each other. Also, lubrication is essential to reduce

friction between the pressed compact and the rigid tool components when compacting metal powders in steel die so zinc stearate was used as lubricant. After compaction, Al – Fe – V − Si alloy powder compacts were produced and they were 90 mm in diameter and 25 mm in height. These tablets are shown in Figure 3.12.

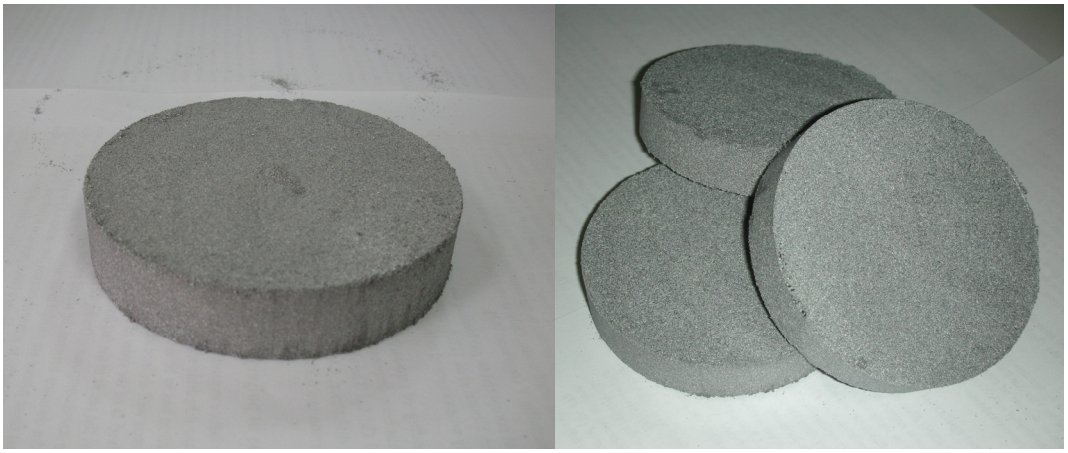

Figure 3.12 Compacts made from Al – Fe – V – Si alloy powders by cold compaction.

Extrusion billets were made by canning the compacts in suitable metal container. The selected containers were 6XXX series aluminum tubes, which were 108 mm in diameter and 350 mm in height, for five different size ranges with various extrusion ratios. The bottom openings of these tubes were closed by tungsten inert gas (TIG) welding method and the compacts were placed in the tubes. A schematic drawing of canning is given in Figure 3.13. Then, the top openings of the tubes were again closed by TIG welding. Also, some holes were drilled on the top of tubes in order to remove residual air. An extrusion billet composed of compacts is demonstrated in Figure 3.14.

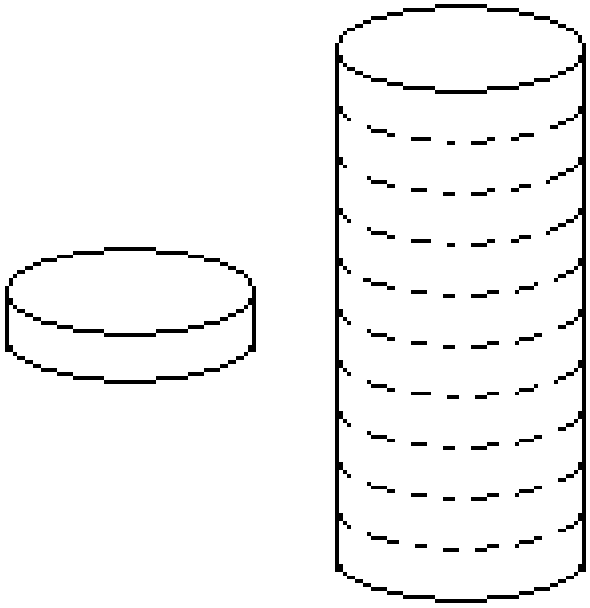

Figure 3.13 A schematic drawing of canning.

Figure 3.14 The extrusion billets composed of compacts.

3.1.6 Hot Extrusion

The billets composed of cold pressed compacts were preheated at 350 – 380 °C and extruded at 455 – 480 °C in the direct extrusion mode to obtain continuous bars of Al – Fe – V – Si powders. Extrusion was carried out in a horizontal acting 1100 ton press with a ram speed of 5 mm/s in OSKO Aluminum. The extrusion machine is shown in Figure 3.15.

Figure 3.15 Extrusion machine, OSKO Aluminum, Ankara, Turkey.

There were three different extrusion ratios (144 to 1, 81 to 1, and 26 to 1) used in this study. The first one (144:1) was only used for the billet that was made from –2000+212 μm powders. The extrusion ratio of 81 to 1 was used for the billets that were made from all powder size fractions except for −2000+212 μm powders. The billets composed of –212+150 μm and –150+106 μm powders also extruded with an extrusion ratio of 26 to 1. The formula used for extrusion ratio, R calculation is as follows:

$$R = \frac{A_0}{A_f} \tag{3.1}$$

where A_0 is the initial cross sectional area of the billet and A_f is the final cross sectional area after extrusion. Hot extruded continuous rods are shown in Figure 3.16.

Figure 3.16 Examples of continuous rods after hot extrusion.

Figure 3.17 demonstrates the followed route starting from the alloy preparation step to the characterization of the hot extruded alloy.

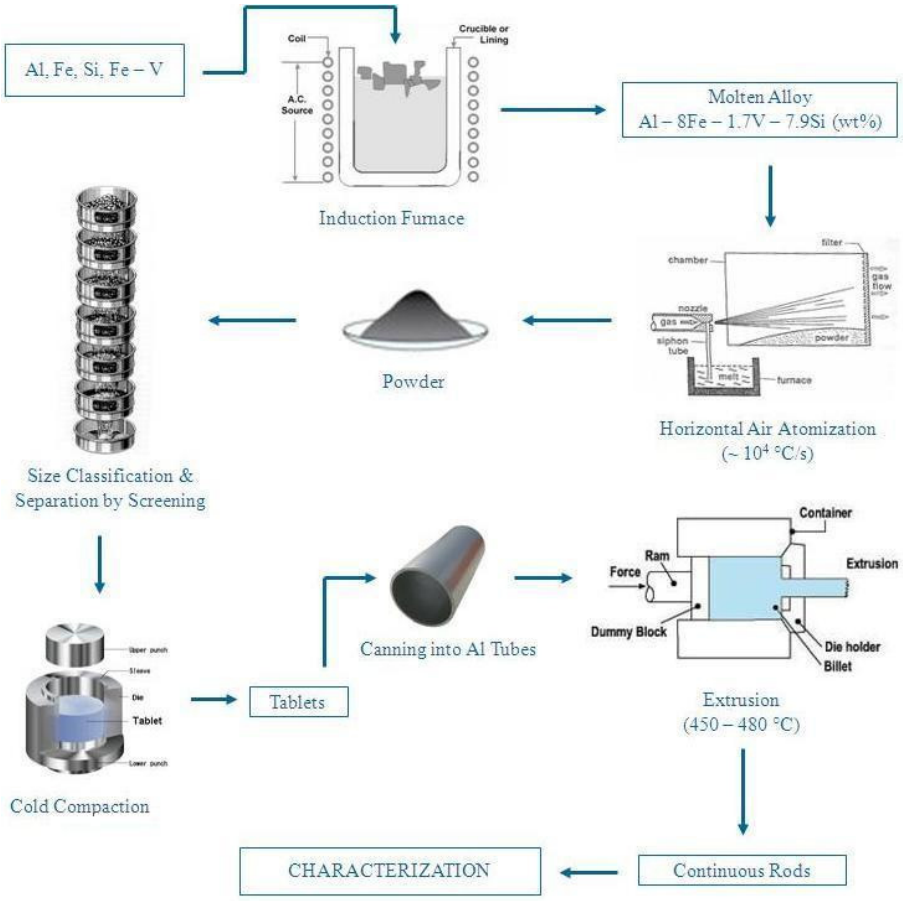

Figure 3.17 The flow chart for the processing of high performance Al – Fe – V – Si alloy.

3.2 Characterization

3.2.1 Hall Flowmeter Analysis

The interparticle friction was measured by the Hall flowmeter. It was used for measuring the flow rate of particles, which is a measure of the rate that a powder will feed under gravity through a small opening. The flow rate was expressed as the time for 50 g of Al – Fe – V – Si powder to flow through the Hall flowmeter. Figure 3.18 illustrates the Hall flowmeter.

Figure 3.18 Hall flowmeter.

3.2.2 X – Ray Analysis

The phases in air atomized powders as well as in extruded alloys were identified by XRD technique. Specimens were put into XRD in both powder and bulk form. The XRD measurements were performed at METU Metallurgical and Materials Engineering Department, using Rigaku DMAX – B 2200 PC diffractometer. A

computerized Rikagu DMAX – B unit was employed for collecting 2θ values of diffraction and the intensity of the diffraction peaks. Phase identification was performed by an automated built in software of the XRD unit. The details of the parameters involved in XRD analysis are summarized in Table 3.4.

Table 3.4 The parameters of the XRD analysis.

Radiation type	Cu
λ value used	1.542 Å, K_α
X – Ray operation	40 kV, 40 mA
Temperature	22 ± 2 °C
Range of 2θ	10° – 80°
Step size	0.02°

XRD was also used for particle size determination. Particle size of the extruded samples was calculated by using Scherrer's formula. The size of very small crystals is estimated from the measured the full width of XRD peaks at the half maximum height of the peak with the use of this technique. The Scherrer's formula is as follows:

$$t = \frac{0.9 * \lambda}{B * \cos\theta_B} \tag{3.2}$$

where t is the average particle size, λ is the wavelength of the radiation used, B is the full width at half maximum intensity of the broadened diffraction line on the 2θ scale (in radians), and θ_B is the Bragg's angle of the peak selected [42].

Measuring the breath of the peak from which the broadening is to be measured is not enough because of other factors that influence the breath. These are named as instrumental broadening. In order to evaluate the degree of instrumental broadening, a standard sample is examined in the same setup. In this study, this was achieved by examining an as – cast Al – 8Fe – 1.7V – 7.9 Si alloy with a grain size larger than

10 μm. Sand casting was used to produce this standard sample and a grain size 22 μm was obtained. The broadening obtained for this sample was only due to instrumental broadening because of large grains. Structural broadening (B) is calculated as follows:

$$B^2 = B_M^2 - B_S^2 \tag{3.3}$$

where B_M is the broadening of the sample (extruded alloys) and B_S is the broadening of the standard sample (as – cast alloy).

3.2.3 DTA Analysis

The thermal stability of air atomized powders was investigated by DTA. The temperature of phase transformation of powders was measured at METU Central Laboratory by using Simultaneous Thermogravimetric Analyzer and Differential Thermal Analyzer (Setaram Labsys TGA/DTA). DTA analysis was performed from room temperature to 600 °C with a heating rate of 10 °C/min.

3.2.4 Optical Microscopy

Microstructures of extruded Al – Fe – V – Si alloy bars were examined by means of optical microscopy. The samples were prepared following standard metallographic procedures. Longitudinal and transverse sections of extruded bars were cut and mounted in Bakelite. Then, samples were grinded and polished automatically with diamond suspension with 1 μm particle size. A dilute Keller' s reagent, which is composed of 95% H_2O, 2.5% HNO_3, 1.5% HCl, and 1% HF, was used to etch polished cross sections of the samples. An Olympus PM3 optical microscope was used for taking the representative photographs of the resulting samples.

The volume percentage of the second phases was studied with the help of an image analyzer (Dewinter Material Plus 4.1).

3.2.5 SEM Analysis

The details of microstructures of powders and extruded bars, and tensile fracture surfaces were examined via SEM. Chemical analysis were also performed. A JEOL JSM 6400 Electron Microscope, equipped with an Energy Dispersive Spectrometer (EDX analyzer) was used for these purposes.

3.2.6 Tensile Tests

The extruded bars were machined in order to obtain tensile test specimens. The specimens were grinded to prevent an early failure because of any surface crack. All tensile tests were performed at four different temperatures; room temperature, 150 °C, 250 °C, and 350 °C, and according to TS138 EN10002 – 1 (Metallic materials – Tensile Testing – Part 1: Method of test at ambient temperature) and TS1730 EN 10002 – 5 (Metallic materials – Tensile Testing – Part 5: Method of test at elevated temperature) standards. The geometry and dimensions of tensile test specimens are shown in Figure 3.19.

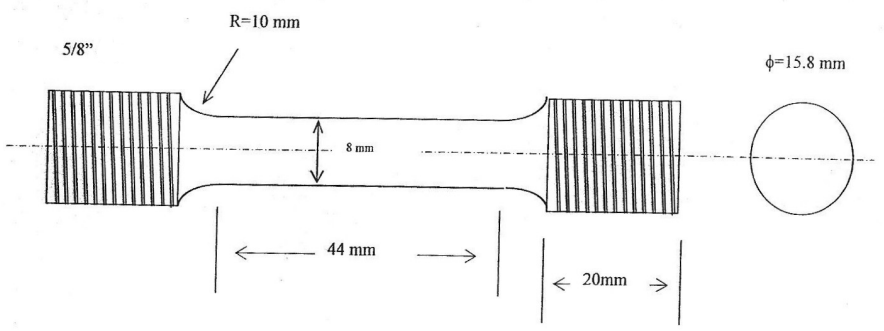

Figure 3.19 Geometry and dimensions of tensile test samples.

Tensile tests were carried out at METU Metallurgical and Materials Engineering Department; using a 50 kN machine at a strain rate of $8*10^{-4}$/s. The 0.2% proof stress, ultimate tensile strength (UTS) and elongation (%) were determined for all

specimens. To achieve a better understanding of the possible amounts of error in these tensile tests, standard deviations are also calculated and placed on the curves obtained.

3.2.7 Hardness Tests

Heckert Analogue hardness testing machine with 613 N load was used to determine the hardness. The averages of ten indentations on surfaces longitudinal and transverse to extrusion direction were taken for all specimens.

CHAPTER 4

RESULTS AND DISCUSSION

Aims of this study was to produce high temperature Al – Fe – V – Si alloy via powder processing technology and investigate the effects of powder particle size and extrusion ratio on the microstructural and mechanical properties of Al – Fe – V – Si alloy. As – atomized powder properties were taken into account because high performance Al – Fe – V – Si alloy production is strongly dependent on powder properties. Powder properties were investigated using SEM, Hall flowmeter, XRD, and DTA measurements.

After the investigation of powder properties, as – extruded Al – Fe – V – Si alloy properties were extensively studied. XRD were done in order to structurally characterize the alloys. As – extruded alloys morphology was investigated by optical microscopy and SEM. Tensile and hardness tests were used for mechanical property characterizations.

Experimental details of the samples prepared in this study were given in Table 4.1.

Table 4.1 Experimental details of the samples prepared in this study.

Al – 8Fe – 1.7V – 7.9Si Alloy Powder Size Fraction	Extrusion Ratio
212 μm < *d* < 2 mm (−2 mm+212 μm)	144:1
150 μm < *d* < 212 μm (−212+150 μm)	26:1
150 μm < *d* < 212 μm (−212+150 μm)	81:1
106 μm < *d* < 150 μm (−150+106 μm)	26:1
106 μm < *d* < 150 μm (−150+106 μm)	81:1
90 μm < *d* < 106 μm (−106+90 μm)	81:1
d < 90 μm (−90 μm)	81:1

4.1 As – Atomized Al – 8Fe – 1.7V – 7.9Si Alloy Powder Properties

The results of sieve analysis of air atomized powders of the alloy under investigation present a wide range of particle sizes. SEM micrographs exhibiting the general morphology of powder particles are presented in Figures 3.4 through 3.10. Microstructures of as – atomized powders with different size fractions were found to exhibit similar microstructural morphologies. Different cooling rates, undercoolings, and solidification velocities lead to the variation in structural morphology with powder particle size [10]. It is seen that as – atomized powder particles of different size fractions have a rounded and irregular shape.

The particle size distribution of powders < 90 μm used in the experiments is shown in Figure 4.1. The median size corresponds to the 50% value [15]. Its weight mean diameter was about 70 μm.

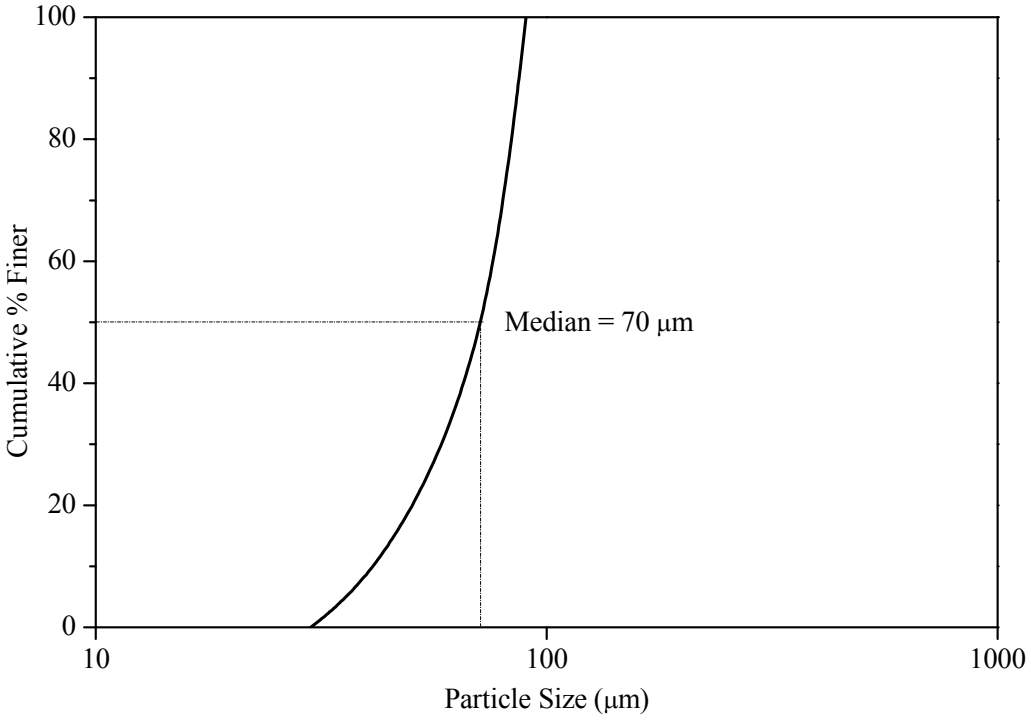

Figure 4.1 The cumulative particle size distribution plot for Al – 8Fe – 1.7V – 7.9Si alloy produced by air atomization of powder size < 90 μm.

Different size fractions of air atomized powders did not flow through the funnel and no information on their flowability could be determined as a result of Hall flowmeter tests. This type of powders is named as non – free flowing powder. Flow characteristics are dependent on several variables such as interparticle friction, particle shape and size, etc. A main feature of interparticle friction is the resistance to flow. The surface area, surface roughness and surface chemistry affect the interparticle friction [15, 19].

Details of powder characteristics are given below.

4.1.1 Phase Identifications in Atomized Powders

Powder samples were examined by XRD in order to investigate the second phase dispersoids in air – atomized alloy powders for different size fractions. XRD patterns for different size fractions are shown in Figure 4.2. The XRD pattern indicates that there are two phases, namely the aluminum matrix and $Al_{13}(Fe, V)_3Si$ phase, existing in Al – Fe – V – Si powders. In other words, powders showed the presence of α – $Al_{13}(Fe, V)_3Si$ phase of bcc structure along with α – Al. This $Al_{13}(Fe, V)_3Si$ phase (cubic silicide phase) is responsible for the high temperature strength in these alloys [8, 37, 43]. The peaks due to $Al_{13}(Fe, V)_3Si$ phase were strong so a large fraction of dispersoids occurred in these air – atomized alloy powders. Detailed XRD patterns of searched phases are given in Appendix A.

On the XRD pattern, any other second phase was not observed except for α – $Al_{13}(Fe, V)_3Si$. This situation is directly related to rapid solidification because it suppresses the formation of primary phases, brittle intermetallic silicide compounds and other eutectic mixtures that are detrimental to high temperature performance of the alloy [33, 44, 45]. With this respect, cooling rate was high enough for all size fractions of powders and no detrimental phase formation was observed.

Since the degree of undercooling increased, powder particle size decreased and supersaturation of alloying elements was raised. Supersaturation of alloying elements is directly dependent on the undercooling experienced during solidification of the alloy [46]. As seen from Figure 4.2, the peaks of $Al_{13}(Fe, V)_3Si$ phases became more evident when powder particle size increased owing to the level of undercooling.

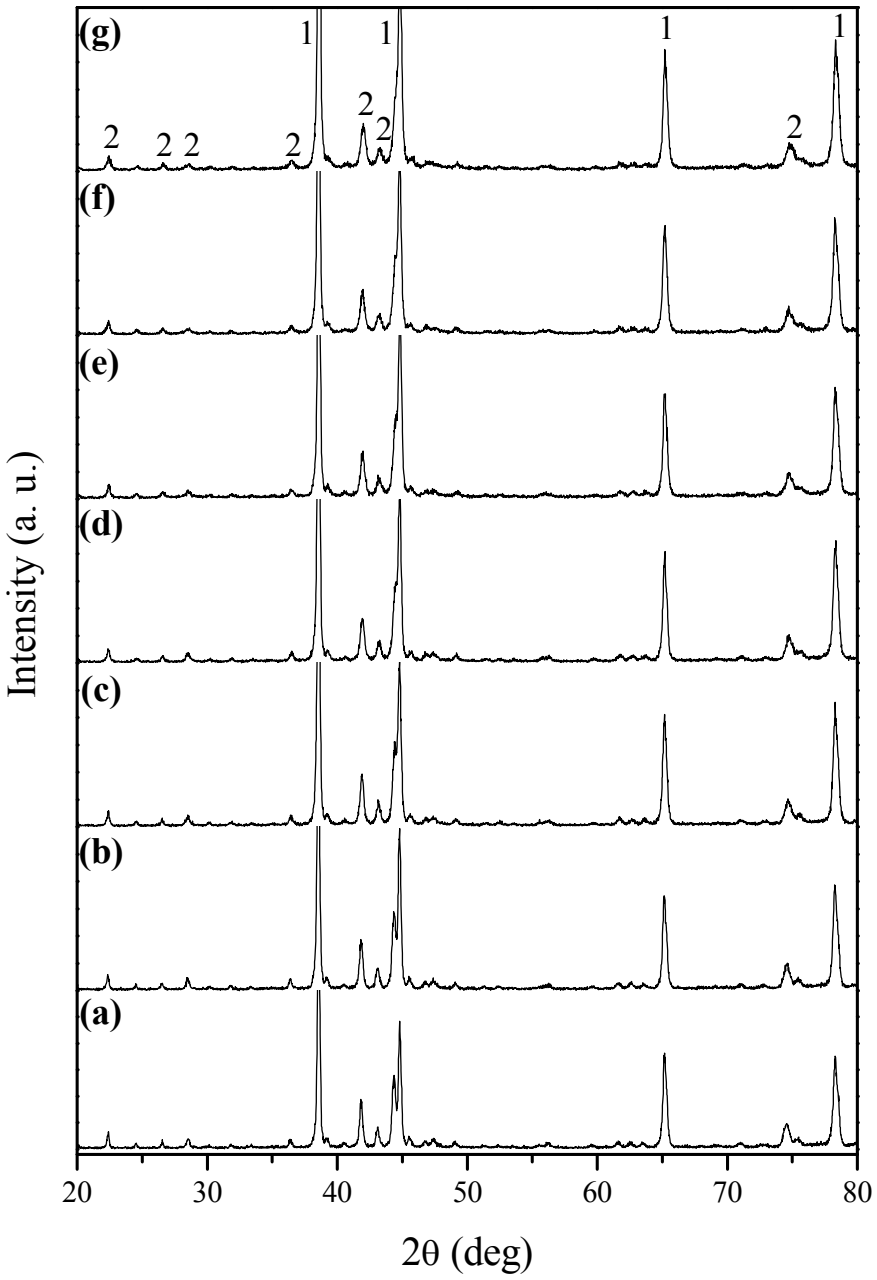

Figure 4.2 XRD pattern for Al – 8Fe – 1.7V – 7.9Si produced by air atomization of powder size fraction of **(a)** –212+150 μm, **(b)** –150+106 μm, **(c)** –106+90 μm, **(d)** –90+75 μm, **(e)** –75+53 μm, **(f)** –53+38 μm, and **(g)** –38 μm. [**(1)** Aluminum, **(2)** $Al_{13}(Fe, V)_3Si$ phase.]

4.1.2 Microstructural Stability of Atomized Powders

Microstructural stability of air – atomized powders was investigated by DTA scanning in the temperature range 25 to 600 °C and with a heating rate of 10 °C/min. Figure 4.3 shows DTA traces for Al – 8Fe – 1.V – 7.9Si alloy powder of different size fractions. There is a strong exotherm with a peak temperature at 581 °C, which is indicative of a phase transformation occurring during heating of the powders, on the DTA traces of all alloy powders of different size fractions. In addition, the strong DTA peak implies that a large fraction of the microstructure in all powders was composed of this phase. The possible phase transformation reaction corresponding to DTA exotherm may be the decomposition of $\alpha - Al_{13}(Fe, V)_3Si$ phase. The decomposition temperature at which the $\alpha - Al_{13}(Fe, V)_3Si$ phase transformed to the $\theta - (Al, Si)_3Fe_4$ phase was found to be 650 °C for a melt spun Al – 13.4Fe – 0.85V – 2.23Si alloy [4]. Wang et al. [4] prove this phase transformation with the help of TEM and XRD. The difference between this temperature (650 °C) and measured DTA peak temperature (581 °C) was entirely attributed to the amount of silicon, which was 7.9 wt% of Si in this study because the transformation temperature is reduced as the amount of silicon increases in the quaternary alloys [37]. In addition, Aral [47] studied the effect of temperature expose on phase stability of Al – 8.5Fe – 1.7V – 1.3Si alloy powders. According to XRD analysis, no new phase formation was observed at 650 °C exposure for 10 hours [47].

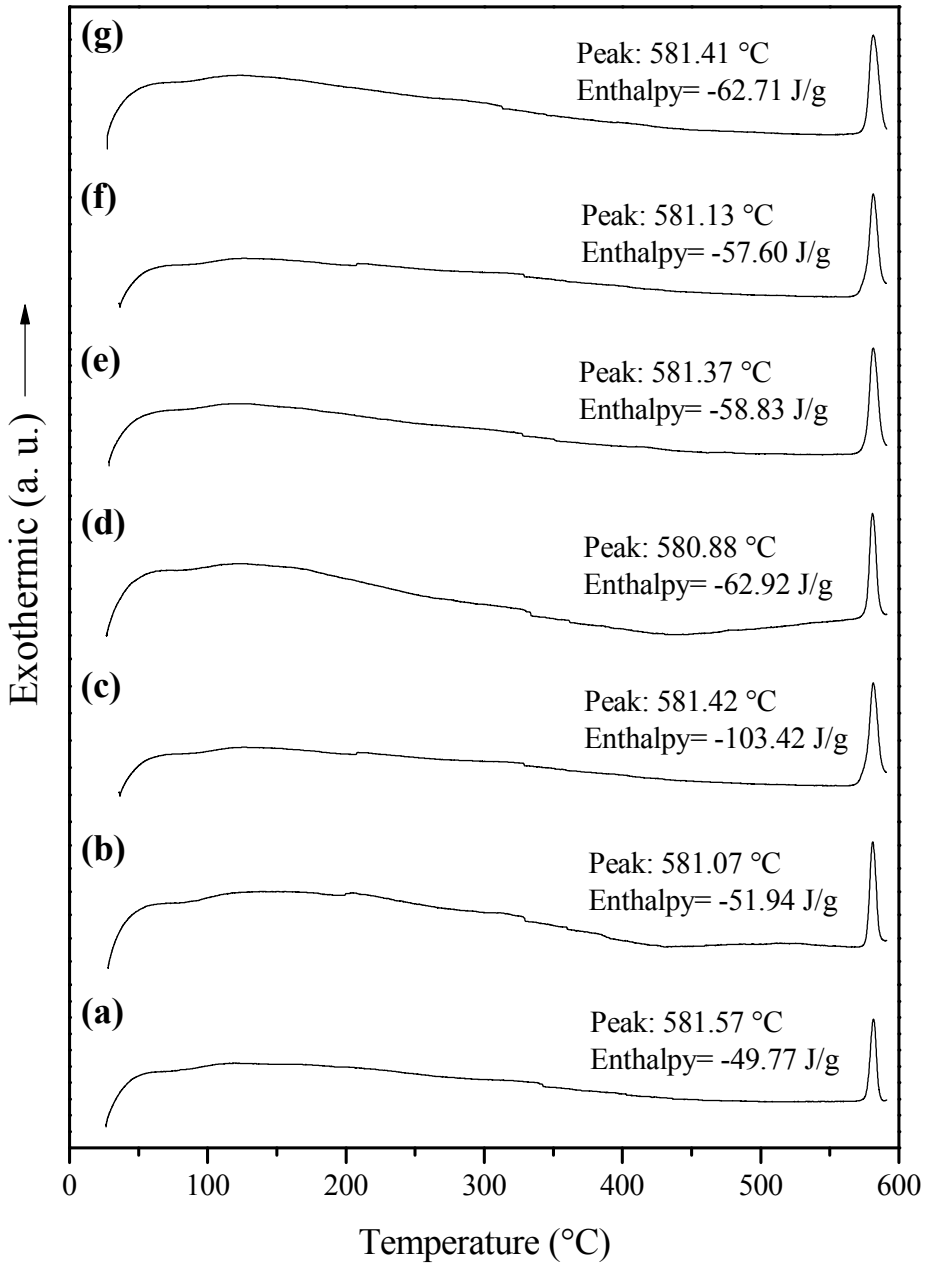

Figure 4.3 DTA traces for Al – 8Fe – 1.V – 7.9Si alloy powder of different size fractions processed by air atomization. **(a)** –212+150 μm, **(b)** –150+106 μm, **(c)** –106+90 μm, **(d)** –90+75 μm, **(e)** –75+53 μm, **(f)** –53+38 μm, and **(g)** –38 μm.

4.2 Extruded Al – 8Fe – 1.7V – 7.9Si Alloy Properties

For the production of high performance Al – Fe – V− Si alloy, there were a lot of steps which affect the high temperature properties of the alloy. Hot extrusion was important because it preserves the ultra fine microstructure of initial powders, eliminates defects and improves relative density. During hot extrusion, the alloys were exposed to a short time of high temperature and large deformation. Therefore, the fragmentation of large – sized phases into smaller – sized particles, sealing the micropores and formation of fine microstructures are the results of hot extrusion [33, 41].

4.2.1 Phase Identifications in Extruded Alloys

XRD analysis was done for characterization of the second phase dispersoids in extruded alloys whether or not hot extrusion affects the present phases in the alloy. Figure 4.4 shows the XRD patterns of extruded samples prepared by different powder particle size fraction and extrusion ratio. The phases of the extruded alloys were α – $Al_{13}(Fe, V)_3Si$ and α – Al. Detailed XRD patterns of searched phases are given in Appendix A.

As seen from Figure 4.4, new phase formation was not seen in the XRD pattern after hot extrusion except for the intensities of α – $Al_{13}(Fe, V)_3Si$ phases which increased after hot extrusion for all extruded alloy samples. In addition, the peaks of α – $Al_{13}(Fe, V)_3Si$ phase became more evident as powder particle size fraction decreased owing to the level of undercooling. In the case of extruded alloy produced from finer powders where supersaturation levels were high, α – $Al_{13}(Fe, V)_3Si$ phase precipitated out from supersaturated matrix after hot extrusion [46, 47]. On the other hand, variation in extrusion ratio did not affect the presence of α – $Al_{13}(Fe, V)_3Si$ phase.

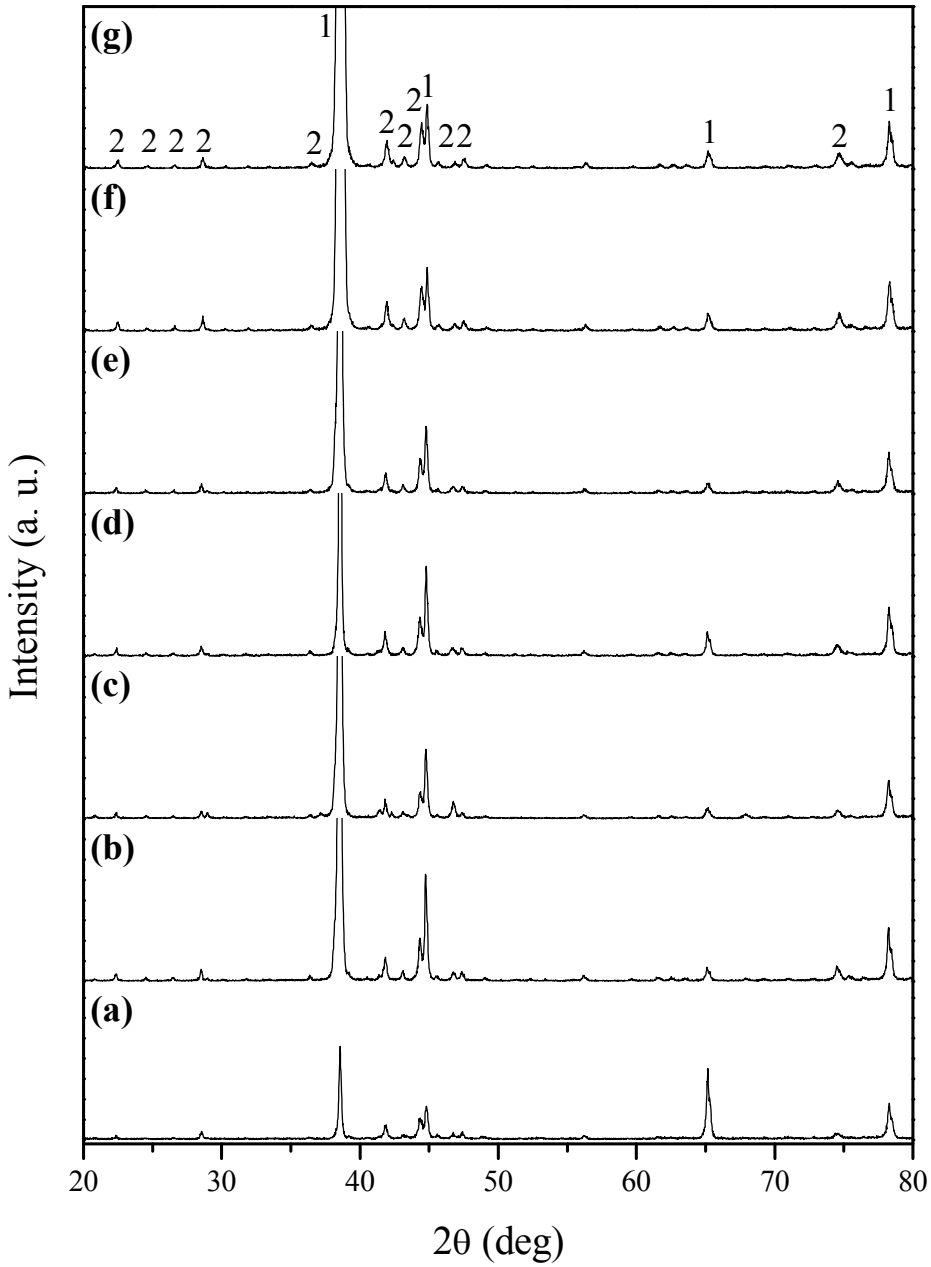

Figure 4.4 XRD pattern for extruded Al – 8Fe – 1.7V – 7.9Si alloys of powder size fraction of **(a)** –2000+212 μm (144:1), **(b)** –212+150 μm (26:1), **(c)** –212+150 μm (81:1), **(d)** –150+106 μm (26:1), **(e)** –150+106 μm (81:1), **(f)** –106+90 μm (81:1), and **(g)** –90 μm (81:1). [**(1)** Aluminum, **(2)** $Al_{13}(Fe, V)_3Si$ phase.]

4.2.2 Particle Size (Crystallite Size) Determination in Extruded Alloys

Grain size or the particle size of the structure affects the mechanical properties of the materials. XRD was used to determine the particle size of the extruded alloys in this study. For particle size determination, aluminum (220) peak was used. Particle sizes of extruded alloys that were calculated using equation 3.2 are shown in Table 4.2.

Table 4.2 Approximate particle sizes of extruded alloys obtained from different powder particle size fraction and extrusion ratio.

Powder Size Fraction (Extrusion Ratio)	***B*** **(radians)**	θ_B **(°)**	**Approximate Particle Size (nm)**
−2000+212 μm (144:1)	1.905×10^{-3}	32.63	205.64
−212+150 μm (26:1)	3.405×10^{-3}	32.62	113.56
−212+150 μm (81:1)	3.405×10^{-3}	32.61	110.69
−150+106 μm (26:1)	3.991×10^{-3}	32.63	98.17
−150+106 μm (81:1)	3.991×10^{-3}	32.59	89.91
−106+90 μm (81:1)	4.527×10^{-3}	32.58	77.42
−90 μm (81:1)	5.030×10^{-3}	32.59	71.34

These results show that the finer powders and higher extrusion ratios that the alloys were produced from, the smaller particle sizes.

4.2.3 Microstructural Features of Extruded Alloys

In order to reveal the overall microstructural features of the extruded alloys and the distribution of $Al_{13}(Fe, V)_3Si$ phase, optical microscope analysis were done. Both longitudinal and transverse sections of the rods were investigated. The optical micrographs of extruded alloys are given in Figures 4.5 through 4.18.

The optical microscopy study revealed that the microstructure of the extruded alloys is very fine. It was impossible to observe the grain boundaries in optical microscope. The microstructures of the extruded alloys consisted of $Al_{13}(Fe, V)_3Si$ phase embedded in fine grained Al matrix. During hot extrusion, $Al_{13}(Fe, V)_3Si$ particles in as – atomized powders are fragmented into smaller size particles and realign around the fine grained matrix boundaries [48]. Uniform distribution of fragmented $Al_{13}(Fe, V)_3Si$ particles could not be achieved during hot extrusion because of highly plastic matrix [33] so as seen from figures, the microstructures of the extruded alloys were not homogeneous. The microstructures of the extruded alloys comprised of regions containing fine and coarse dispersoids. These regions can be seen in both optical micrographs. In these micrographs, bright regions consisted of fine dispersoids whereas dark ones were composed of coarser dispersoids.

Figures 4.5 through 4.11 clearly show that as powder particle size decreased, dispersoids became finer and more uniform microstructures of extruded alloys were obtained. Moreover, the extrusion ratio had an important effect on the microstructure. The amount of fragmented particles dispersed in the matrix increased with the help of higher extrusion ratios. As a result of this, the microstructures became more uniform. Figure 4.6 – 4.7 and Figure 4.8 – 4.9 demonstrates the effect of extrusion ratio on the microstructure.

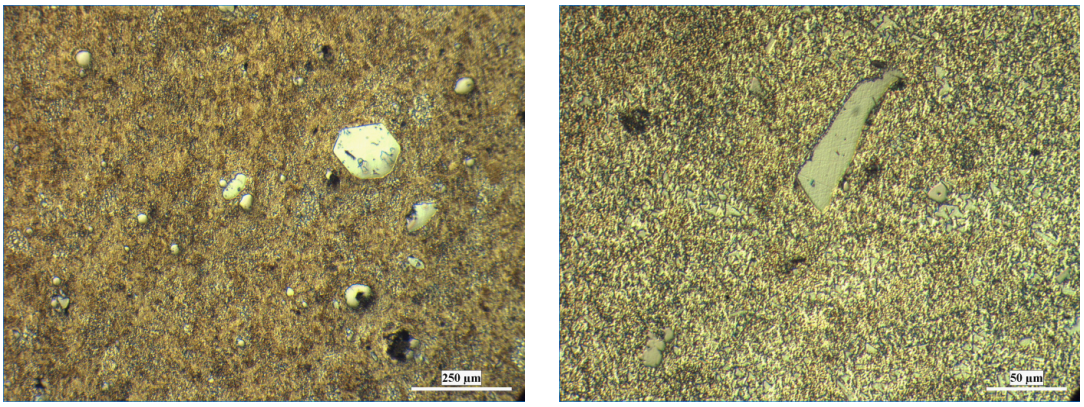

(a) **(b)**

Figure 4.5 Optical micrographs showing the microstructures of transverse section of Al – 8Fe – 1.7V – 7.9Si alloy produced by hot extrusion of –2000+212 µm powders with an extrusion ratio of 144:1 at **(a)** 50X **(b)** 200X.

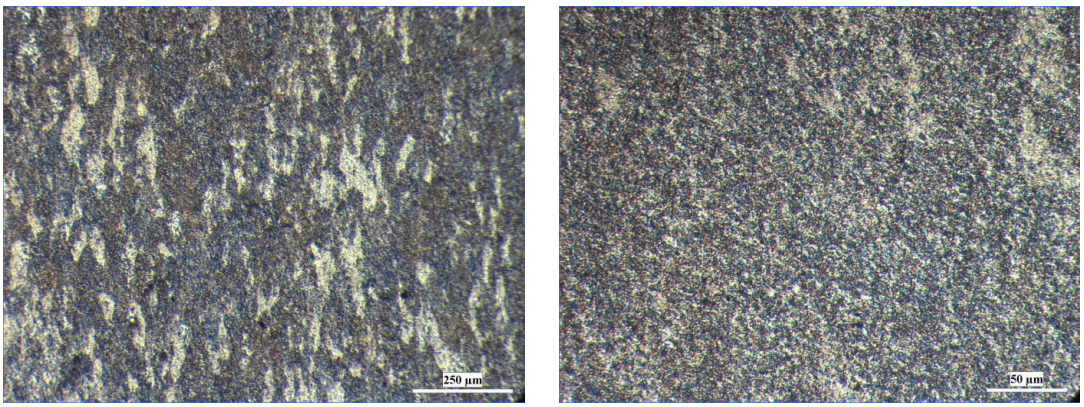

(a) **(b)**

Figure 4.6 Optical micrographs showing the microstructures of transverse section of Al – 8Fe – 1.7V – 7.9Si alloy produced by hot extrusion of –212+150 µm powders with an extrusion ratio of 26:1 at **(a)** 50X **(b)** 200X.

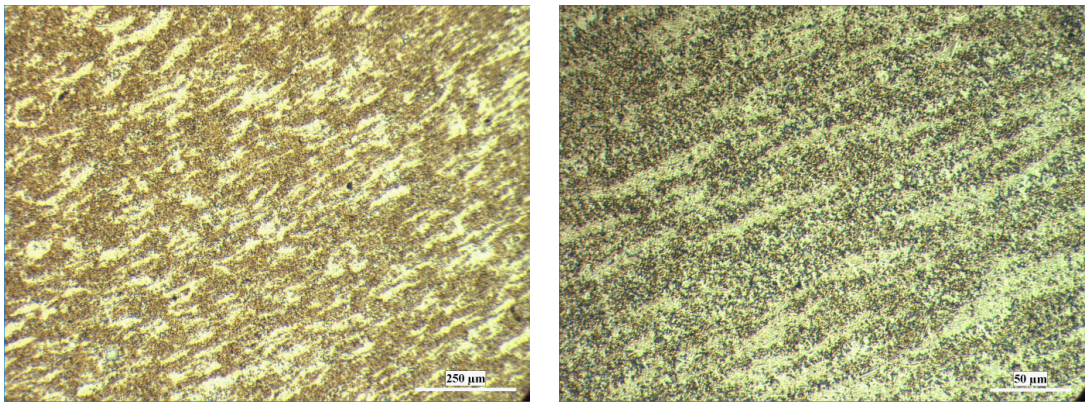

(a) **(b)**

Figure 4.7 Optical micrographs showing the microstructures of transverse section of Al – 8Fe – 1.7V – 7.9Si alloy produced by hot extrusion of –212+150 µm powders with an extrusion ratio of 81:1 at **(a)** 50X **(b)** 200X.

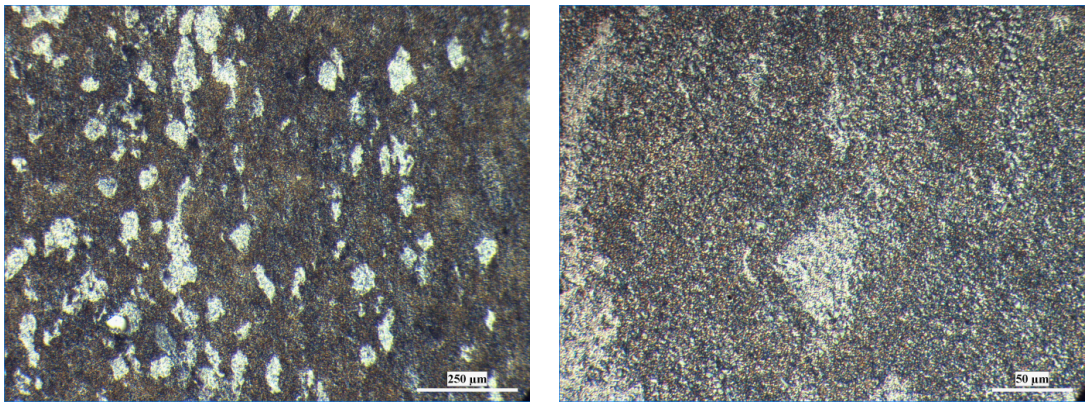

(a) **(b)**

Figure 4.8 Optical micrographs showing the microstructures of transverse section of Al – 8Fe – 1.7V – 7.9Si alloy produced by hot extrusion of –150+106 µm powders with an extrusion ratio of 26:1 at **(a)** 50X **(b)** 200X.

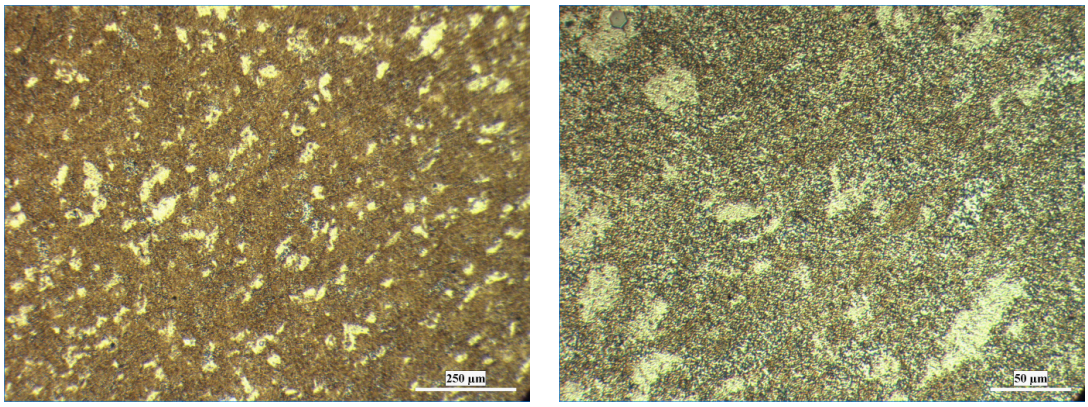

(a) **(b)**

Figure 4.9 Optical micrographs showing the microstructures of transverse section of Al – 8Fe – 1.7V – 7.9Si alloy produced by hot extrusion of –150+106 µm powders with an extrusion ratio of 81:1 at **(a)** 50X **(b)** 200X.

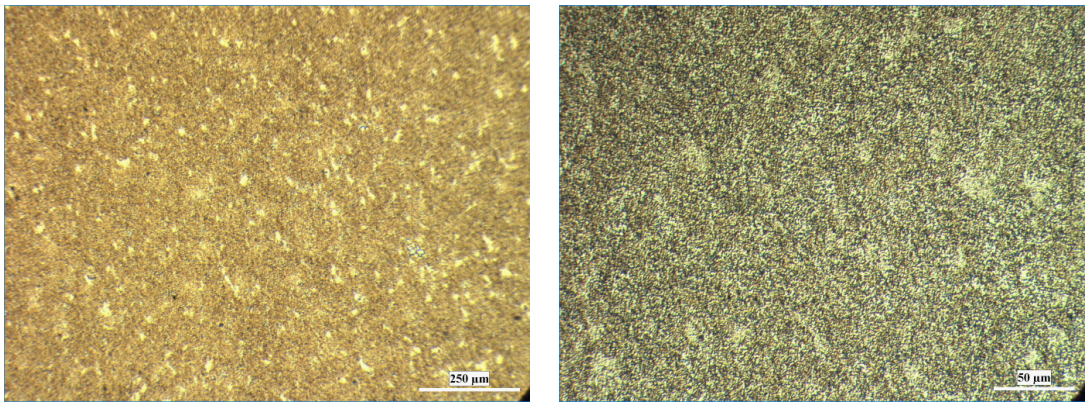

(a) **(b)**

Figure 4.10 Optical micrographs showing the microstructures of transverse section of Al – 8Fe – 1.7V – 7.9Si alloy produced by hot extrusion of –106+90 µm powders with an extrusion ratio of 81:1 at **(a)** 50X **(b)** 200X.

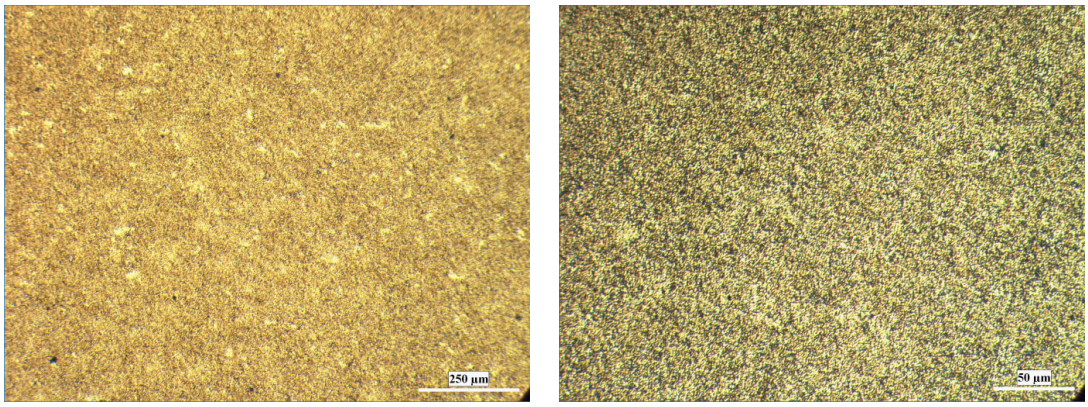

(a) **(b)**

Figure 4.11 Optical micrographs showing the microstructures of transverse section of Al – 8Fe – 1.7V – 7.9Si alloy produced by hot extrusion of –90 µm powders with an extrusion ratio of 81:1 at **(a)** 50X **(b)** 200X.

The longitudinal sections of the extruded alloys are shown in Figures 4.12 through 4.18. The microstructures of extruded bars were inhomogeneous and a noticeable lamellar structure existed along the longitudinal sections of the extrudates. This structure was fine. Furthermore, there were bands of regions containing fine and coarse dispersoids that were elongated with an alternate dark and bright contrast in the material flow direction.

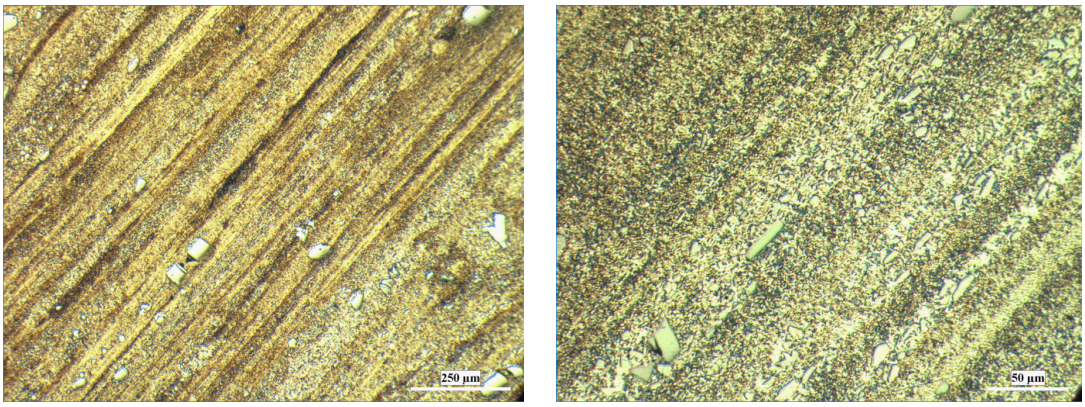

(a) **(b)**

Figure 4.12 Optical micrographs showing the microstructures of longitudinal section of Al – 8Fe – 1.7V – 7.9Si alloy produced by hot extrusion of –2000+212 µm powders with an extrusion ratio of 144:1 at **(a)** 50X **(b)** 200X.

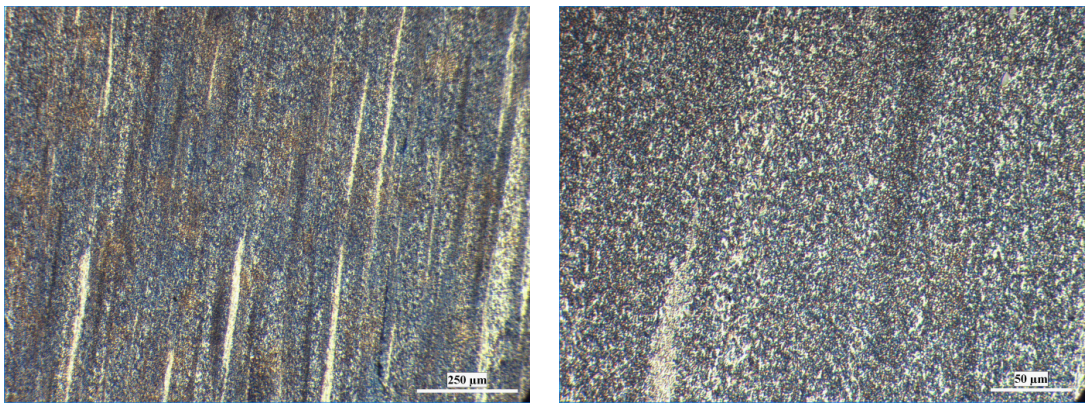

(a) **(b)**

Figure 4.13 Optical micrographs showing the microstructures of longitudinal section of Al – 8Fe – 1.7V – 7.9Si alloy produced by hot extrusion of –212+ 50 µm powders with an extrusion ratio of 26:1 at **(a)** 50X **(b)** 200X.

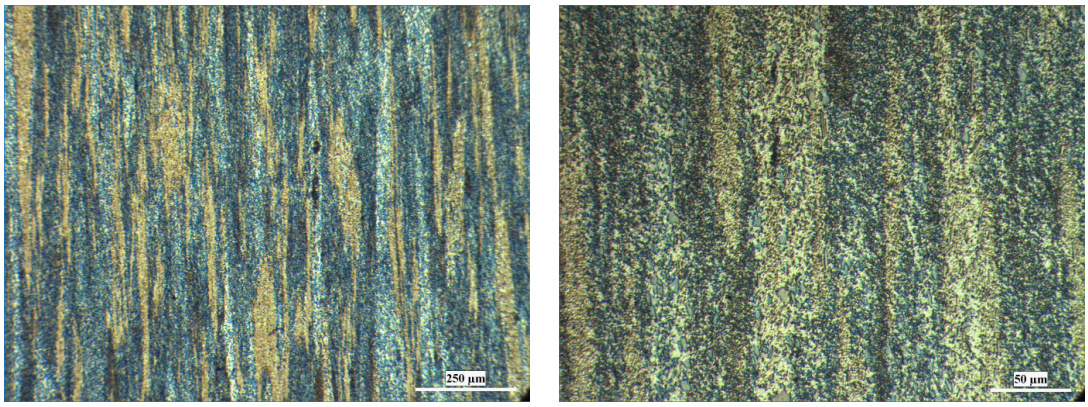

(a) **(b)**

Figure 4.14 Optical micrographs showing the microstructures of longitudinal section of Al – 8Fe – 1.7V – 7.9Si alloy produced by hot extrusion of –212+150 µm powders with an extrusion ratio of 81:1 **(a)** 50X **(b)** 200X.

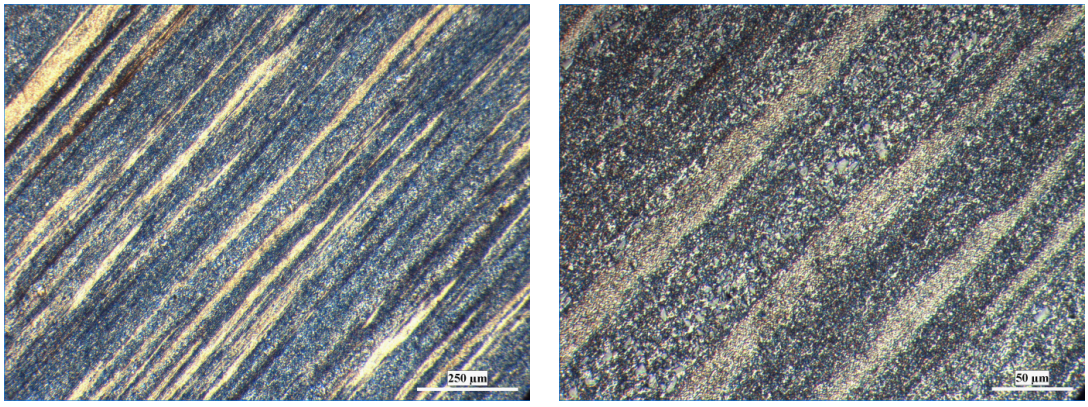

(a) **(b)**

Figure 4.15 Optical micrographs showing the microstructures of longitudinal section of Al – 8Fe – 1.7V – 7.9Si alloy produced by hot extrusion of –150+106 µm powders with an extrusion ratio of 26:1 at **(a)** 50X **(b)** 200X.

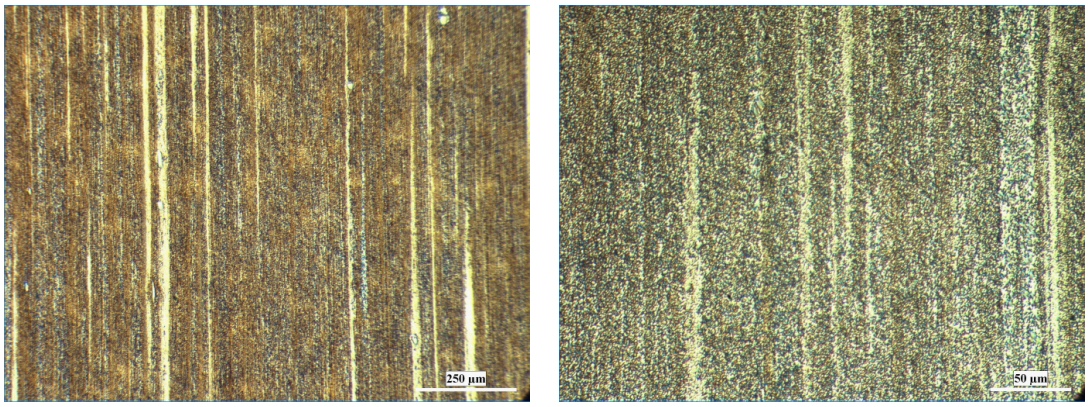

(a) **(b)**

Figure 4.16 Optical micrographs showing the microstructures of longitudinal section of Al – 8Fe – 1.7V – 7.9Si alloy produced by hot extrusion of –150+106 µm powders with an extrusion ratio of 81:1 at **(a)** 50X **(b)** 200X.

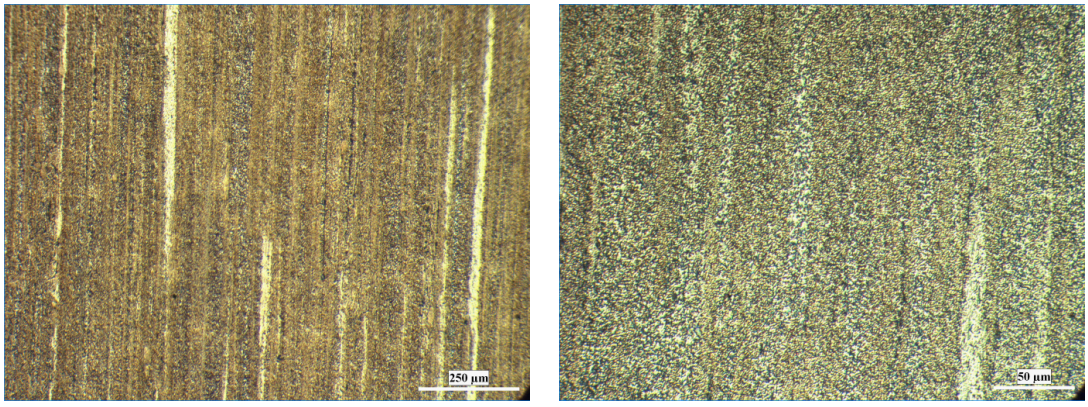

(a) **(b)**

Figure 4.17 Optical micrographs showing the microstructures of longitudinal section of Al – 8Fe – 1.7V – 7.9Si alloy produced by hot extrusion of –106+90 µm powders with an extrusion ratio of 81:1 at **(a)** 50X **(b)** 200X.

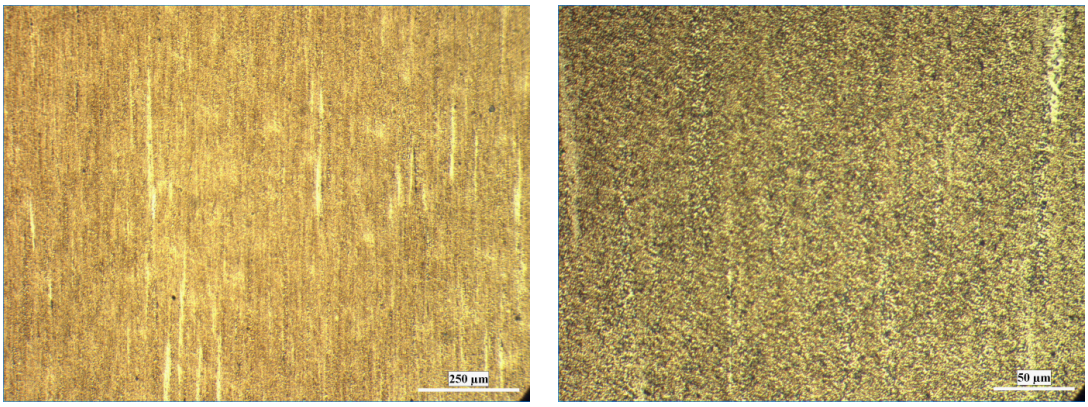

(a) **(b)**

Figure 4.18 Optical micrographs showing the microstructures of longitudinal section of Al – 8Fe – 1.7V – 7.9Si alloy produced by hot extrusion of –90 µm powders with an extrusion ratio of 81:1 at **(a)** 50X **(b)** 200X.

As seen from the optical micrographs, the distribution of dispersoids was more uniform for finer powder size fractions and higher extrusion ratio. The dispersoids' size decreased with decreasing powder particle size. This decrease in dispersoid size was due to higher cooling rate of finer powders.

Extruded alloys were examined by Dewinter Material Plus 4.1 to investigate the vol% of dispersoids in the matrix. This program makes a contrast between two phases and finds the area ratio of these phases. Extruded alloys were investigated from the surfaces longitudinal to extrusion direction at 100X magnification because the resolution was not enough to reveal the actual contrast between the phases at the surfaces transverse to extrusion direction. An example of the image analysis is given in Figure 4.19.

Vol%' s calculated by Dewinter Material Plus 4.1 are listed in Table 4.3. It is seen that vol% of dispersoids in the matrix increased with decreasing powder particle size and increasing extrusion ratio.

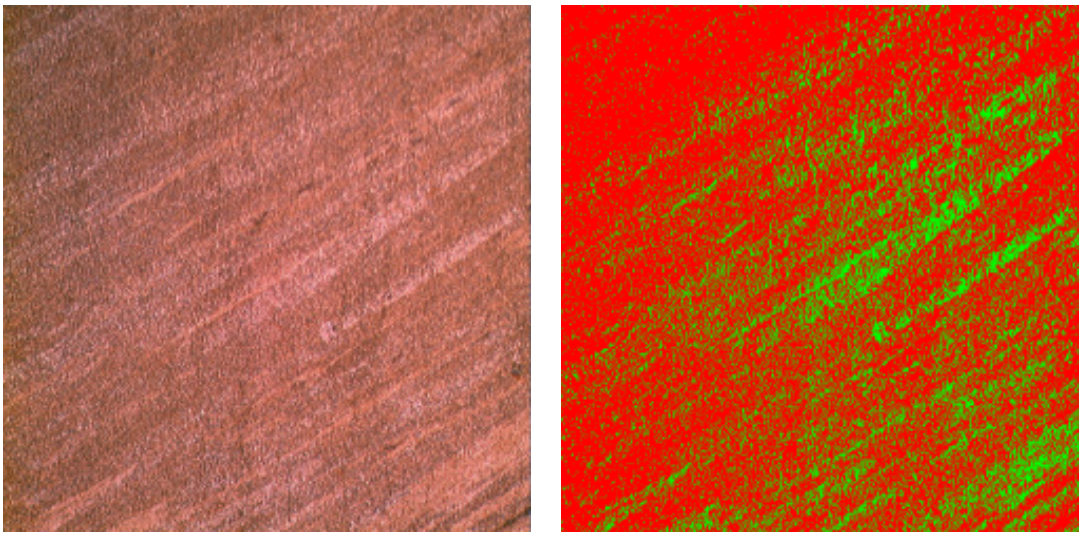

(a) **(b)**

Figure 4.19 **(a)** The optical micrograph showing the microstructure of longitudinal section of the extruded alloy produced by hot extrusion of −212+150 µm powders with an extrusion ratio of 26:1 at 100X **(b)** The image after image analysis.

Table 4.3 Image analyzer results of the extruded alloys.

Powder Size Fraction (Extrusion Ratio)	**Vol% of Dispersoids**
−2000+212 µm (144:1)	22.8
−212+150 µm (26:1)	24.3
−212+150 µm (81:1)	26.0
−150+106 µm (26:1)	27.9
−150+106 µm (81:1)	29.2
−106+90 µm (81:1)	33.7
−90 µm (81:1)	35.5

The longitudinal and transverse sections of extruded alloys were examined by means of SEM in order to observe the detailed microstructure in spite of the fact that SEM does not have sufficient resolution to show the microstructure. The longitudinal sections are given in Figures 4.20 through 4.26 while Figures 4.27 through 4.33 demonstrate the transverse sections of the extruded alloys.

As it can be observed in SEM micrographs, the microstructure of the extruded alloys consisted of very fine grain size and irregular shaped intermetallic dispersoids ($Al_{13}(Fe, V)_3Si$) distributed throughout the aluminum matrix. Because of the fineness of the grains, grain boundaries could not be seen in the SEM micrographs.

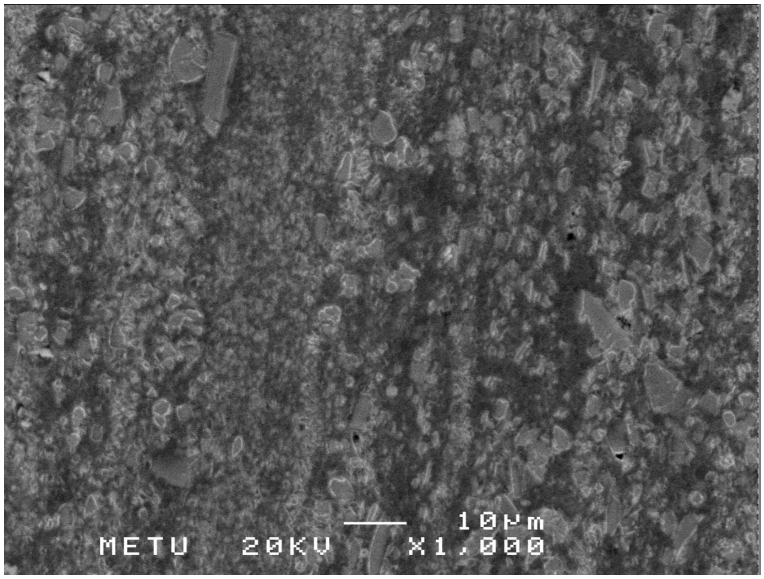

Figure 4.20 SEM micrograph showing the microstructures of longitudinal section of Al – 8Fe – 1.7V – 7.9Si alloy produced by hot extrusion of –2000+212 μm powders with an extrusion ratio of 144:1.

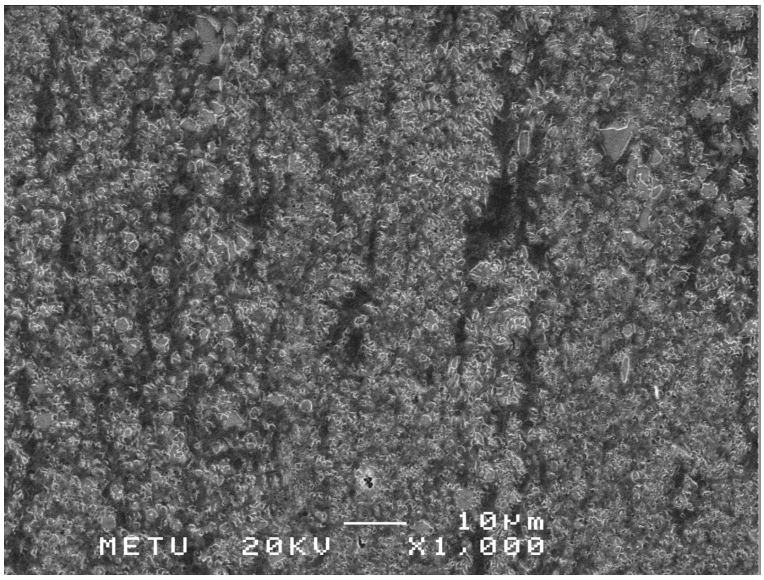

Figure 4.21 SEM micrograph showing the microstructures of longitudinal section of Al – 8Fe – 1.7V – 7.9Si alloy produced by hot extrusion of –212+150 µm powders with an extrusion ratio of 26:1.

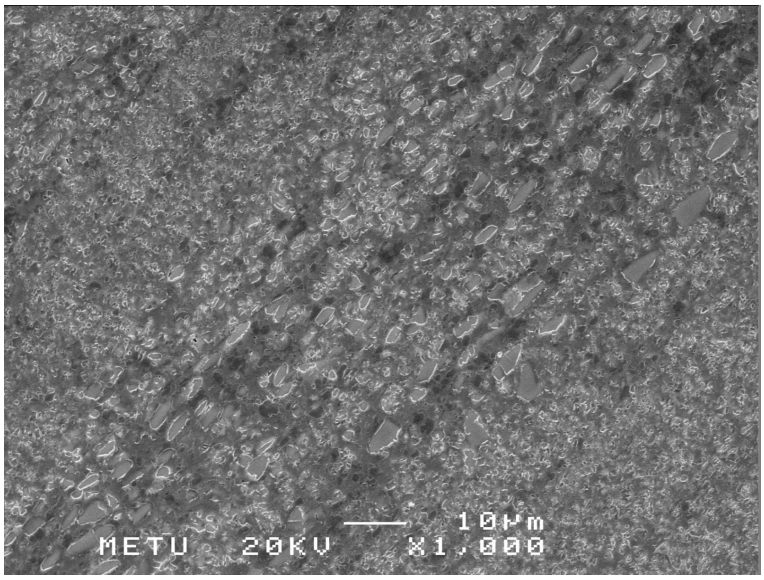

Figure 4.22 SEM micrograph showing the microstructures of longitudinal section of Al – 8Fe – 1.7V – 7.9Si alloy produced by hot extrusion of –212+150 µm powders with an extrusion ratio of 81:1.

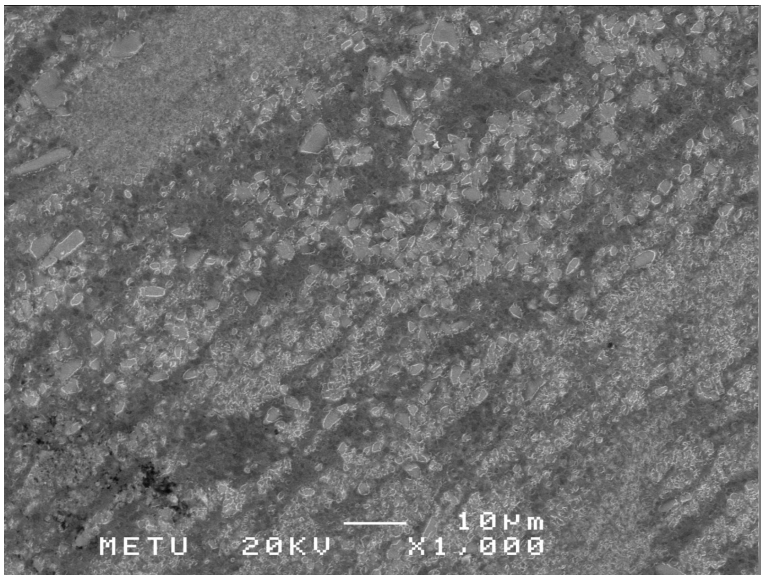

Figure 4.23 SEM micrograph showing the microstructures of longitudinal section of Al – 8Fe – 1.7V – 7.9Si alloy produced by hot extrusion of –150+106 µm powders with an extrusion ratio of 26:1.

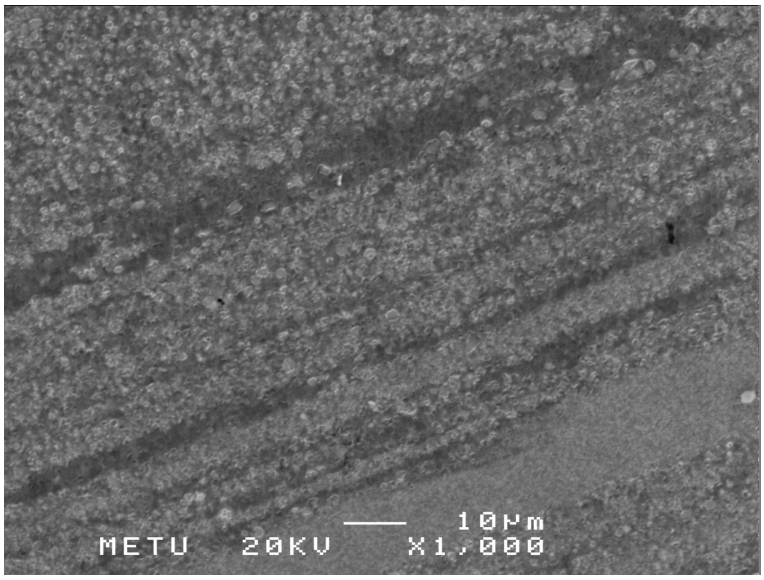

Figure 4.24 SEM micrograph showing the microstructures of longitudinal section of Al – 8Fe – 1.7V – 7.9Si alloy produced by hot extrusion of –150+106 µm powders with an extrusion ratio of 81:1.

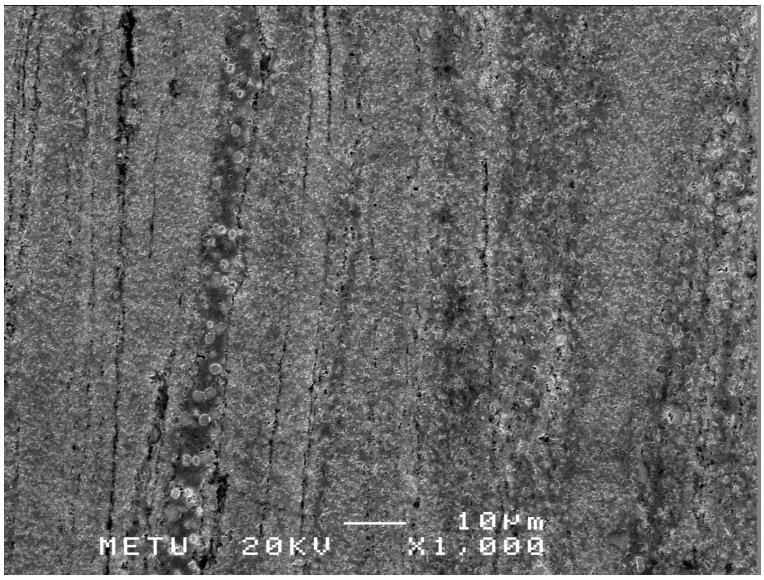

Figure 4.25 SEM micrograph showing the microstructures of longitudinal section of Al – 8Fe – 1.7V – 7.9Si alloy produced by hot extrusion of –106+90 µm powders with an extrusion ratio of 81:1.

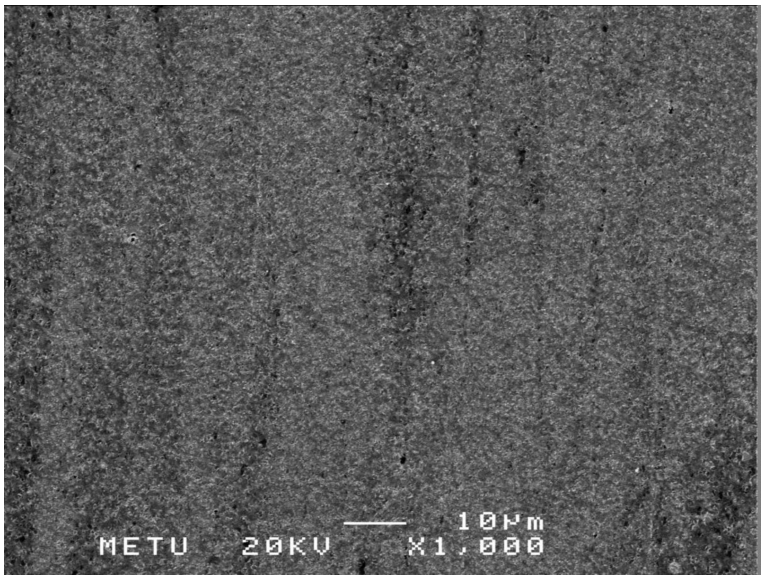

Figure 4.26 SEM micrograph showing the microstructures of longitudinal section of Al – 8Fe – 1.7V – 7.9Si alloy produced by hot extrusion of –90 µm powders with an extrusion ratio of 81:1.

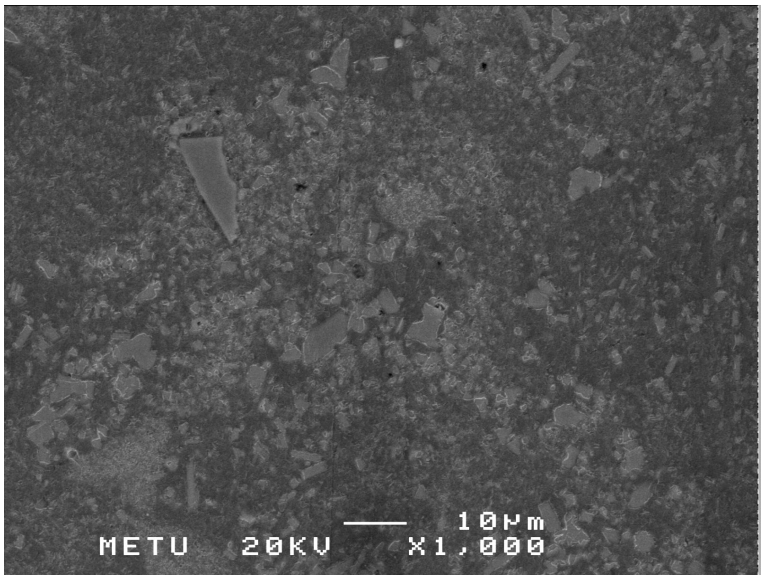

Figure 4.27 SEM micrograph showing the microstructures of transverse section of Al – 8Fe – 1.7V – 7.9Si alloy produced by hot extrusion of –2000+212 µm powders with an extrusion ratio of 144:1.

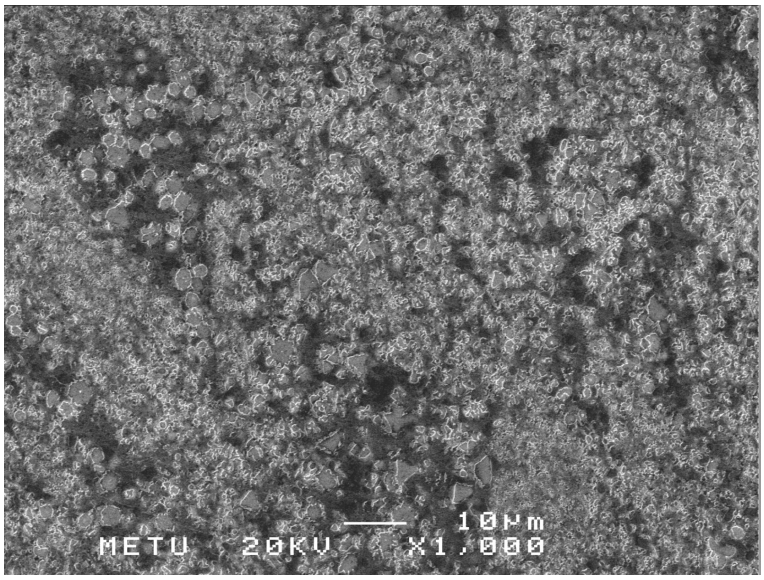

Figure 4.28 SEM micrograph showing the microstructures of transverse section of Al – 8Fe – 1.7V – 7.9Si alloy produced by hot extrusion of –212+150 µm powders with an extrusion ratio of 26:1.

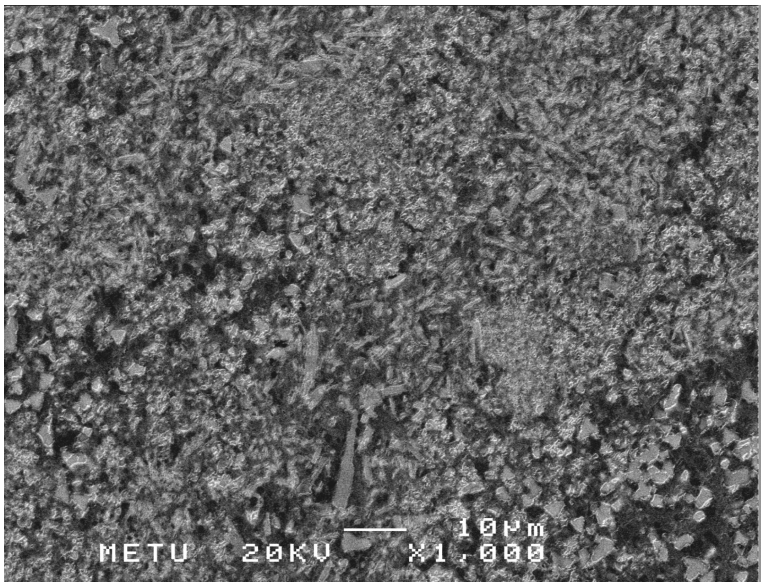

Figure 4.29 SEM micrograph showing the microstructures of transverse section of Al – 8Fe – 1.7V – 7.9Si alloy produced by hot extrusion of –212+150 µm powders with an extrusion ratio of 81:1.

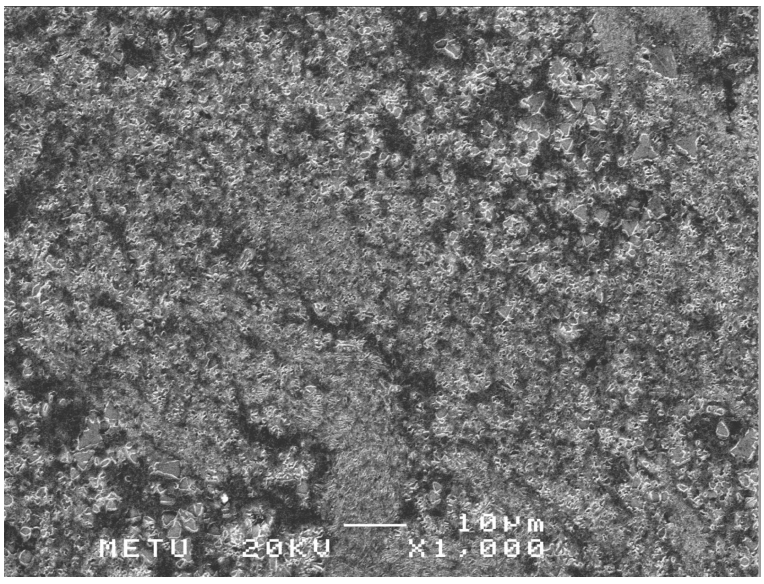

Figure 4.30 SEM micrograph showing the microstructures of transverse section of Al – 8Fe – 1.7V – 7.9Si alloy produced by hot extrusion of –150+106 µm powders with an extrusion ratio of 26:1.

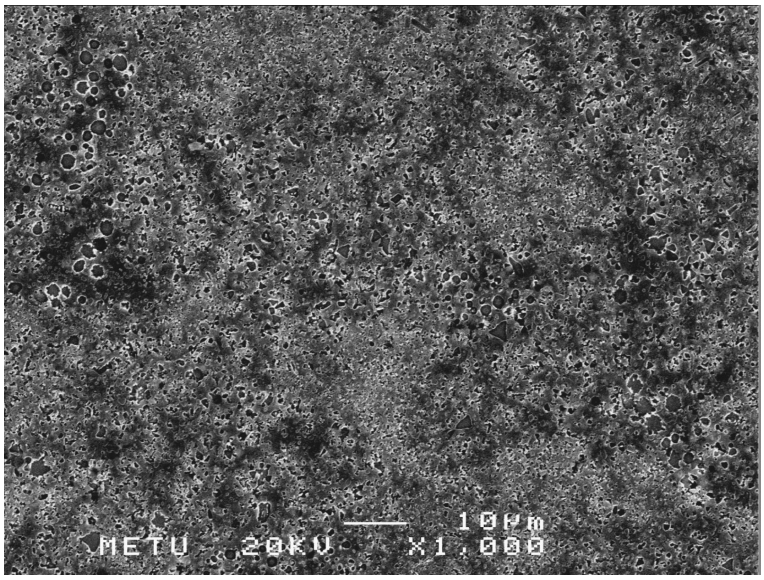

Figure 4.31 SEM micrograph showing the microstructures of transverse section of Al – 8Fe – 1.7V – 7.9Si alloy produced by hot extrusion of –150+106 µm powders with an extrusion ratio of 81:1.

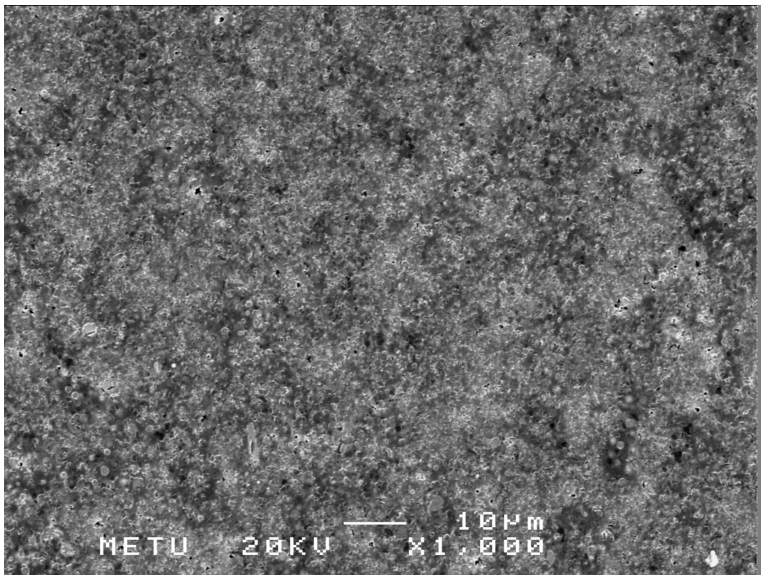

Figure 4.32 SEM micrograph showing the microstructures of transverse section of Al – 8Fe – 1.7V – 7.9Si alloy produced by hot extrusion of –106+90 µm powders with an extrusion ratio of 81:1.

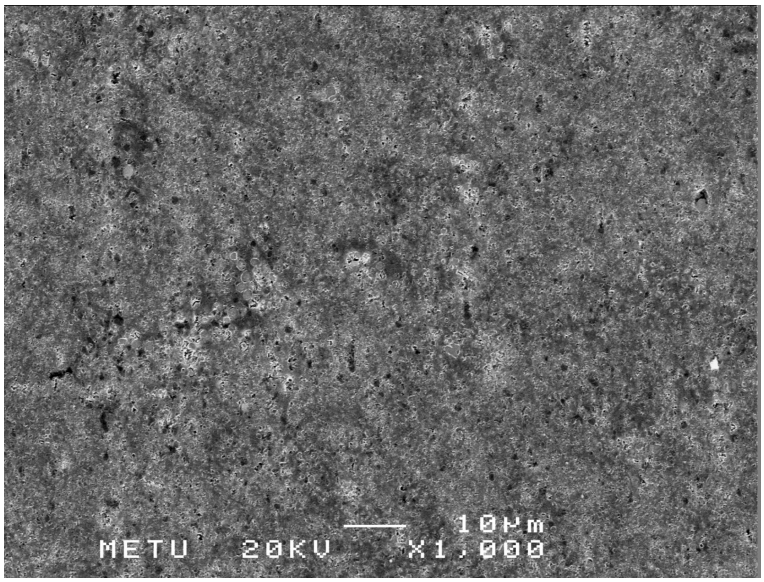

Figure 4.33 SEM micrograph showing the microstructures of transverse section of Al – 8Fe – 1.7V – 7.9Si alloy produced by hot extrusion of –90 µm powders with an extrusion ratio of 81:1.

It is clear from SEM micrographs that the change of powder particle size from coarse to fine and increase in extrusion ratio is beneficial to the forming small dispersoids, more uniform and finer microstructure.

EDX analysis also conducted mainly on the transverse sections to obtain information about the chemical composition of dispersoids. Table 4.4 shows the EDX results of dispersoids in the extruded alloys.

Table 4.4 EDX results of dispersoids in the extruded alloys.

Figure	Element (at. %)			
	Al	**Fe**	**V**	**Si**
4.27	72.10	13.27	3.97	10.66
4.28	85.51	6.31	1.06	7.12
4.29	72.60	14.16	0.21	13.02
4.30	77.01	10.92	2.82	9.25
4.31	86.63	8.98	0.56	3.83
4.32	88.63	6.58	0.88	3.91
4.33	78.86	9.98	1.82	9.34

The stoichiometric formulas of dispersoids in extruded alloys produced from –2000+212 μm powders with an extrusion ratio of 144:1, –212+150 μm powders with an extrusion ratio of 26:1, –212+150 μm powders with an extrusion ratio of 81:1, –150+106 μm powders with an extrusion ratio of 26:1, –150+106 μm powders with an extrusion ratio of 81:1, –106+90 μm powders with an extrusion ratio of 81:1, and –90 μm powders with an extrusion ratio of 81:1 corresponded to $Al_{6.8}(Fe, V)_{1.6}Si$, $Al_{12}(Fe, V)_{1.1}Si$, $Al_{5.6}(Fe, V)_{1.1}Si$, $Al_{8.3}(Fe, V)_{1.5}Si$, $Al_{22.6}(Fe, V)_{2.5}Si$, $Al_{22.7}(Fe, V)_{1.9}Si$, and $Al_{8.4}(Fe, V)1._3Si$, respectively. It is evident from EDX results that the extruded alloys contained only quaternary dispersoids and these dispersoids were silicides. However, the composition of the silicides was not confirmed by XRD since the points on dispersoids are analyzed by means of EDX and as a result of this, EDX cannot give the accurate composition.

4.2.4 Mechanical Properties of Extruded Alloys

Mechanical analysis included the investigation of tensile properties, fractography, and hardness of extruded alloys. Two types of mechanical tests, which were tensile and hardness tests, were carried out for seven different types of specimens. For each condition, arithmetic means and standard deviations were calculated.

4.2.4.1 Tensile Test Analysis of Extruded Alloys

Tensile tests were performed with the aim of studying the high temperature tensile properties of the extruded samples and the effect of powder particle size and extrusion ratio on the high temperature performance. Several tensile tests were done and their results are given in Appendix B.

The tensile properties of the extruded alloys produced using the hot extrusion of the air atomized powders at room temperature and high temperatures (150, 250, and 350 °C) are summarized in Tables 4.5 through 4.8. As seen from these tables, at room and elevated temperatures, the alloy made from –90 μm powders with an extrusion ratio of 81:1 showed the best tensile properties among all seven different hot extruded alloys. These property enhancements were attributed to fine and dispersed intermetallic compound ($Al_{13}(Fe, V)_3Si$) produced by rapid solidification process. Finer powder sizes were subjected to higher cooling rate so they had finer dispersoids than coarser ones. Other than the powder particle size effect, the increase in extrusion ratio provides the uniform distribution of dispersoids [33]. The principal strengthening mechanism in these alloys is the dislocation pinning by dispersoids [3, 8, 49]. Also, the retention of high levels of strength to high temperatures is caused by the relative resistance of these dispersoids to Ostwald ripening and grain growth and recrystallization [8, 50].

Table 4.5 Mechanical properties of Al – 8Fe – 1.7V – 7.9Si alloys at room temperature.

Powder Size Fraction (Extrusion Ratio)	Yield Strength (MPa)	Ultimate Tensile Strength (MPa)	Total Elongation (%)
−2000+212 μm (144:1)	246.30	265.49	0.90
−212+150 μm (26:1)	247.90	325.36	4.87
−212+150 μm (81:1)	249.68	327.94	5.16
−150+106 μm (26:1)	274.69	333.65	3.61
−150+106 μm (81:1)	300.53	387.21	3.72
−106+90 μm (81:1)	318.94	393.78	3.92
−90 μm (81:1)	342.91	407.61	2.02

Table 4.6 Mechanical properties of Al – 8Fe – 1.7V – 7.9Si alloys at 150 °C.

Powder Size Fraction (Extrusion Ratio)	Yield Strength (MPa)	Ultimate Tensile Strength (MPa)	Total Elongation (%)
−2000+212 μm (144:1)	191.10	212.08	2.13
−212+150 μm (26:1)	212.94	231.85	7.36
−212+150 μm (81:1)	218.15	234.84	7.84
−150+106 μm (26:1)	237.01	253.76	5.04
−150+106 μm (81:1)	238.03	262.96	5.35
−106+90 μm (81:1)	263.50	293.14	7.60
−90 μm (81:1)	282.28	320.83	3.40

Table 4.7 Mechanical properties of Al – 8Fe – 1.7V – 7.9Si alloys at 250 °C.

Powder Size Fraction (Extrusion Ratio)	Yield Strength (MPa)	Ultimate Tensile Strength (MPa)	Total Elongation (%)
−2000+212 μm (144:1)	146.54	158.34	2.66
−212+150 μm (26:1)	161.87	170.06	7.80
−212+150 μm (81:1)	164.46	172.07	8.02
−150+106 μm (26:1)	183.41	196.22	8.20
−150+106 μm (81:1)	193.59	216.60	8.68
−106+90 μm (81:1)	204.26	227.52	9.15
−90 μm (81:1)	238.33	254.51	4.24

Table 4.8 Mechanical properties of Al – 8Fe – 1.7V – 7.9Si alloys at 350 °C.

Powder Size Fraction (Extrusion Ratio)	Yield Strength (MPa)	Ultimate Tensile Strength (MPa)	Total Elongation (%)
−2000+212 μm (144:1)	96.58	101.95	2.91
−212+150 μm (26:1)	99.82	102.05	9.05
−212+150 μm (81:1)	101.63	103.94	9.32
−150+106 μm (26:1)	109.56	119.89	9.15
−150+106 μm (81:1)	118.29	126.17	9.48
−106+90 μm (81:1)	122.38	131.43	10.52
−90 μm (81:1)	133.22	143.17	6.21

Tables 4.5 through 4.8 show clearly that the decrease in powder particle size range and increase in extrusion ratio enhanced the ultimate tensile strength (UTS) and yield strength (YS) at all test temperatures. The powder particle size range had more dominant effect on the tensile properties than the extrusion ratio. After the increase in extrusion ratio, there is a small difference in UTS and YS of the specimens. However, the elongations of the specimens varied differently as powder particle size decreased and extrusion ratio increased. Evidently, the extruded alloys made from finer powders exhibited higher UTS and YS but lower ductility than that made from coarser powders.

The tensile properties of extruded alloys as a function of test temperature are given in Figures 4.34 through 4.36. Furthermore, the effect of powder particle size and extrusion ratio on tensile properties at different temperatures can be understood from these figures. It can be clearly seen from the figures that with increasing test temperatures, both UTS and YS of all alloys decreased but their elongation increased.

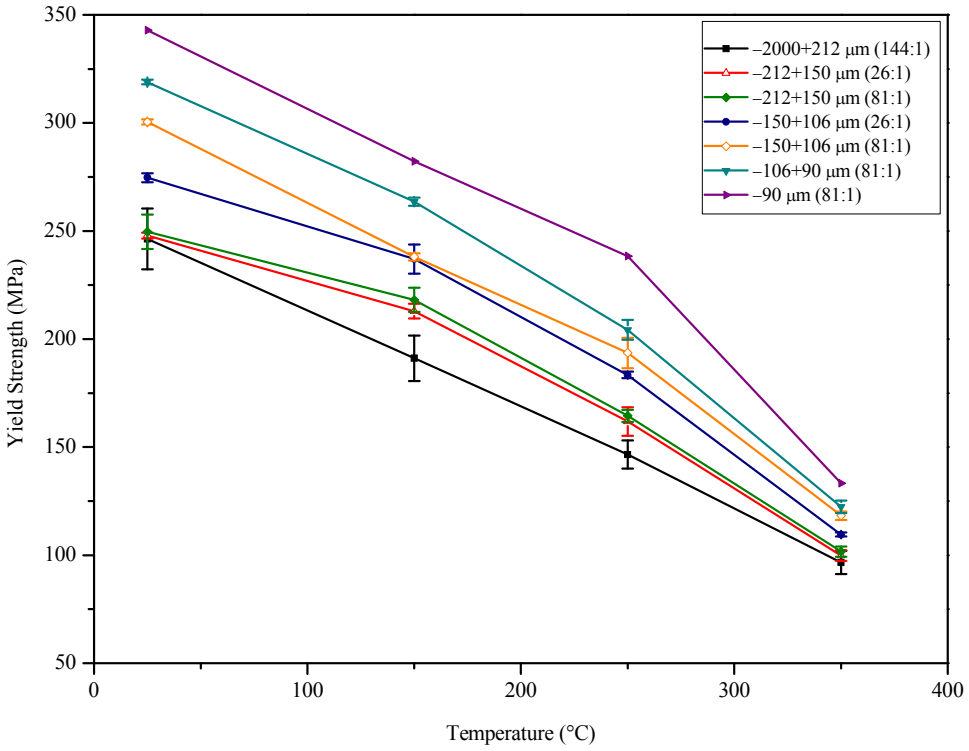

Figure 4.34 The variation in yield strength with test temperature at different powder particle size fraction and extrusion ratio.

It is seen from Figure 4.34 that YS of the extruded specimens decreased with increasing the test temperature. With decreasing powder particle size and increasing extrusion ratio, both room and elevated temperature YS were improved. The highest values were obtained from the specimens made from –90 μm powders and these were 342.91 MPa, 282.28 MPa, 238.33 MPa, and 133.22 MPa at room temperature, 150 °C, 250 °C, and 350 °C, respectively.

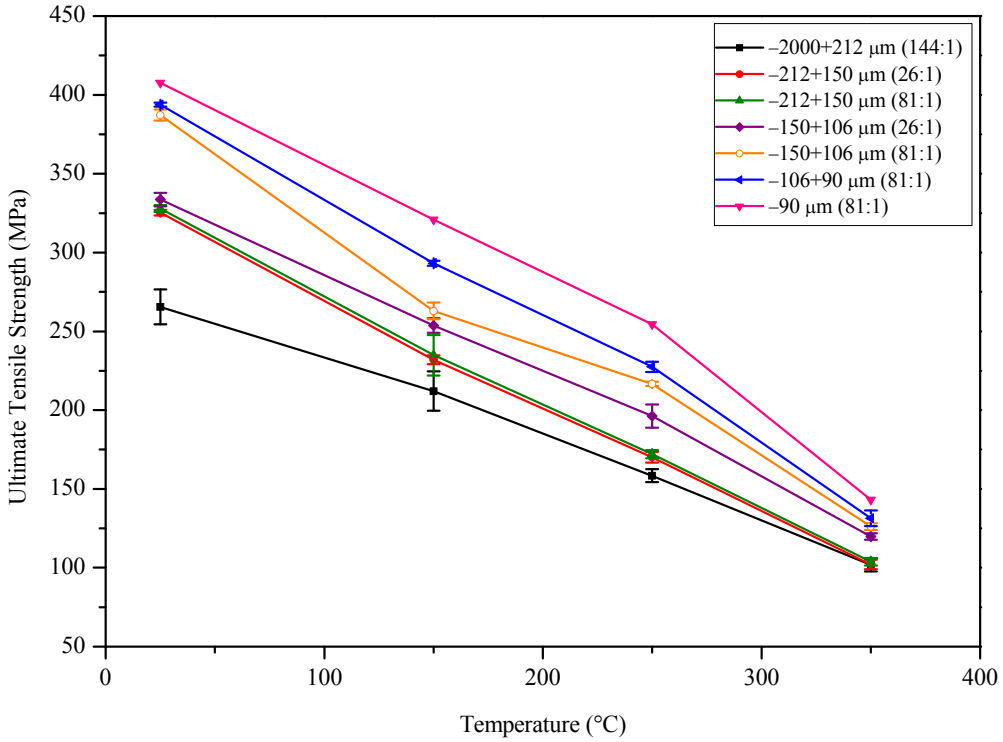

Figure 4.35 The variation in ultimate tensile strength with test temperature at different powder particle size fraction and extrusion ratio.

When Figure 4.35 is examined, it is seen that UTS of the specimens decreased with increasing temperature. Apparently, the UTS values at room temperature, 150 °C, 250 °C, and 350 °C for the extruded alloy produced from the hot extrusion of –90 μm were better than other extruded alloys. Among seven different extruded alloys, the UTS increased from 265.49 to 407.61 MPa (enhanced 53.3%) at room temperature, 212.08 to 320.83 MPa (enhanced 51.3%) at 150 °C, 158.34 to 254.51 MPa (enhanced 60.7%) at 250 °C, and 101.95 to 143.17 MPa (enhanced 40.4%) at 350 °C.

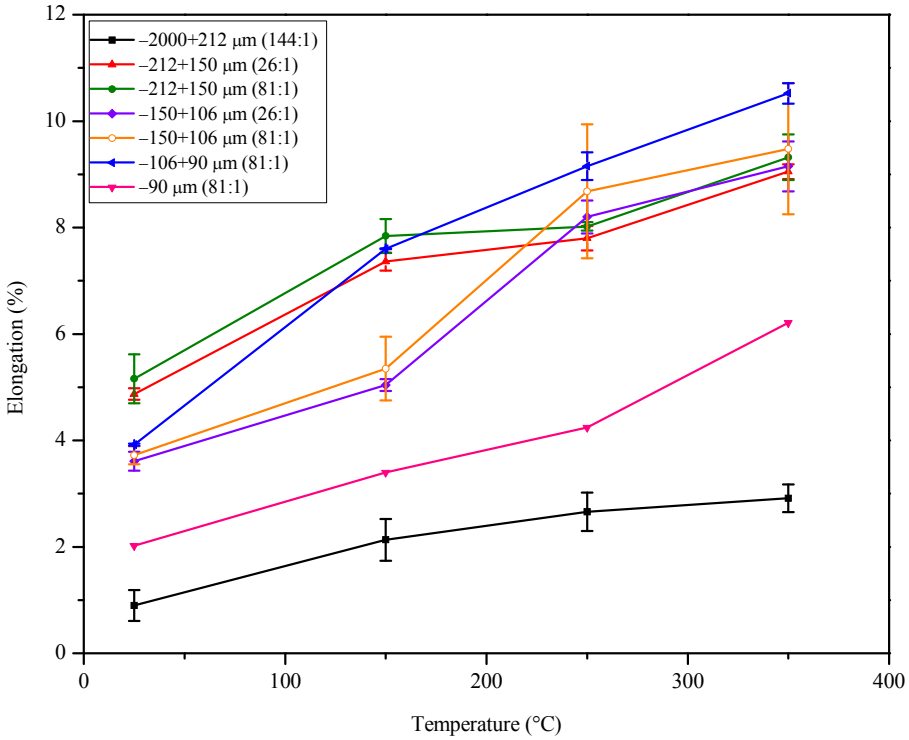

Figure 4.36 The variation in total elongation with test temperature at different powder particle size fraction and extrusion ratio.

Figure 4.36 demonstrates the variation of elongation (%) with test temperature for different extruded alloys, showing that elongation increased not only with increasing temperature but also with increasing extrusion ratio. Extruded alloys produced from –106+90 µm powders with an extrusion ratio 81:1 gave a maximum at 350 °C in elongation. At room temperature, the highest elongation value was obtained from the alloy made from –212+150 µm powders with an extrusion ratio of 81:1. This can be attributed to the coarser powder particle size and higher extrusion ratio. The extruded alloy consolidated from −2000+212 µm powders exhibited the poorest ductility. In other words, its elongation values were the lowest among them because –2000+212 µm powders had high level of surface oxide due to exposure to air and humidity and this resulted in a poor bonding of powders after extrusion. Normally, surface oxidation is directly related to surface area so coarser powders have low level of surface oxide. Furthermore, the alloys made from the

same powder size range but different extrusion ratio showed a slight increase. The increase in elongation aroused from the fact that more uniform distribution of the intermetallic phases were achieved with increasing the extrusion ratio.

4.2.4.2 Fracture Morphology of Extruded Alloys

The fracture surfaces of extruded alloys were studied by SEM in order to obtain information about the nature of fracture and the role of dispersoids ($Al_{13}(Fe, V)_3Si$) on the fracture mode. SEM micrographs of the fracture surfaces of extruded alloys at different test temperature are demonstrated in Figures 4.37 through 4.60. As illustrated in figures, there were equiaxial cup – like depressions (dimples) which had different size and shape in the fracture surfaces. The dimples were distributed throughout the fracture surfaces. This indicated that the fracture mode was dimpled rupture and this type of fracture was an indication of a ductile fracture. The dimpled rupture is composed of three stages. Firstly, microvoids are initiated at second phase particles. Then, the voids grow, and finally the ligaments between the microvoids fracture [39, 49].

The fracture mode did not change with test temperature, powder particle size, and extrusion ratio. On the other hand, the dimple morphology varied with test temperature. At lower temperatures, the dimples became shallower due to lower ductility. Moreover, the amount of dimples increased as test temperature increased because greater dynamic recovery. There was no appreciable difference in the amount and morphology of the dimples of extruded alloys produced from different powder particle size and extrusion ratio.

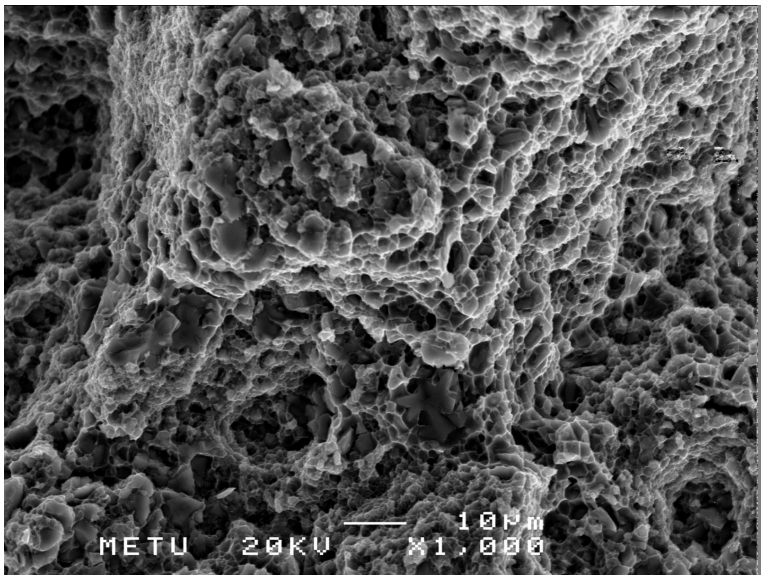

Figure 4.37 SEM micrograph of the fracture surface of the room temperature tensile test specimen of Al – 8Fe – 1.7V – 7.9Si alloy produced by hot extrusion of –2000+212 µm powders (a reduction of 144:1).

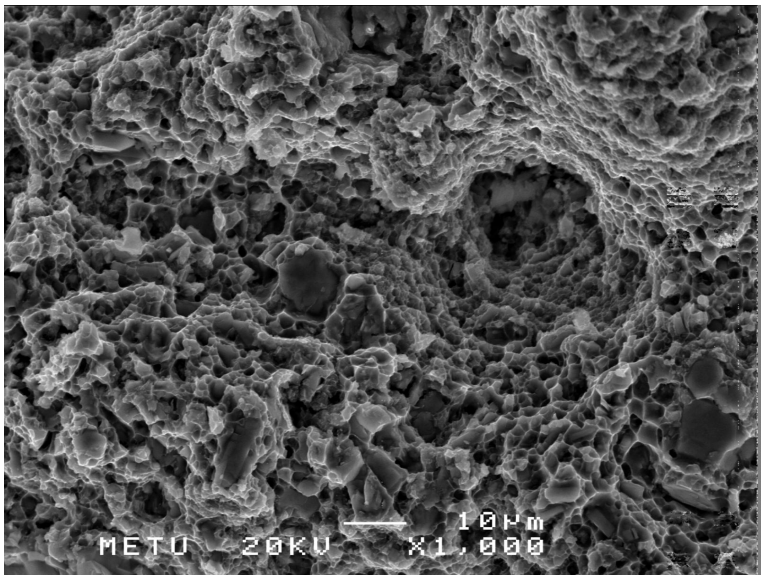

Figure 4.38 SEM micrograph of the fracture surface of the hot tensile test specimen at 150 °C of Al – 8Fe – 1.7V – 7.9Si alloy produced by hot extrusion of –2000+212 µm powders (a reduction of 144:1).

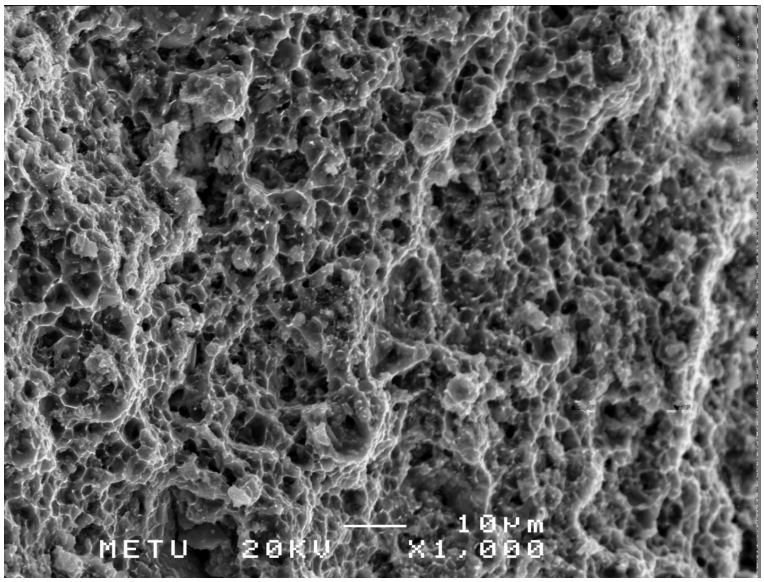

Figure 4.39 SEM micrograph of the fracture surface of the hot tensile test specimen at 250 °C of Al – 8Fe – 1.7V – 7.9Si alloy produced by hot extrusion of –2000+212 µm powders (a reduction of 144:1).

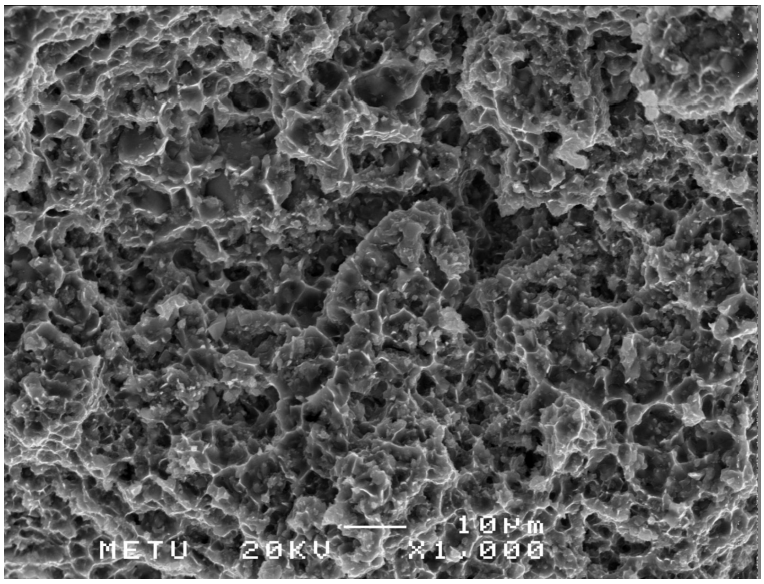

Figure 4.40 SEM micrograph of the fracture surface of the hot tensile test specimen at 350 °C of Al – 8Fe – 1.7V – 7.9Si alloy produced by hot extrusion of –2000+212 µm powders (a reduction of 144:1).

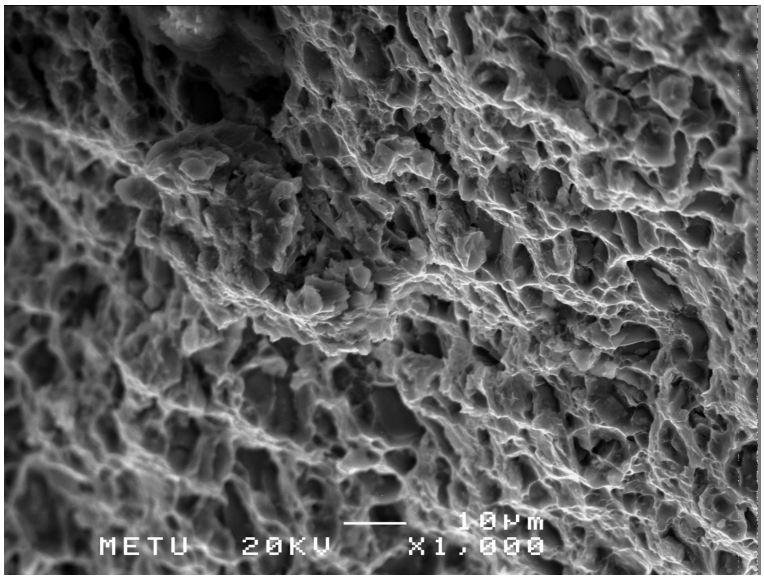

Figure 4.41 SEM micrograph of the fracture surface of the room temperature tensile test specimen of Al – 8Fe – 1.7V – 7.9Si alloy produced by hot extrusion of –212+150 μm powders (a reduction of 26:1).

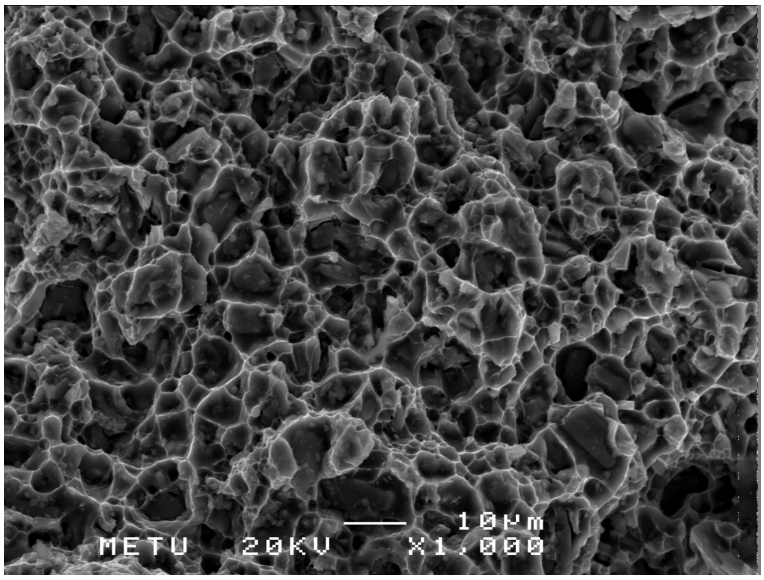

Figure 4.42 SEM micrograph of the fracture surface of the hot tensile test specimen at 150 °C of Al – 8Fe – 1.7V – 7.9Si alloy produced by hot extrusion of –212+150 μm powders (a reduction of 26:1).

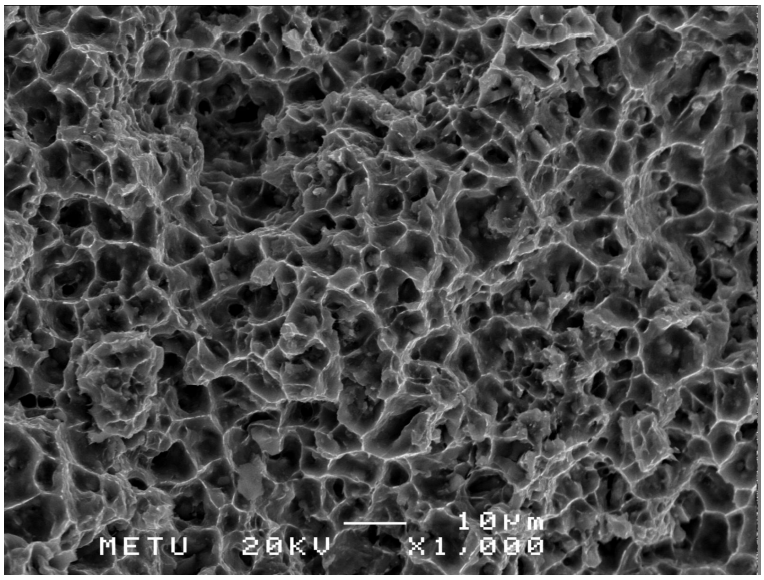

Figure 4.43 SEM micrograph of the fracture surface of the hot tensile test specimen at 250 °C of Al – 8Fe – 1.7V – 7.9Si alloy produced by hot extrusion of –212+150 µm powders (a reduction of 26:1).

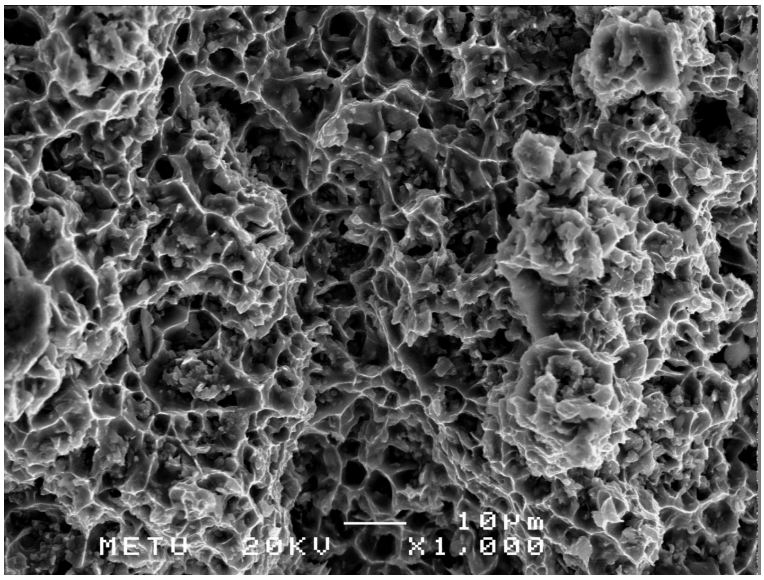

Figure 4.44 SEM micrograph of the fracture surface of the hot tensile test specimen at 350 °C of Al – 8Fe – 1.7V – 7.9Si alloy produced by hot extrusion of –212+150 µm powders (a reduction of 26:1).

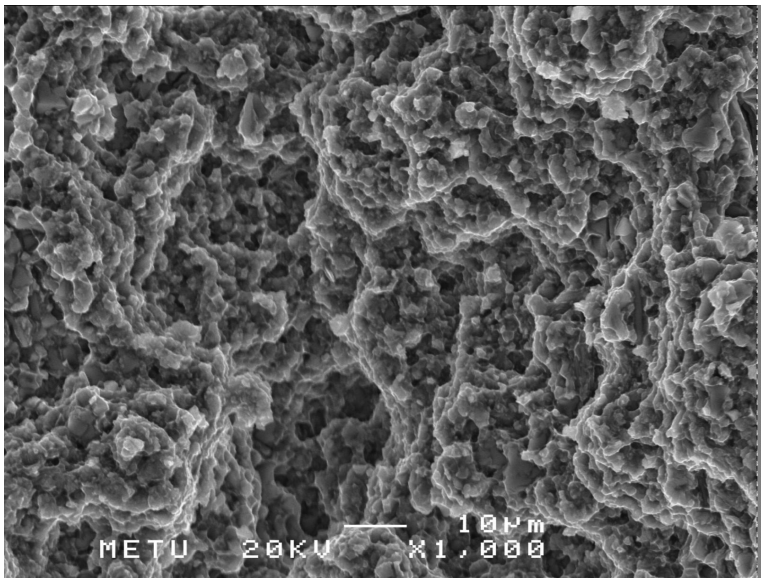

Figure 4.45 SEM micrograph of the fracture surface of the room temperature tensile test specimen of Al – 8Fe – 1.7V – 7.9Si alloy produced by hot extrusion of –212+150 µm powders (a reduction of 81:1).

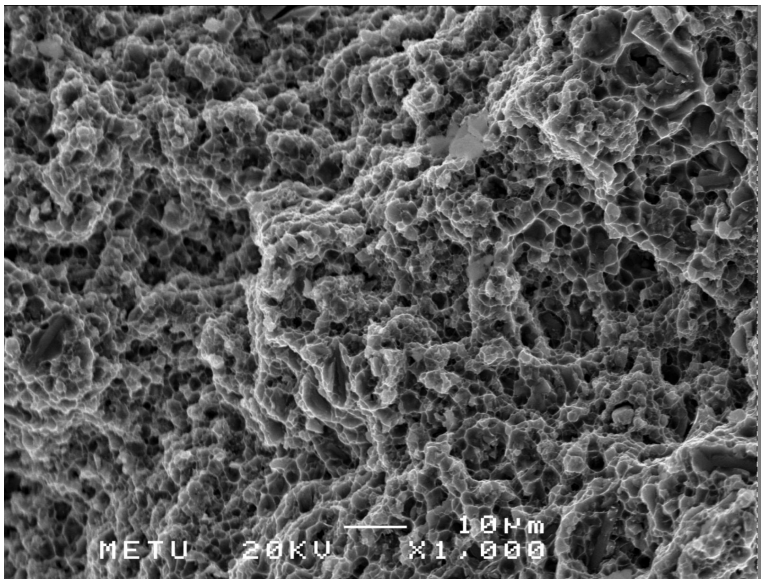

Figure 4.46 SEM micrograph of the fracture surface of the hot tensile test specimen at 150 °C of Al – 8Fe – 1.7V – 7.9Si alloy produced by hot extrusion of –212+150 µm powders (a reduction of 81:1).

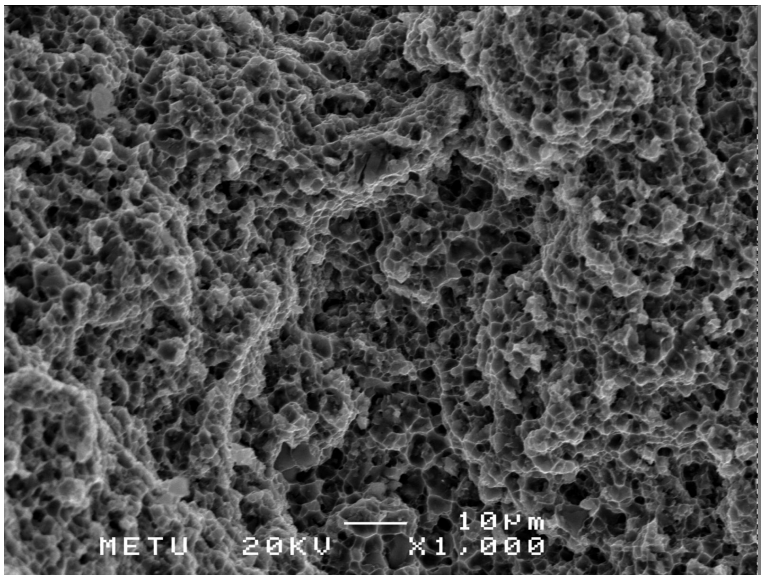

Figure 4.47 SEM micrograph of the fracture surface of the hot tensile test specimen at 250 °C of Al – 8Fe – 1.7V – 7.9Si alloy produced by hot extrusion of –212+150 µm powders (a reduction of 81:1).

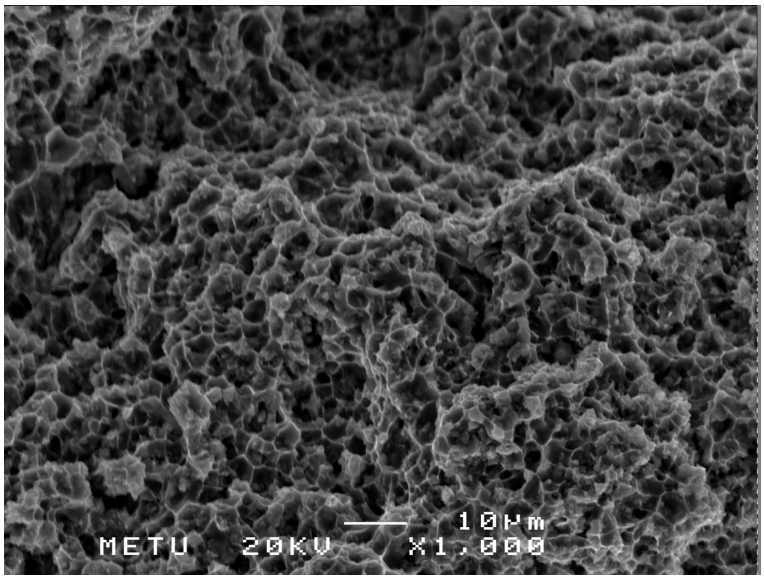

Figure 4.48 SEM micrograph of the fracture surface of the hot tensile test specimen at 350 °C of Al – 8Fe – 1.7V – 7.9Si alloy produced by hot extrusion of –212+150 µm powders (a reduction of 81:1).

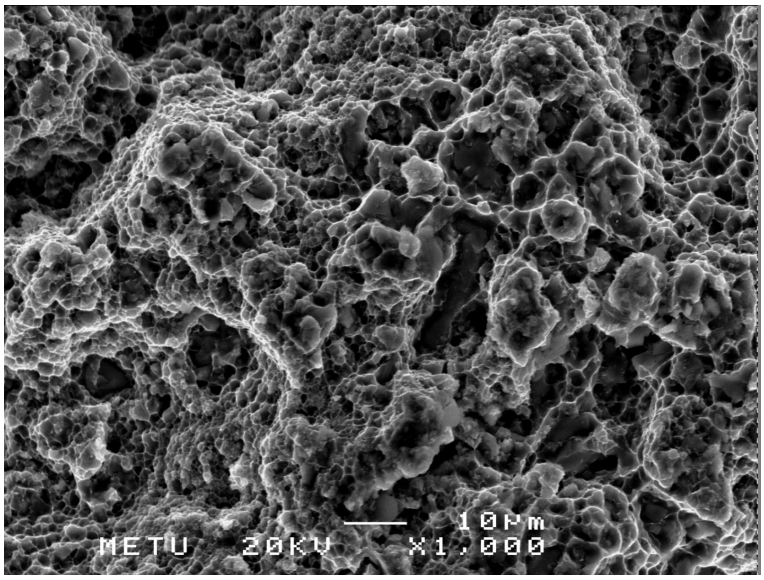

Figure 4.49 SEM micrograph of the fracture surface of the room temperature tensile test specimen of Al – 8Fe – 1.7V – 7.9Si alloy produced by hot extrusion of –150+106 μm powders (a reduction of 26:1).

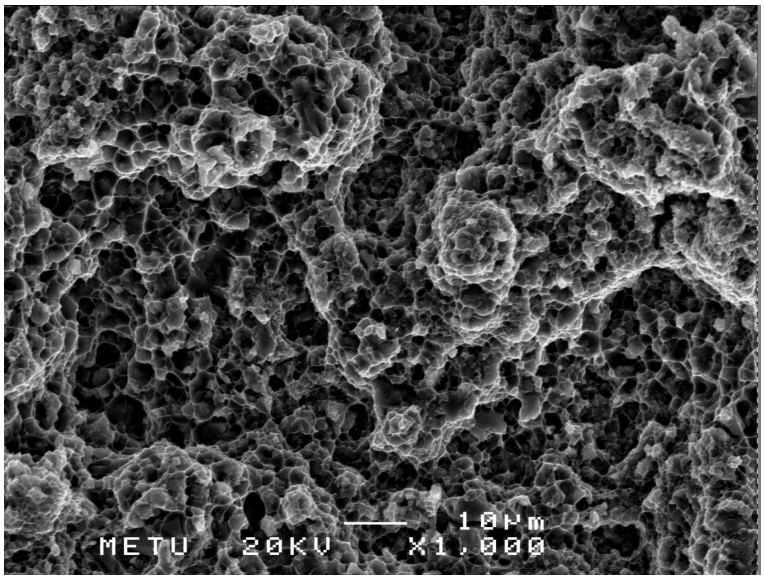

Figure 4.50 SEM micrograph of the fracture surface of the hot tensile test specimen at 150 °C of Al – 8Fe – 1.7V – 7.9Si alloy produced by hot extrusion of –150+106 μm powders (a reduction of 26:1).

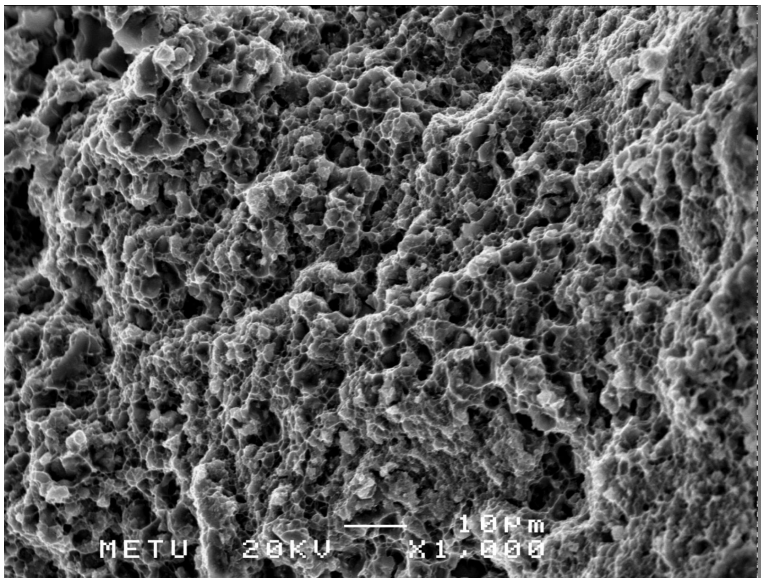

Figure 4.51 SEM micrograph of the fracture surface of the hot tensile test specimen at 250 °C of Al – 8Fe – 1.7V – 7.9Si alloy produced by hot extrusion of –150+106 µm powders (a reduction of 26:1).

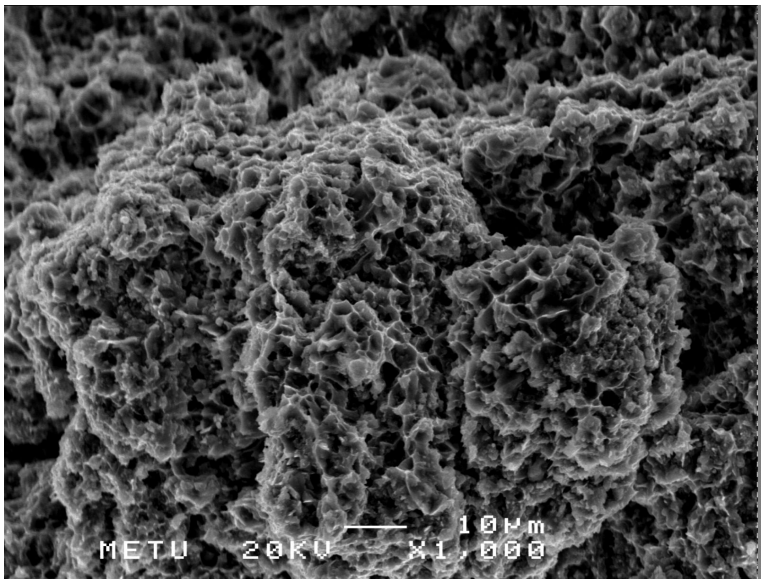

Figure 4.52 SEM micrograph of the fracture surface of the hot tensile test specimen at 350 °C of Al – 8Fe – 1.7V – 7.9Si alloy produced by hot extrusion of –150+106 µm powders (a reduction of 26:1).

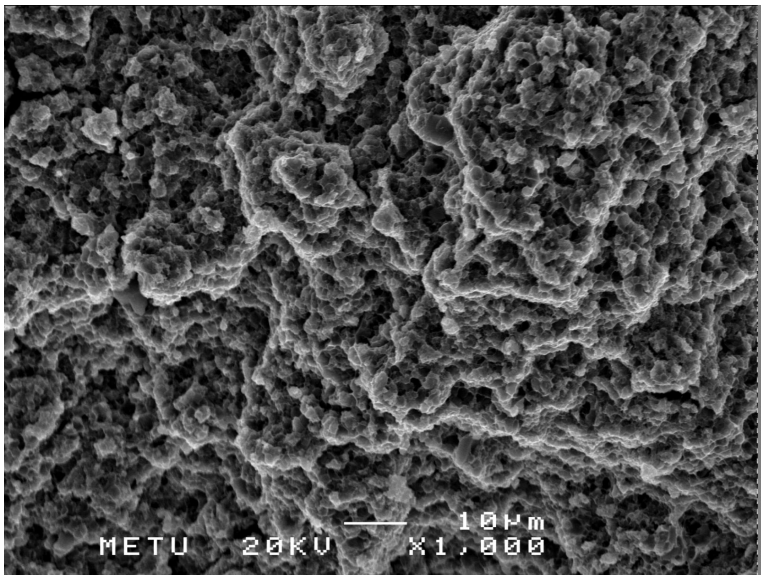

Figure 4.53 SEM micrograph of the fracture surface of the room temperature tensile test specimen of Al – 8Fe – 1.7V – 7.9Si alloy produced by hot extrusion of –106+90 µm powders (a reduction of 81:1).

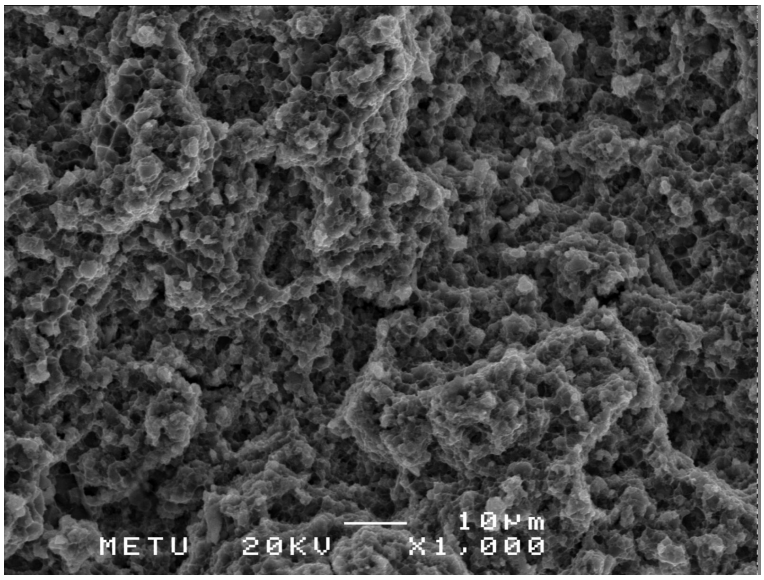

Figure 4.54 SEM micrograph of the fracture surface of the hot tensile test specimen at 150 °C of Al – 8Fe – 1.7V – 7.9Si alloy produced by hot extrusion of –106+90 µm powders (a reduction of 81:1).

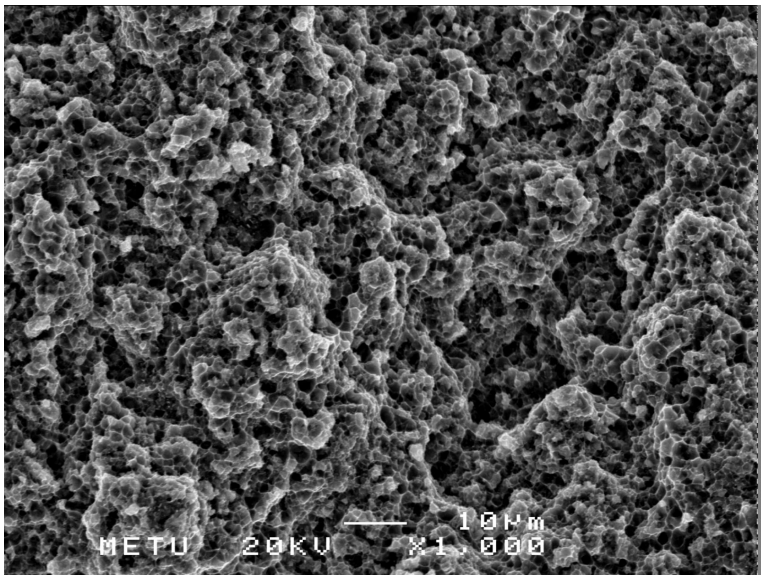

Figure 4.55 SEM micrograph of the fracture surface of the hot tensile test specimen at 250 °C of Al – 8Fe – 1.7V – 7.9Si alloy produced by hot extrusion of –106+90 µm powders (a reduction of 81:1).

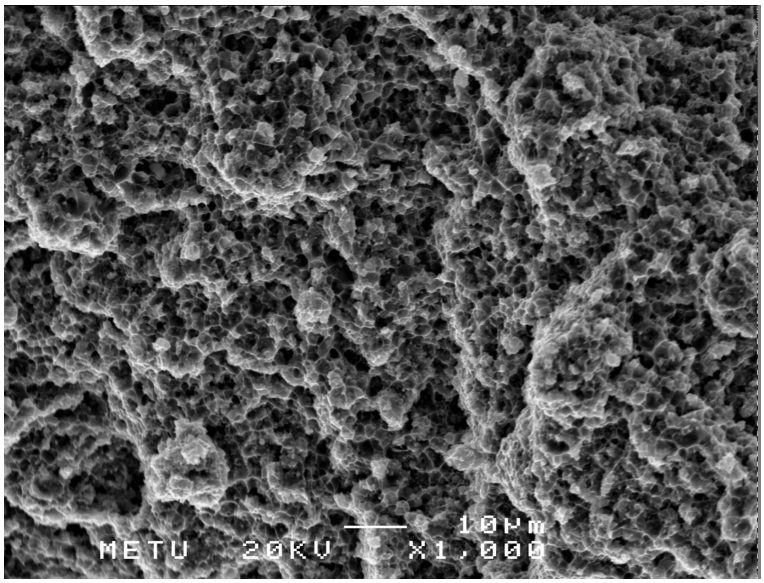

Figure 4.56 SEM micrograph of the fracture surface of the hot tensile test specimen at 350 °C of Al – 8Fe – 1.7V – 7.9Si alloy produced by hot extrusion of –106+90 µm powders (a reduction of 81:1).

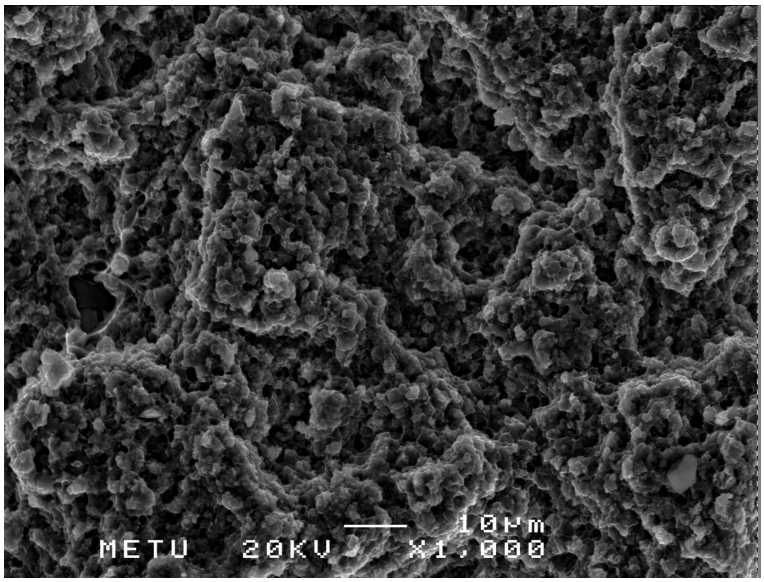

Figure 4.57 SEM micrograph of the fracture surface of the room temperature tensile test specimen of Al – 8Fe – 1.7V – 7.9Si alloy produced by hot extrusion of –90 µm powders (a reduction of 81:1).

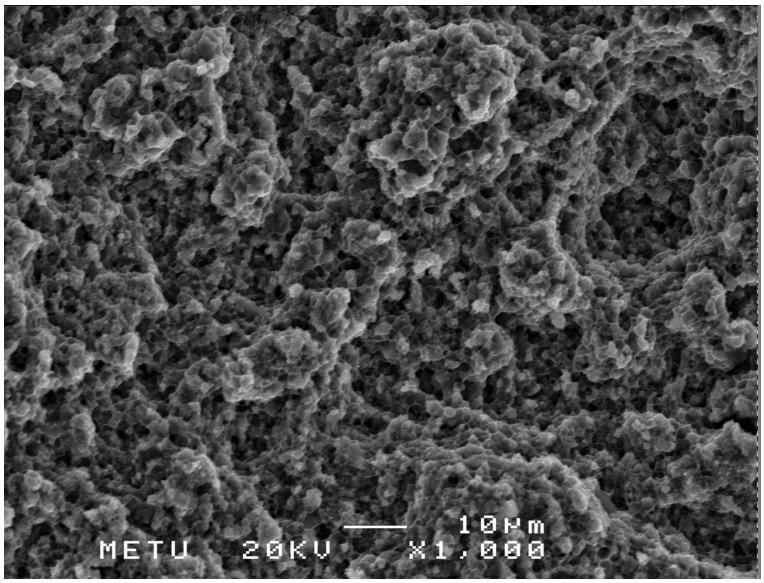

Figure 4.58 SEM micrograph of the fracture surface of the hot tensile test specimen at 150 °C of Al – 8Fe – 1.7V – 7.9Si alloy produced by hot extrusion of –90 µm powders (a reduction of 81:1).

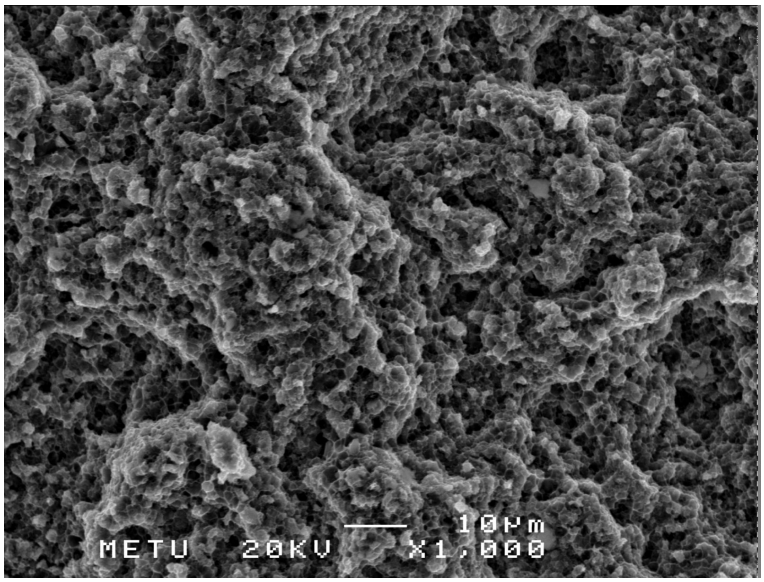

Figure 4.59 SEM micrograph of the fracture surface of the hot tensile test specimen at 250 °C of Al – 8Fe – 1.7V – 7.9Si alloy produced by hot extrusion of –90 µm powders (a reduction of 81:1).

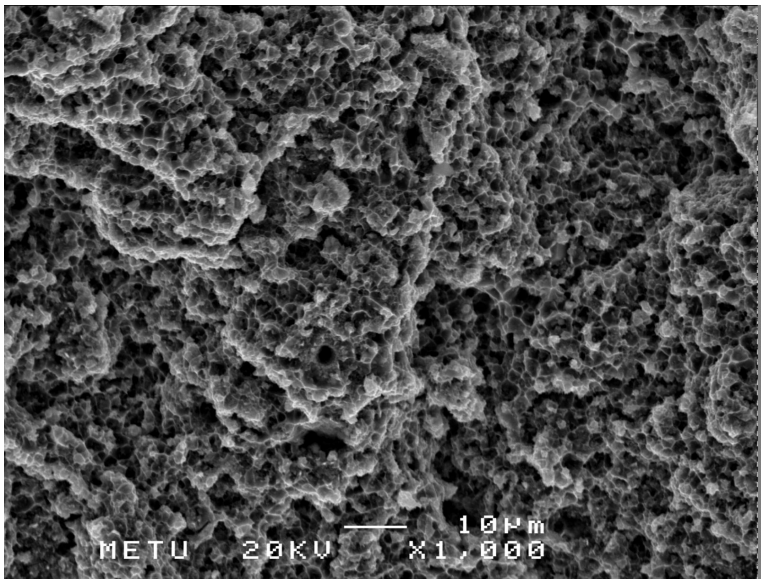

Figure 4.60 SEM micrograph of the fracture surface of the hot tensile test specimen at 350 °C of Al – 8Fe – 1.7V – 7.9Si alloy produced by hot extrusion of –90 µm powders (a reduction of 81:1).

4.2.4.3 Hardness Test Analysis of Extruded Alloys

Hardness gives a good indication of metal's resistance to plastic deformation [49] so hardness tests were performed to observe the effect of powder particle size, extrusion ratio and extrusion direction on the extruded alloys. The comparison and change in hardness values with powder particle size, extrusion ratio and direction are illustrated in Figure 4.61 and Figure 4.62. The hardness test results of all specimens are reported in Appendix C.

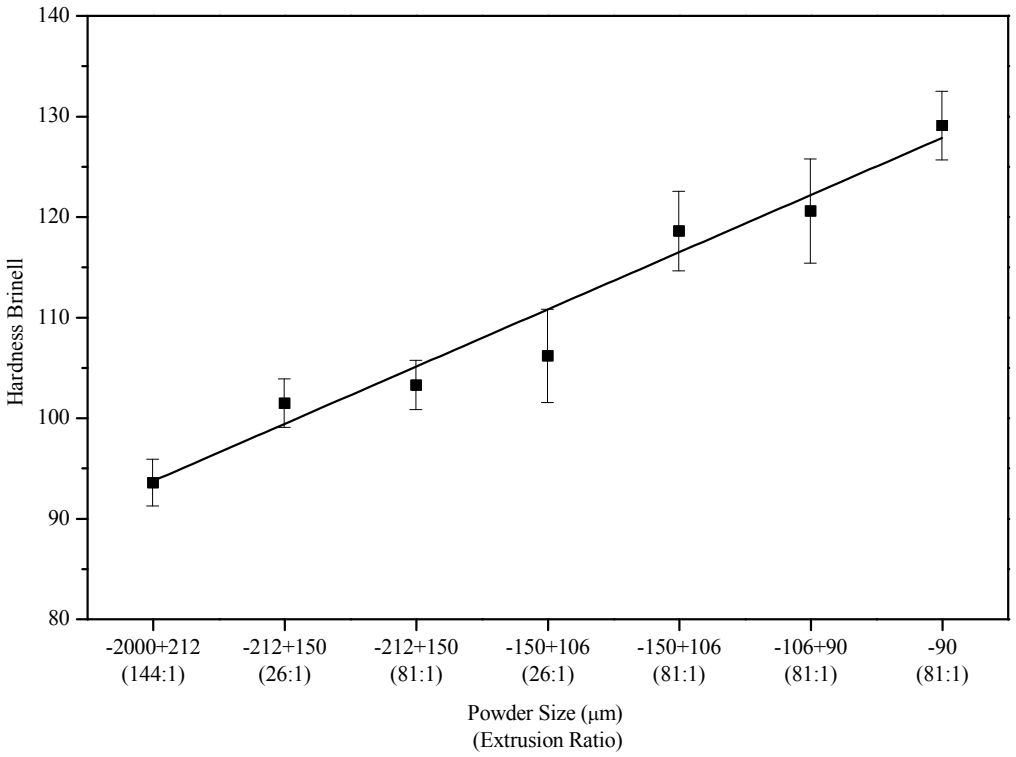

Figure 4.61 Variation in hardness values taken parallel to the extrusion direction as a function of powder particle size and extrusion ratio.

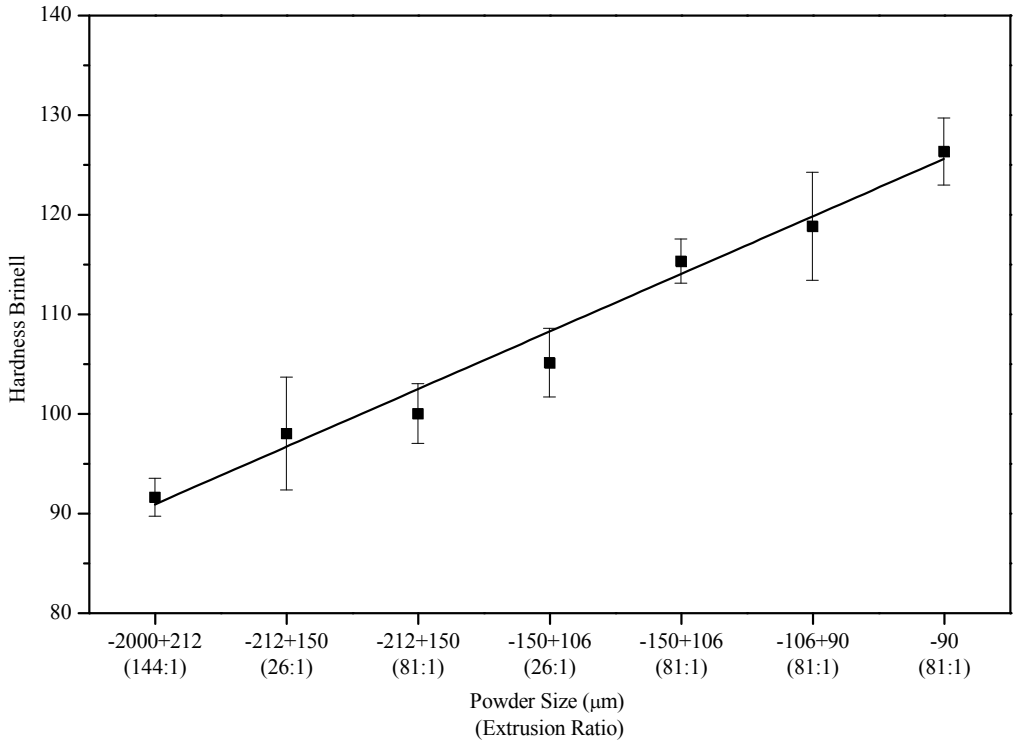

Figure 4.62 Variation in hardness values taken vertical to the extrusion direction as a function of powder particle size and extrusion ratio.

The hardness values increased with decrease in powder particle size as it can be seen in Figure 4.61 and Figure 4.62. As powder particle size decreased, the size of dispersoids that are quaternary intermetallic silicides having much higher strength than the aluminum matrix decreased and their volume fraction in the microstructure of the extruded alloys increased. These dispersoids act as barriers to dislocation motion and lead to strain hardening [49]. Moreover, the alloys produced by hot extrusion of finer powder particle size had finer grains and this resulted in increase in hardness. Apart from these, the additional rise in hardness was achieved with an increase in extrusion ratio. The degree of strengthening resulting from dispersoids depends on the distribution of dispersoids in the ductile matrix [49]. Therefore, the distribution of dispersoids was improved by increasing extrusion ratio.

The results obtained from samples prepared by surfaces parallel to extrusion direction were slightly higher than that of perpendicular to extrusion direction. This small difference between hardness values was owing to the texture produced by the extrusion. The highest hardness value parallel and vertical to the extrusion direction was 135 and 131 for the extruded alloys produced by hot extrusion of –90 μm powders with an extrusion ratio of 81:1, respectively.

CHAPTER 5

CONCLUSIONS

In the present study concerning the production of high performance Al – 8Fe – 1.7V – 7.9 Si alloy via powder metallurgy, the following major conclusions have been drawn:

1. The air atomized Al – Fe – V – Si alloy powder particles produced in the present study exhibited rounded and irregular shape in all powder fractions.

2. XRD investigations revealed the microstructure of the as – atomized alloys consisted of dispersoids distributed in the aluminum matrix. The structure of these dispersoids was a bcc α – $Al_{13}(Fe, V)_3Si$. The volume fraction of these intermetallic phases increased as the powder particle size decreased.

3. Solubility limit extension for 7.9% Si (in wt%) was valid because there was no primary Si crystal formation.

4. There was only one exotherm peak observed in the as – atomized powder particles. This was an indicator of a phase transformation. The possible phase transformation reaction occurring at 581 °C was the precipitation of the equilibrium phases from silicide particles ($Al_{13}(Fe, V)_3Si$). The powder consolidation temperature should be lower than 581°C. Above that temperature, powder consolidation led to the transformation of intermetallic phases to equilibrium phases that are detrimental to the high performance elevated temperature alloy.

5. The microstructure of the extruded alloys was very fine. It was composed of dispersoids of α – $Al_{13}(Fe, V)_3Si$ in α – Al solid solution matrix. The volume fraction of the dispersoids increased after hot extrusion in all alloys. The finer powder particle size that the alloy was produced from, the more increase in the volume fraction of dispersoids. This was due to higher degree of supersaturation, which yielded to the formation of additional $Al_{13}(Fe, V)_3Si$ dispersoids, of finer powders.

6. The matrix grain size of the extruded Al – Fe – V – Si alloys investigated was very fine. Finer grains were obtained at finer powders and higher extrusion ratios.

7. The optical microscopy and SEM indicated that the microstructure of the extruded alloys was inhomogeneous and a noticeable lamellar structure existed along the longitudinal sections of the extrudates. There were bands of regions containing fine and coarse dispersoids that were aligned with an alternate dark and bright contrast in the material flow direction. The initial powder particle size and extrusion ratio had an influence on the homogeneity and fineness of the alloys' microstructures. With decreasing powder particle size and increasing extrusion ratio, much finer and more uniform microstructures that contained very fine dispersoids were obtained.

8. The mechanical properties of Al – Fe – V – Si alloys produced by means of powder metallurgy were greatly increased. The improvement of mechanical properties was due to the refinement of microstructure and fine dispersoids distributed in Al matrix.

9. The powder particle size and extrusion ratio influenced the mechanical properties of extrudates. Finer powder particle size and higher extrusion ratio resulted in high UTS and YS but low elongation. The effect of powder particle size was greater than that of extrusion ratio.

10. As the test temperature increased, UTS and YS decreased whereas elongation increased for all extruded alloys.

11. UTS and YS of the alloy produced from –90 μm powders were the highest at room and elevated temperatures. The reason of this behaviour was attributed to more uniform and finer microstructure of this extrudates and higher volume fraction of the intermetallic phase in the matrix. The highest enhancement in mechanical properties of the extrudates obtained was the 60.7% increase in UTS at 250 °C. This was gained compared to the extruded alloy made from –2000+212 μm powders with an extrusion ratio of 144:1.

12. The extrudate produced from –106+90 μm powders gave a maximum at 350 °C in elongation.

13. The fracture mode was dimpled rupture and it can be concluded that this type of fracture was an indication of a ductile fracture. The fracture mode did not change with test temperature, powder particle size, and extrusion ratio.

14. Hardness values were inversely proportional to the powder particle size. Hardness increased with decreasing powder particle size. Higher extrusion ratio also provided the additional increase in hardness. It was observed that hardness values for parallel to extrusion direction were slightly higher than that for perpendicular to extrusion direction.

REFERENCES

1. J. R. Davis and Associates, eds, "*ASM Specialty Handbook: Aluminum and Aluminum Alloys"*, 1993, ASM International: Ohio.

2. J. R. Davis and Associates, eds, "*ASM Metals Handbook: Properties and Selection: Nonferrous Alloys and Special - Purpose Materials"*, 1992, ASM International: Ohio.

3. E. J. Lavernia, J. D. Ayers, and T. S. Srivatsan, "*Rapid Solidification Processing with Specific Application to Aluminium Alloys"*, International Materials Review, 1992, 37 (1): p. 1 - 42.

4. J. Q. Wang, M. K. Tseng, X. F. Chen, B. J. Zhang, and Z. Xianyu, "*An Investigation on the Microstructure Stability of Rapidly Solidified Al - Fe - V - Si Alloy Ribbon"*, Materials Science and Engineering, 1994, A179 / A180: p. 412 - 415.

5. A. K. Srivastava and S. Ranganathan, "*Microstructural Characterization of Rapidly Solidified Al - Fe - Si, Al - V - Si, and Al - Fe - V - Si Alloys"*, Journal Of Materials Research, 2001, 16 (7): p. 2103 - 2117.

6. W. J. Park, S. Ahn, and N. J. Kim, "*Evolution of Microstructure in A Rapidly Solidified Al - Fe - V - Si Alloy "*, Materials Science and Engineering, 1994, A(189): p. 291 - 299.

7. Y. W. Kim and W. M. Griffith, eds, "*Dispersion Strengthened Aluminium Alloys"*, 1988, AIME: Warrendale, PA.

8. S. K. Das and L. A. Davis, "*High Performance Aerospace Alloys via Rapid Solidification Processing "*, Materials Science and Engineering, 1998, 98: p. 1 - 12.

9. U. Prakash, T. Raghu, A. A. Gokhale, and S. V. Kamat, "*Microstructure and Mechanical Properties of RSP / M Al - Fe - V - Si and Al - Fe - Ce Alloys"*, Journal of Materials Science, 1999, 34: p. 5061 - 5065.

10. R. Tongsri, E. J. Minay, R. P. Thackray, R. J. Dashwood, and H. B. Mcshane, "*Microstructural and Their Stability in Rapidly Solidified Al - Fe - (V, Si) Alloy Powders"*, Journal of Materials Science, 2001, 36: p. 1845 - 1856.

11. S. Yaneva, A. Kalkanlı, K. Petrov, R. Petrov, I. Y. Houbaert, and S. Kassabov, "*Structure Development in Rapidly Solidified Al - Fe - V - Si Ribbons"*, Materials Science and Engineering, 2004, A373: p. 90 - 98.

12. Y. Wang, G. W. Lorimer, and F. R. Sale, "*Microstructural Development During Consolidation of Rapidly Solidified Al - Fe - V - Si Powder by VHP, Extrusion and Rolling"*, Scripta Metallurgica et Materialia, 1994, 31 (10): p. 1337 - 1342.

13. G. Haour and P. G. Boswell, "*Rapidly Solidified Materials - A Status Report"*, Materials and Design, 1987, 8 (1): p. 10 -12.

14. T. S. Srivatsan and T. S. Sudarshan, eds, "*Rapid Solidification Technology: An Engineering Guide"*, 1993, Technomic Publishing Company Inc.: Pennsylvania.

15. R. M. German, "*Powder Metallurgy Science*", 1997, New Jersey: Metal Powder Industries Federation.

16. I. T. H. Chang and H. S. Nalwa, "*Handbook of Nanostructured Materials and Nanotechnology*", 2000, Burlington: Academic Press.

17. H. Jones and C. Suryanarayana, "*Pergamon Materials Series*", Vol. 2, 1999: Pergamon.

18. J. W. Christian, "*The Theory of Transformations in Metals and Alloys*", 2002, Oxford: Pergamon.

19. J. R. Davis and Associates, eds, "*ASM Metals Handbook: Powder Metal Technologies and Applications "*, 1990, ASM International: Ohio.

20. A. J. Yule and J. J. Dunkley, "*Atomization of Melts for Powder Production and Spray Deposition*", 1994, New York: Oxford University Press Inc.

21. H. Biloni, W. J. Boettinger, W. C. Robert, and P. Haasen, "*Physical Metallurgy* ", 4 ed, 1996, Oxford: North - Holland.

22. A. Kalkanlı;, J. V. Wood;, and N. Braithwaite, "*Melt Instabilities and the Effect of Surface Tension on Preventing Edge Serrations in Melt Overflow Alloy Strip Casting"*, ISIJ International, 1998, 38 (2): p. 142-148.

23. A. Lawley, "*Atomization: The Production of Metal Powders*", 1992, New Jersey: Metal Powder Industries Federation.

24. H. A. Kuhn and A. Lawley, eds, "*Powder Metallurgy Processing: New Techniques and Analyses"*, 1978, Academic Press: New York.

25. F. Thümmler and R. Oberacker, "*An Introduction to Powder Metallurgy*", I. Jenkins and J.V. Wood, 1993, London: The Institute of Materials.

26. J. S. Hirschhorn, "*Introduction to Powder Metallurgy*", 2nd ed, 1976, New Jersey: American Powder Metallurgy Institute.

27. J. J. Dunkley, "*Production of Metal Powders by Water Atomisation"*, Wire Industry, 1978, V45: p. 38 - 41.

28. H. H. Hausner, K. H. Roll, and P. K. Johnson, eds, "*New Methods for The Consolidation of Metal Powders"*, 1967, Metal Powder Industries Federation: New York.

29. L. F. Pease and W. G. West, "*Fundamentals of Powder Metallurgy*", 2002, Princeton, N. J.: Metal Powder Industries Federation.

30. A. Kalkanlı, R. Gürbüz, N. Akgün, N. Stoichev, N. Djulgerov, and T. Özdemir, *Mechanical Characterization of Powder Extruded AlFeVSi Alloy Composites for High Temperature Application*.

31. W. G. J. Bunk, "*Aluminium RS Metallurgy"*, Materials Science and Engineering A, 1991, A134: p. 1087 - 1097.

32. H. J. Koh, W. J. Park, and N. J. Kim, "*Identification of Metastable Phases in Strip - cast and Spray - cast Al - Fe - V - Si Alloys "*, Materials Transactions, 1998, 39 (9): p. 982 - 988.

33. K. L. Sahoo, C. S. Sivaramakrishnan, and A. K. Chakrabarti, "*The Effects of Mg Treatment on the Properties of Al - 8.3Fe - 0.8V - 0.9Si Alloy"*, Journal of Materials Processing Technology, 2001, 112: p. 6 - 11.

34. A. K. Srivastava, S. N. Ojha, and S. Ranganathan, "*Microstructural Features and Heat Flow Analysis of Atomized and Spray - Formed Al - Fe - V - Si Alloy"*, Metallurgical and Materials Transactions A, 1998, 29A: p. 2205 - 2219.

35. R. Tongsri, R. Dashwood, and H. Mcshane, "*Microstructure and Solidification of Al - Fe - (V, Si) Alloy Powders"*, Science Asia, 2004, 30: p. 33 - 41.

36. F. Carreno, M. T. Perez - Prado, G. Gonzalez - Doncel, and O. A. Ruano, "*Texture Stability of A Rapidly Solidified Dispersion Strengthened Al - Fe - V - Si Material"*, Scripta Metallurgica et Materialia, 1998, 38 (9): p. 1427 - 1433.

37. V. R. V. Ramanan, D. J. Skinner, and M. S. Zedalis, "*On the Nature of Icosahedral Phases in Al - (Fe, V, Si) Alloys"*, Materials Science and Engineering, 1991, A134: p. 912 - 916.

38. Y. Wang, Z. Chen, X. Jiang, and D. Zhou, "*The Effect of Powder Characteristics on the Microstructure and Properties of RS Al - Fe - V- Si Alloys"*, in *The 3rd International Conference on ALUMINIUM ALLOYS*, 1991: p. 193 - 197.

39. Q. Yan, D. Fu, X. Deng, H. Zhang, and Z. Chen, "*Tensile Deformation Behavior of Spray - Deposited FVS0812 Heat - Resistant Aluminum Alloy Sheet at Elevated Temperatures"*, Materials Characterization, 2007, 58: p. 575 - 579.

40. F. Carreno, M. Eddahbi, and O. A. Ruano, "*Creep Behaviour of Three Dispersion - Strengthened Al - Fe - V - Si Materials"*, Journal of Materials Science Letters, 1997, 16: p. 1728 - 1730.

41. Y. Tang, D. Tan, W. Li , Z. Pan, L. Liu , and W. Hu, "*Preparation of Al - Fe - V - Si Alloy by Spray Co - deposition with Added its Over - sprayed Powders"*, Journal of Alloys ad Compounds, 2007, 439: p. 103 - 108.

42. B. D. Cullity and S. R. Stock, "*Elements of X - Ray Diffraction*", Third ed, 2001, New Jersey: Prentice-Hall, Inc., p. 385 - 435.

43. M. A. Zaidi, "*Microstructure of Rapidly Solidified Aluminum Alloy Powders for Elevated Temperature Applications"*, Materials Science and Engineering, 1988, 98: p. 221 - 226.

44. J. D. Cotton and M. J. Kaufman, "*Microstructural Evolution in Rapidly Solidified Al - Fe Alloys: An Alternative Explanation"*, Metallurgical Transactions A, 1991, 22A: p. 927 - 933.

45. A. Griger and V. Stefaniay, "*Equilibrium and Non - equilibrium Intermetallic Phases in Al - Fe and Al - Fe - Si Alloys"*, Journal of Materials Science, 1996, 31: p. 6645 - 6652.

46. S. Hariprasad, S. M. L. Sastry, and K. L. Jerina, "*Undercooling and Supersaturation of Alloying Elements in Rapidly Solidified Al - 8.5% Fe - 1.2% V - 1.7% Si Alloy"*, Journal of Materials Science, 1996, 31: p. 921 - 925.

47. B. Aral, *Characterization of Rapidly Solidified Al - Fe - V - Si Alloy Powders*, in *Department of Metallurgical and Materials Engineering*, 2001, Middle East Technical University: Ankara.

48. A. K. Srivastava, V. C. Srivastava, A. Gloter, and S. N. Ojha, "*Microstructural features induced by spray processing and hot extrusion of an Al-18% Si-5% Fe-1.5% Cu alloy"*, Acta Materialia, 2006, 54 (7): p. 1741-1748.

49. G. E. Dieter, "*Mechanical Metallurgy*", SI Metric ed, 1988, Singapore: McGrow-Hill Book Company (UK) Limited, p. 184 - 210.

50. C. Zhenhua, H. Peiyun, J. Xiangyang, W. Yun, P. Chanqun, and S. Zhangming, "*Multilayer Spray Forming Process and Setup"*, Materials Science Forum, 1996, 217 - 222: p. 317 - 322.

APPENDIX A

X – RAY DIFFRACTION CARDS OF PRESENT PHASES

Table A.1 X – Ray details of Aluminum.

04-0787 Quality: *
CAS Number: 7429-90-5
Molecular Weight: 26.98
Volume[CD]: 66.40
Dx: 2.699 Dm:
Sys: Cubic
Lattice: Face-centered
S.G.: Fm3̄m (225)
Cell Parameters:
a 4.049 b c
α β γ
SS/FOM: F 9=93(.0108, 9)
I/Icor: 3.62
Rad: CuKa1
Lambda: 1.54056
Filter: Ni
d-sp:
Mineral Name:
Aluminum, syn

Al
Aluminum
Ref: Swanson, Tatge, Natl. Bur. Stand. (U.S.), Circ. 539, I, 11 (1953)

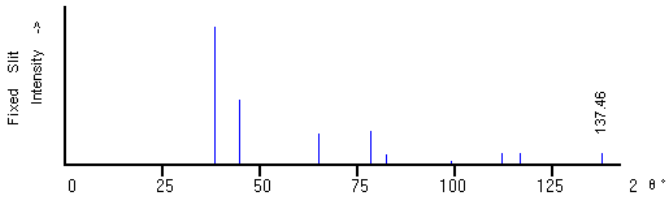

2θ	Int-f	h	k	l	2θ	Int-f	h	k	l	2θ	Int-f	h	k	l
38.472	100	1	1	1	78.227	24	3	1	1	112.04	8	3	3	1
44.738	47	2	0	0	82.435	7	2	2	2	116.56	8	4	2	0
65.133	22	2	2	0	99.078	2	4	0	0	137.45	8	4	2	2

Table A.2 X – Ray details of α – $Al_{13}(Fe, V)_3Si$.

51-1193 Quality:
CAS Number:
Molecular Weight: 544.33
Volume[CD]: 2000.38
Dx: 3.615 Dm:
Sys: Cubic
Lattice: Primitive
S.G.: P
Cell Parameters:
a 12.60 b c
α β γ
SS/FOM: F14= 1 (0.162, 83)
I/Icor:
Rad:
Lambda:
Filter:
d-sp:

α-Al13 (Fe , V)3 Si
Aluminum Iron Silicon Vanadium
Ref: Wang, J et al., Int. J. Non-Equilibrium Proc., 10, 83 (1997)

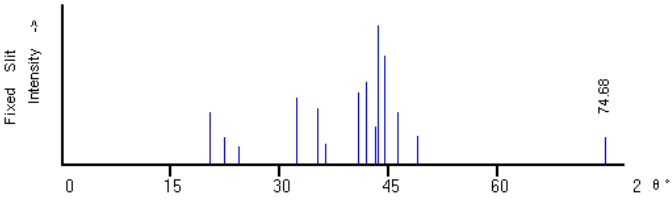

2θ	Int-f	h	k	l	2θ	Int-f	h	k	l	2θ	Int-f	h	k	l
20.305	37	2	2	0	36.342	15	5	1	0	44.369	78	6	1	1
22.376	19	3	1	0	40.796	51	4	4	1	46.283	37	5	4	0
24.299	13	2	2	2	41.784	59	5	3	0	48.929	20	6	3	1
32.291	48	4	2	1	43.037	27	6	0	0	74.677	19	9	4	1
35.164	40	4	2	2	43.472	100	6	1	0					

APPENDIX B

DETAILED TABULATION OF TENSILE TEST RESULTS

Table B.1 Yield strengths of hot extruded specimens (produced from –2000+212 μm powders with an extrusion ratio of 144:1) at different temperatures.

Test Temperature (°C)	Yield Strength (MPa)	Avg. Yield Strength (MPa)	Stdev. (MPa)
RT	238.24	246.30	14.02
	262.49		
	238.18		
150	197.60	191.10	10.48
	179.01		
	196.69		
250	147.85	146.54	6.55
	139.44		
	152.34		
350	90.22	96.58	5.33
	94.31		
	99.82		
	101.97		

Table B.2 Ultimate tensile strengths of hot extruded specimens (produced from –2000+212 μm powders with an extrusion ratio of 144:1) at different temperatures.

Test Temperature (°C)	Ultimate Tensile Strength (MPa)	Avg. Ultimate Tensile Strength (MPa)	Stdev. (MPa)
RT	268.33	265.49	11.06
	274.85		
	253.28		
150	219.56	212.08	12.41
	197.76		
	218.92		
250	162.38	158.34	4.09
	154.20		
	158.43		
350	99.04	101.95	4.17
	97.87		
	104.27		
	106.61		

Table B.3 Elongations of hot extruded specimens (produced from –2000+212 μm powders with an extrusion ratio of 144:1) at different temperatures.

Test Temperature (°C)	Elongation (%)	Avg. Elongation (%)	Stdev. (%)
RT	0.59	0.90	0.29
	1.15		
	0.98		
150	1.95	2.13	0.39
	1.86		
	2.58		
250	3.06	2.66	0.36
	2.55		
	2.36		
350	3.08	2.91	0.26
	2.90		
	2.54		
	3.12		

Table B.4 Yield strengths of hot extruded specimens (produced from –212+150 μm powders with an extrusion ratio of 26:1) at different temperatures.

Test Temperature (°C)	Yield Strength (MPa)	Avg. Yield Strength (MPa)	Stdev. (MPa)
RT	248.86	247.90	1.36
	246.93		
150	215.31	212.94	3.35
	210.57		
250	166.54	161.87	6.60
	157.20		
350	101.52	99.82	2.41
	98.11		

Table B.5 Ultimate tensile strengths of hot extruded specimens (produced from –212+150 μm powders with an extrusion ratio of 26:1) at different temperatures.

Test Temperature (°C)	Ultimate Tensile Strength (MPa)	Avg. Ultimate Tensile Strength (MPa)	Stdev. (MPa)
RT	324.11	325.36	1.76
	326.60		
150	233.82	231.85	2.79
	229.87		
250	172.45	170.06	3.39
	167.66		
350	104.14	102.05	2.96
	99.96		

Table B.6 Elongations of hot extruded specimens (produced from –212+150 μm powders with an extrusion ratio of 26:1) at different temperatures.

Test Temperature (°C)	Elongation (%)	Avg. Elongation (%)	Stdev. (%)
RT	4.79	4.87	0.11
	4.94		
150	7.24	7.36	0.17
	7.48		
250	7.96	7.80	0.23
	7.63		
350	9.15	9.05	0.14
	8.95		

Table B.7 Yield strengths of hot extruded specimens (produced from –212+150 μm powders with an extrusion ratio of 81:1) at different temperatures.

Test Temperature (°C)	Yield Strength (MPa)	Avg. Yield Strength (MPa)	Stdev. (MPa)
RT	250.99	249.68	8.00
	241.10		
	256.95		
150	219.87	218.15	5.61
	222.71		
	211.88		
250	167.74	164.46	2.87
	162.41		
	163.23		
350	104.27	101.63	2.42
	99.52		
	101.09		

Table B.8 Ultimate tensile strengths of hot extruded specimens (produced from –212+150 μm powders with an extrusion ratio of 81:1) at different temperatures.

Test Temperature (°C)	Ultimate Tensile Strength (MPa)	Avg. Ultimate Tensile Strength (MPa)	Stdev. (MPa)
RT	330.04	327.94	2.18
	325.69		
	328.10		
150	246.42	234.84	12.87
	237.12		
	220.98		
250	174.96	172.07	2.65
	169.76		
	171.48		
350	106.34	103.94	2.41
	101.53		
	103.96		

Table B.9 Elongations of hot extruded specimens (produced from –212+150 μm powders with an extrusion ratio of 81:1) at different temperatures.

Test Temperature (°C)	Elongation (%)	Avg. Elongation (%)	Stdev. (%)
RT	5.24	5.16	0.46
	4.66		
	5.58		
150	8.07	7.84	0.32
	7.47		
	7.98		
250	7.95	8.02	0.08
	8.10		
	8.00		
350	8.93	9.32	0.43
	9.78		
	9.25		

Table B.10 Yield strengths of hot extruded specimens (produced from –150+106 μm powders with an extrusion ratio of 26:1) at different temperatures.

Test Temperature (°C)	Yield Strength (MPa)	Avg. Yield Strength (MPa)	Stdev. (MPa)
RT	276.17	274.69	2.09
	273.21		
150	232.24	237.01	6.75
	241.79		
250	184.46	183.41	1.49
	182.36		
350	110.26	109.56	0.99
	108.86		

Table B.11 Ultimate tensile strengths of hot extruded specimens (produced from –150+106 μm powders with an extrusion ratio of 26:1) at different temperatures.

Test Temperature (°C)	Ultimate Tensile Strength (MPa)	Avg. Ultimate Tensile Strength (MPa)	Stdev. (MPa)
RT	336.71	333.65	4.33
	330.58		
150	257.01	253.76	4.60
	250.50		
250	190.98	196.22	7.41
	201.46		
350	121.31	119.89	2.02
	118.46		

Table B.12 Elongations of hot extruded specimens (produced from –150+106 μm powders with an extrusion ratio of 26:1) at different temperatures.

Test Temperature (°C)	Elongation (%)	Avg. Elongation (%)	Stdev. (%)
RT	3.48	3.61	0.18
	3.74		
150	4.96	5.04	0.11
	5.12		
250	8.42	8.20	0.31
	7.98		
350	8.81	9.15	0.47
	9.48		

Table B.13 Yield strengths of hot extruded specimens (produced from –150+106 μm powders with an extrusion ratio of 81:1) at different temperatures.

Test Temperature (°C)	Yield Strength (MPa)	Avg. Yield Strength (MPa)	Stdev. (MPa)
RT	299.25	300.53	1.16
	300.29		
	302.06		
150	238.54	238.03	1.67
	236.16		
	239.38		
250	187.16	193.59	6.99
	192.58		
	201.04		
350	120.20	118.29	2.00
	118.46		
	116.20		

Table B.14 Ultimate tensile strengths of hot extruded specimens (produced from 150+106 μm powders with an extrusion ratio of 81:1) at different temperatures.

Test Temperature (°C)	Ultimate Tensile Strength (MPa)	Avg. Ultimate Tensile Strength (MPa)	Stdev. (MPa)
RT	388.10	387.21	3.45
	383.40		
	390.13		
150	264.26	262.96	5.32
	267.50		
	257.11		
250	215.65	216.60	1.31
	216.05		
	218.10		
350	126.40	126.17	2.07
	128.11		
	123.99		

Table B.15 Elongations of hot extruded specimens (produced from –150+106 μm powders with an extrusion ratio of 81:1) at different temperatures.

Test Temperature (°C)	Elongation (%)	Avg. Elongation (%)	Stdev. (%)
RT	3.67	3.72	0.17
	3.91		
	3.59		
150	5.33	5.35	0.60
	4.76		
	5.96		
250	7.49	8.68	1.26
	10.01		
	8.54		
350	8.07	9.48	1.23
	10.14		
	10.24		

Table B.16 Yield strengths of hot extruded specimens (produced from –106+90 μm powders with an extrusion ratio of 81:1) at different temperatures.

Test Temperature (°C)	Yield Strength (MPa)	Avg. Yield Strength (MPa)	Stdev. (MPa)
RT	319.68	318.94	1.06
	318.19		
150	262.16	263.50	1.89
	264.84		
250	207.49	204.26	4.57
	201.04		
350	124.43	122.38	2.89
	120.34		

Table B.17 Ultimate tensile strengths of hot extruded specimens (produced from –106+90 μm powders with an extrusion ratio of 81:1) at different temperatures.

Test Temperature (°C)	Ultimate Tensile Strength (MPa)	Avg. Ultimate Tensile Strength (MPa)	Stdev. (MPa)
RT	394.71	393.78	1.31
	392.85		
150	292.01	293.14	1.59
	294.27		
250	225.20	227.52	3.29
	229.85		
350	134.91	131.43	4.93
	127.94		

Table B.18 Elongations of hot extruded specimens (produced from –106+90 μm powders with an extrusion ratio of 81:1) at different temperatures.

Test Temperature (°C)	Elongation (%)	Avg. Elongation (%)	Stdev. (%)
RT	3.93	3.92	0.02
	3.91		
150	7.61	7.60	0.01
	7.59		
250	8.97	9.15	0.26
	9.34		
350	10.38	10.52	0.19
	10.65		

Table B.19 Yield strengths of hot extruded specimens (produced from –90 μm powders with an extrusion ratio of 81:1) at different temperatures.

Test Temperature (°C)	Yield Strength (MPa)
RT	342.91
150	282.28
250	238.33
350	133.22

Table B.20 Ultimate tensile strengths of hot extruded specimens (produced from –90 μm powders with an extrusion ratio of 81:1) at different temperatures.

Test Temperature (°C)	Ultimate Tensile Strength (MPa)
RT	407.61
150	320.83
250	254.51
350	143.17

Table B.21 Elongations of hot extruded specimens (produced from –90 μm powders with an extrusion ratio of 81:1) at different temperatures.

Test Temperature (°C)	Elongation (%)
RT	2.02
150	3.40
250	4.24
350	6.21

APPENDIX C

DETAILED TABULATION OF HARDNESS TEST RESULTS

Table C.1 Hardness values of samples parallel to the extrusion direction measured by Brinell test.

Powder Particle Size (Extrusion Ratio)	Test Points					Avg. Hardness	Stdev.
	1	2	3	4	5		
	6	7	8	9	10		
−2000+212 μm (144:1)	95	93	93	93	93	93.6	2.32
	93	93	89	97	97		
−212+150 μm (26:1)	102	97	102	102	99	101.5	2.42
	99	104	104	102	104		
−212+150 μm (81:1)	104	104	107	102	102	103.3	2.45
	107	99	102	104	102		
−150+106 μm (26:1)	110	110	104	107	99	106.2	4.64
	112	102	104	112	102		
−150+106 μm (81:1)	121	124	124	121	118	118.6	3.95
	118	115	115	112	118		
−106+90 μm (81:1)	118	115	124	128	115	120.6	5.17
	118	115	121	124	128		
−90 μm (81:1)	128	131	131	128	128	129.1	3.41
	124	131	124	135	131		

Table C.2 Hardness values of samples transverse to the extrusion direction measured by Brinell test.

Powder Particle Size (Extrusion Ratio)	Test Points					Avg. Hardness	Stdev.
	1	**2**	**3**	**4**	**5**		
	6	**7**	**8**	**9**	**10**		
−2000+212 μm (144:1)	91	89	93	93	91	91.6	1.90
	93	91	91	95	89		
−212+150 μm (26:1)	99	99	99	102	93	98.0	5.66
	99	91	97	91	110		
−212+150 μm (81:1)	102	99	102	99	107	100.0	2.98
	99	97	97	99	99		
−150+106 μm (26:1)	107	102	107	102	110	105.1	3.45
	102	110	102	107	102		
−150+106 μm (81:1)	115	115	118	118	115	115.3	2.21
	115	112	115	112	118		
−106+90 μm (81:1)	121	115	110	118	124	118.8	5.43
	124	121	124	110	121		
−90 μm (81:1)	128	124	131	128	121	126.3	3.37
	128	124	131	124	124		